Tomas Bata University in Zlín
Faculty of Technology

Doctoral Thesis

Mold Design Concept for Injection Molding of Highly Filled Compounds

Koncept vstřikovací formy pro vysoce plněné polymery

Author:	**Ing. Jakub Huba**
Study programme:	P3909 Process Engineering
Field of study:	3909V013 Tools and Processes
Supervisor	prof. Ing. Berenika Hausnerová, Ph.D.

Zlín, June 2019

This publication was issue in the year 2019

Keywords: highly filled compound, injection molding, phase separation, filling simulation, infra-red sensors, weld line, thermal conductivity, computed tomography, tensile strength

Klíčová slova: vysoce plněné systémy, vstřikování, fázová separace, tokové analýzy, infračervené senzory, studené spoje, teplotní vodivost, počítačová tomografie, pevnost v tahu

CONTENT

ABSTRACT

The thesis discusses the mold design for highly filled polymer melts, with a special emphasis on powder injection molding (PIM) compounds, which substantially differs from mold design requirements applied to conventional thermoplastic injection molding.

First part of the Thesis is devoted to a phase separation during injection molding. The mold design to quantify separation recently proposed by the PIM research group at TBU is treated with flow simulation approach (Moldflow). The data obtained from a capillary rheometry (viscosity) and differential scanning calorimetry (specific heat capacity) and modified transient plane source technique (thermal conductivity) is implemented to Cross model, where temperature-induced physical changes are predicted with the help of Williams-Landel-Ferry equation (WLF). Both models are used for simulations, and according to the results obtained, the new mold design is proposed. Simultaneously, the phase separation is detected with computed tomography on the real samples of stainless steel feedstock used in PIM.

As it is found that the separation is closely related to shear rate gradients accompanied with temperature changes, infra-red sensors are installed into the new testing mold to intercept the areas prone to this issue. Real observations made on PIM compounds are compared with simulated ones, and statistically analysed.

Second part of the Thesis is focused on a common problem during injection molding – weld line formation, which is most severe for highly filled polymers due to a lack of polymer entanglement across the approaching of the flow fronts. To increase time for an entanglement, the mold inserts from various materials (copper, aluminum, bronze, epoxy resin, and epoxy resin with hexagonal boron nitride, acrylic 3D printing material) with different thermal conductivity are used. It is shown (with the support of carefully selected statistical methods) that in case of conventional highly filled compounds as wooden plastic composites, weld lines have a considerable effect on the tensile strength, while for PIM feedstocks have not, but the presence of a weld line in a PIM part may be beneficial as it results in the shortening of the filling trajectory, and subsequently, leads to the time saving during molding.

ABSTRACT IN CZECH

Dizertační práce se zabývá koncepcí návrhu vstřikovacích forem pro vysoce plněné polymerní taveniny s důrazem na materiály pro práškové vstřikování (tzv. PIM technologii), kde se design nástrojů částečně liší v porovnání s požadavky pro vstřikování termoplastů.

První část práce je věnována fázové separaci, která vzniká během vstřikování vysoce plněných polymerních tavenin. Vstřikovací forma pro kvantifikaci fázové separace, jejíž konstrukci navrhla výzkumná skupina pro PIM na UTB ve Zlíně, byla podrobena tokové analýze (Moldflow). Získaná materiálová data pro výpočet viskozity, měrné tepelné kapacity a tepelné vodivosti byla implementována do simulace založené na viskozitním modelu Crosse. K predikci změny viskozity v závislosti na teplotě byl využit Williams-Landel-Ferry model. Z výsledků simulací byl odvozen návrh nové testovací geometrie. K detekci fázové separace na reálných PIM vzorcích na bázi nerezové ocele byla využita počítačová tomografie.

Bylo zjištěno, že fázová separace je úzce spjata s gradienty rychlosti smykové deformace. Jelikož jsou tyto gradienty doprovázeny změnou teploty, byla lokalizovaná kritická místa formy osazena infračervenými senzory pro měření teploty taveniny. Data získaná z měření byla porovnána s průběhy teploty během simulace procesu a statisticky vyhodnocena.

Druhá část práce pojednává o standardním problému během vstřikování – studeném spoji, což je v případě vysoce plněných polymerů (v důsledku nedostatečné difuze čel taveniny v místě studeného spoje) jeden z vážných problémů doprovázejících jejich zpracování. Pro prodloužení doby pro formování polymerních zapletenin byly použity vložky vstřikovací formy s různou tepelnou vodivostí (měď, hliník, bronz, epoxidová pryskyřice, epoxidová pryskyřice plněná hexagonálním nitridem bóru a akrylátová vložka z 3D tiskárny). V práci je statisticky podloženo, že v případě vysoce plněných polymerů na bázi tzv. WPC kompozitů, studené spoje mají značný vliv na pevnost, zatímco PIM směsi nevykazují žádnou závislost. V případě PIM materiálů však přítomnost studeného spoje zkracuje tokovou dráhu, což může vést k časové úspoře během vstřikovací fáze procesu.

AKNOWLEDGEMENTS

At this place I would like to express my sincere gratitude to my supervisor prof. Berenika Hausnerová for her help, time, advices and consultations. In addition, I would like to thank to assoc. prof. Vladimír Pata for his help with statistical evaluation of data and advices.
Further, I am deeply thankful for the support to my family, my friends, my colleagues and people who I met during my study.

INTRODUCTION

Currently, the aim of circular economy is to reduce the amount of generated waste, and recycle used materials. Therefore, thermoplastic composites are coming to the foreground, and filling of thermoplastic matrices approaches maximum values in terms of processability. This applies specially to powder injection molding (PIM) technology. These highly filled materials consist from two phases during injection molding, and their segregation may lead to deterioration of performance properties as mechanical and aesthetical. If the phase separation occurs, the part should not be passed to next processing, but regrind and used again.

Further, high loadings are associated to an abrasive wear, and therefore, special requirements on a surface quality of tools in contact with a melted compound. Wear is considered as most important parameter governing changes in a surface quality of not only tools, but also molded parts. Furthermore, physical properties such as viscosity and strength are affected by wear due to a change of surface energy, slip effect and roughness variations. All of these adjustments lead to a phase separation of feedstock components - powder and binder, which is currently the most severe issue of PIM technology. As a consequence, suitably designed tool at the beginning of its life-time may fail due to the progressive modifications during usage. So far, simulation approaches do not consider these changes. Therefore, simulation of formation of phase separation is a challenge starting with its detection during injection molding. Current methods focus largely on post-processing qualification (not quantification) of segregation, and no on-line method has been introduced so far.

Another weak point of design concept of molds for highly filled compounds are different mechanical properties obtained in longitudinal and traverse flow (processing) directions. Situation is dramatically changing with the presence of weld lines – the areas, where two or more flow fronts approach each other. Decreased weld line strength is due to insufficient diffusion between flow fronts, limited area of polymer macromolecules because of presence of filler and creation of V-notch due to entrapped air. Entanglement time between macromolecules may be elongated with lower cooling rate of polymeric melt what can be achieved with lower temperature gradient between polymeric melt and mold surface, or by adjustment of thermal conductivity of mold material.

THEORETICAL BACKGROUND

1. Powder Injection Molding

Powder injection molding (PIM) is a manufacturing technique combining the shape advantage of plastic injection molding with final properties of metals or ceramics (German 2001, Heaney 2012, German 2011). In comparison to machining and investment casting, PIM offers an economical saving for mass production of small components having a complex net-shape. Most of PIM items find application in automotive, military, information technologies as well as in medical field (Rak 1999). The selection of appropriate material features is governed by an application, because the selected material affects the final structure and properties of the products. Namely, powder size, particle size distribution, and particle shape as well as binder composition have a key role in the whole process.

1.1 Process of PIM

PIM process consists of four basic steps: mixing, injection molding, debinding and sintering, Fig. 1.

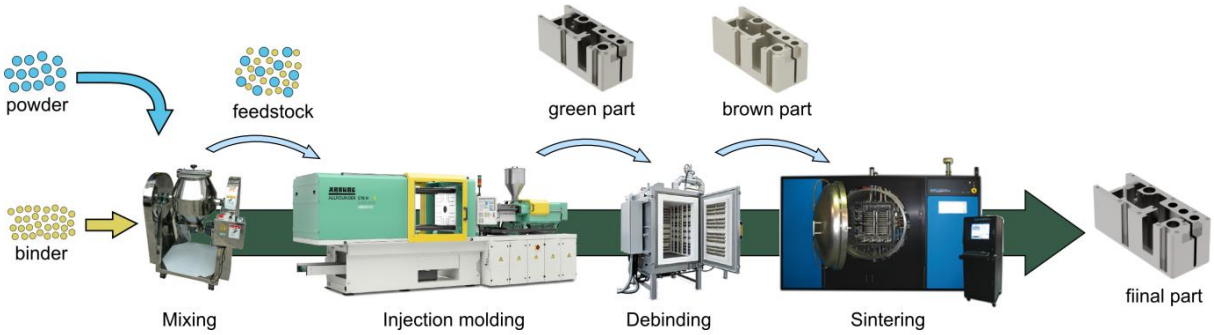

Fig. 1 – Processing steps in PIM technology

1.1.1 Mixing

In the first step, powder particles are mixed in high concentrations with a suitable polymeric binder system into homogenous PIM feedstock. Polymer binder is mostly composed of three types of components: backbone ensuring strength, low molecular weight polymers providing good flow properties for injection molding, and surfactants improving an adhesion between a binder and a powder. Feedstock usually contains 55 - 62 vol. % of powder particles, and is compounded into pellets (Hausnerova 2011). There is also possibility to purchase commercial feedstocks, which are ready-to-use.

Process of mixing involves melting of polymeric material with a subsequent adding of powder). Feedstock has a number of conflicting

requirements as an optimum amount of particulate material loaded into the binder, tailoring particle size distribution of the powder, proper mixing technology, assess of final mixture.

After mixing, it is important to control the homogeneity of a highly filled feedstock. For its determination two possible ways may be adopted (Bose 2013). First, observation of small portion of feedstock selected from a random area under microscope. Second, an inhomogeneous compound would have different density than the calculated one.

For a particular solid loading, the mixing torque should remain nearly constant during mixing (Fig. 2). According to Bricout *et* al. (Bricout, 2013), a sudden decrease of mixing torque means that the critical solid loading has been reached, and further added powder cannot be incorporated into the feedstock.

Roetenberg *et* al. (Roetenberg 1992) claims that mixture homogeneity is dependent on mixing speed. Reddy (1996) supplemented that increased speed results in increased temperature due to amount of energy input that has been converted to dissipation heat, and this might be detrimental for low molecular weight components of binder.

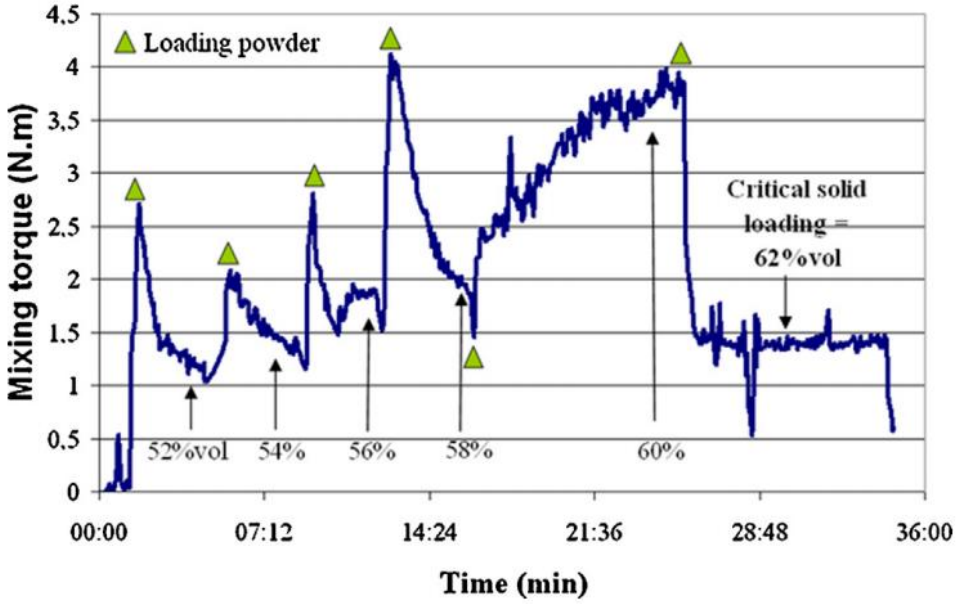

Fig. 2 – Monitoring of mixing torque in time (Bricout, 2013)

Interactions between polymeric binder and solid phase may have major effect on tendency to segregation of powder and binder from the feedstock (called phase separation) during injection molding step. Therefore, good contact on an interface should be ensured. Adhesion is a contact between two materials. Adhesion may be considered as a sum of various simultaneously acting bonding forces. Basic division of adhesion is into mechanical and specific ones. Mechanical adhesion is dependent on surface roughness and describes intrusion of one component into the depression surface of another. Therefore, surface

roughness and surface integrity have a major effect on mechanical origin of adhesion. Specific adhesion could arise from several principles (Heim 2015):

- chemisorbtion based on chemical interaction between phases,
- polarisation, where physical interaction between molecules results in adhesion processes. Requirement for a polarization are sufficient wetting of the solid phase surface and polarity of both components must be identical,
- electrostatic principle, which occurs between two joining component. Between polymer-metal composites relatively thin electric double layer develops and supporting adhesion,
- thermodynamic - requirement for this principle is sufficient contact between the components to develop the effect of intermolecular forces (van der Waals forces, hydrogen bonds, primary valence forces). Work of adhesion in this case is a reversible thermodynamic work that is needed to separate bonded particles from equilibrium state to a separation distance of infinity (Ebnesajjad, 2011),
- diffusion principle has major effect in polymer-polymer phases. Diffusion speed depends on molecular mobility, temperature of the interface and molecular weight. This principle of adhesion causes poor mechanical properties of weldlines in injection molding (Wilkinson, 1998).

In some cases, the feedstock is made from three components. Typical examples are porous PIM products, which consist from powder, binder and space-holder. These structures are (with advantage) used in medical applications, where a net-shape design allows proliferation of biomaterial. PMMA (Gulsoy 2008) is often used as a spherical space-holder, while NaCl (Raza 2015) and KCl (Tuncer 2014) are employed in case of irregular shape particles or fibers with high L/D ratio (Heaney 2012).

1.1.2 Injection Molding

Principle of molding step of PIM is the same as that of thermoplastics, Fig. 3. Feedstock passes through a hopper to a barrel, where - due to rotating screw - it is driven forward to a screw tip. Melting of material occurs due to the heat transfer from the barrel as well as the internal viscous heating caused by molecules deformation caused by rotation of the screw. Accumulated material at the screw tip is injected through the runner system into the mold cavity, where it obtains a shape of a future product (Kazmer, 2007, German, 2001, Tadmor, 2006).

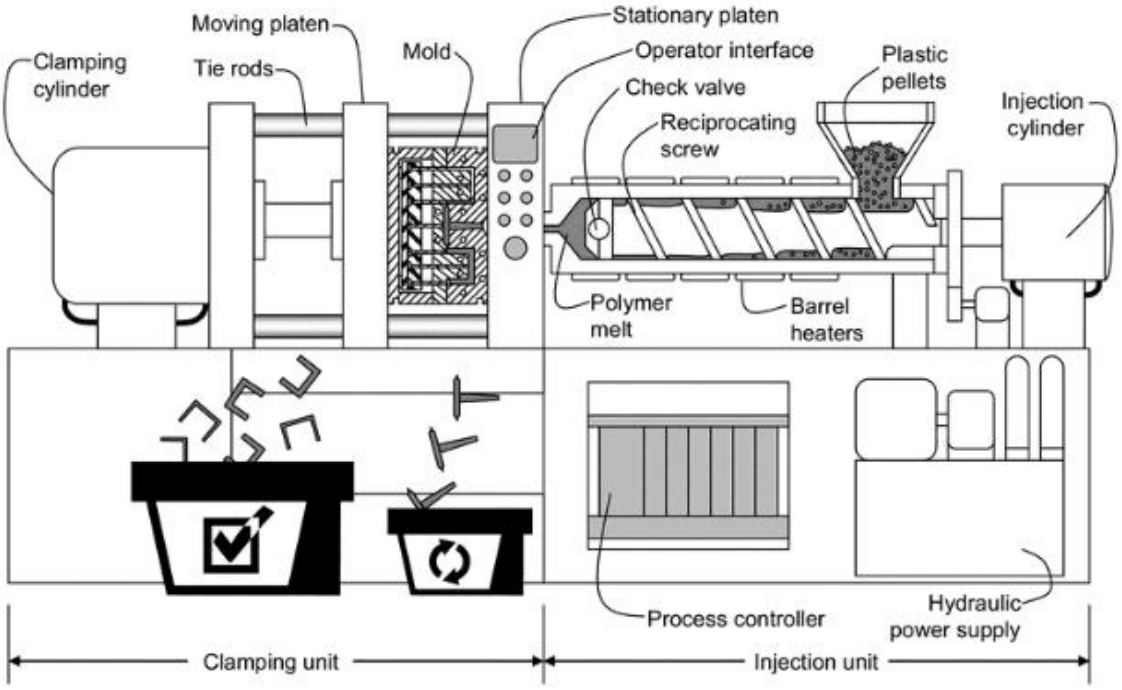

Fig. 3 – Schematic view of injection molding machine (Kazmer, 2007)

With respect to design, PIM follows plastic injection molding requirements for majority of its design features. There is a rule of thumb - everything moldable from plastics is also moldable from metal or ceramic powders (German 2001, German 2013). According to Walcher (Walcher, 2013) almost 70 % of all defects on final parts is due to an inappropriate design of injection molds. As in other production technologies, also PIM products have certain recommendations for moldability and production economics, Table 1.

Table 1 - Recommended design guidelines for PIM products (German, 2001)

Feature	minimum	maximum	typical
thickness [mm]	0.2	25	10
variation in thickness	----	100x	2x
max. dimension [mm]	2	1 000	100
tolerance [%]	0.03	2	0.3
weight [g]	0.02	20 000	40

One of the main requirements in a part design is uniformity of wall-thickness, which has the direct connection with a cycle time. Cooling is the most time consuming stage, and heat flux through a mold insert to cooling channels should be the same in all locations of a mold cavity. If the variation in wall-thickness occurs, this condition is rather difficult to ensure leading often to a non-uniform shrinkage, internal voids formation, deformations, etc (German, 2001).

1.1.3 Debinding

During debinding at least two binder components are distinguished. The first is removed at lower temperatures to obtain open pores through remaining molded body. This part of binder system is usually a low molecular weight polymer(s) with the main role to reduce feedstocks viscosity. While the main function of the second component, leaving the molded part at higher decomposition temperatures, is to retain position of the powder during sintering until the temperature, where diffusion bonds powder particles together (Heaney, 2012).

In practice adopted debinding techniques are solvent (Krauss, 2007), thermal (Enneti, 2012) and catalytic debinding (Li, 2007), see Table 2.

Solvent debinding removes a binder constituent with water, hexane, heptane, acetone, ethanol and other alcohols. Binder is dissolved in these liquids at low temperatures. Duration of debinding is a function of size of the part and size of the powder used in the feedstock. For example, parts made from 20 μm, 10 μm and 1μm powders with same binder system require 3h, 6h and 22 h of solvent debinding time, respectively (Hashmi 2016).

Thermal debinding is highly adopted due to high efficiency of binder burnout rate (pyrolysis), but an occurrence of part defects has limited this technique as a secondary debinding process (Hashmi 2016). Therefore, thermal debinding is mostly adopted as an operation after solvent or catalytic debinding (Heaney 2012).

Polyacetal binder system requires debinding in acid environment, and therefore, catalytic debinding has been adopted in PIM as well. Highly concentrated nitric or oxalic acid at elevated temperatures around 120 °C catalyze the degradation of POM constituent of the binder system (Hashmi 2016).

Table 2 - Debinding temperatures and rates for different binders (Heaney, 2012)

Binder		**Process parameters**		
Primary	**Secondary**	**Method**	**Temperature (°C)**	**Rate (mm/h)**
Paraffin wax	Polypropylene	Heptane	50	1.5
Synthetic wax	Polypropylene	Perchloroethylene	70	2.0
PEG	Polyacetal	Water	60	0.5
Polyacetal	Polyethylene	Nitric acid catalyst	120	1.5

1.1.4 Sintering

The final step of PIM is sintering, where a porous sample is densified under high temperatures into the final metal or ceramic product with sintered density around 97 % of the theoretical (Hausnerova 2013, Gasbarre 1989, Hausnerova 2011). With respect to Wu (2002), overall shrinkage of molded 17-4 PH material during sintering is up to 17 %. Sintering of a brown body is based on continuum mechanics. Total strain rate of model during sintering is (Fang, 2015):

$$\dot{\varepsilon} = \dot{\varepsilon}_e + \dot{\varepsilon}_{th} + \dot{\varepsilon}_{vp}$$

where $\dot{\varepsilon}_e$, $\dot{\varepsilon}_{th}$, $\dot{\varepsilon}_{vp}$ is elastic strain rate, thermal strain rate and visco-plastic strain rate, respectively. Stress rate can be defined as:

$$\dot{\sigma} = D_e \dot{\varepsilon}_e$$

where D_e is an elastic stiffness matrix and materials with isotropic properties can be expressed as:

$$D_e = \frac{E}{(1+\nu)(1-2\nu)} \begin{vmatrix} 1-\nu & \nu & \nu & 0 & 0 & 0 \\ \nu & 1-\nu & \nu & 0 & 0 & 0 \\ \nu & \nu & 1-\nu & 0 & 0 & 0 \\ 0 & 0 & 0 & 1-2\nu & 0 & 0 \\ 0 & 0 & 0 & 0 & 1-2\nu & 0 \\ 0 & 0 & 0 & 0 & 0 & 1-2\nu \end{vmatrix}$$

where E is elastic modulus of material and ν is Poisson ratio. According to previous studies of Zhang (2002) and Gasik (2000), mechanical properties of porous brown part are function of relative density of porous material ρ:

$$E = E_0 \exp\left[-b_0(1-\rho)\right]$$

$$\nu = \nu_0 \sqrt{\frac{\rho}{3-2\rho}}$$

where E_0 and v_0 are elastic modulus and Poisson ratio, respectively, for theoretical density of a full dense material, and b_0 is a fitting parameter.
After sintering, final products can be heat-threated or more densified in a hot isotactic press (German 1997).

1.2 Applications

PIM process is generally suitable for smaller and highly complex parts (Rosato 2000). Representative examples of consumer MIM products are shown in Fig. 4.

Fig. 4 - Examples of consumer products made by PIM (Otsuka 2018)

Although it might seem that products for a daily use are major part of MIM market, diversity of MIM applications is through the continents, Fig. 5. North America is mainly focused on firearm and medical applications, while MIM in Europe is mainly oriented to automotive industry. Year to year sales grow by a 9 % (400 mil. €). Sales of MIM products in China grow by a 10 %, and in year 2017 reached 812 mil. € with main applications in 3C components, namely smartphones (e.g. phone buttons - approx. 50 mil. parts, camera ring - approx. 100 mil. parts) (Williams 2018).

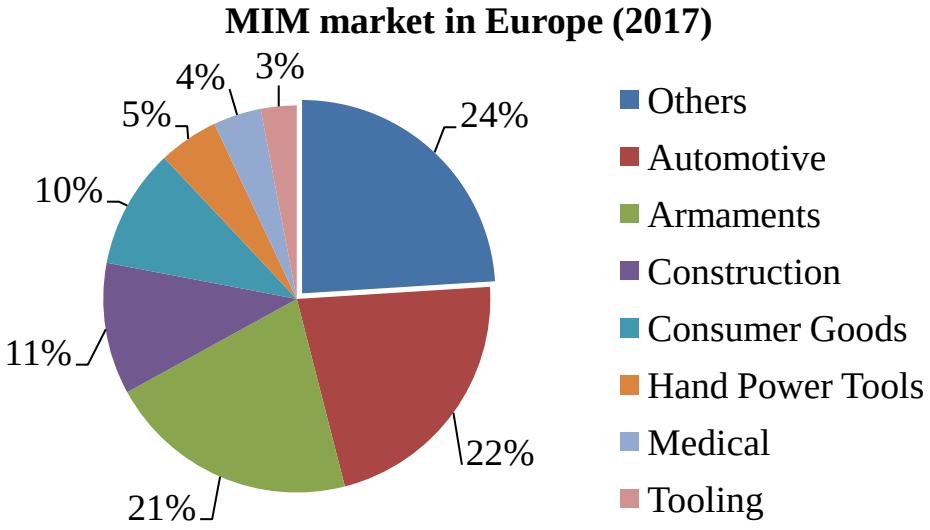

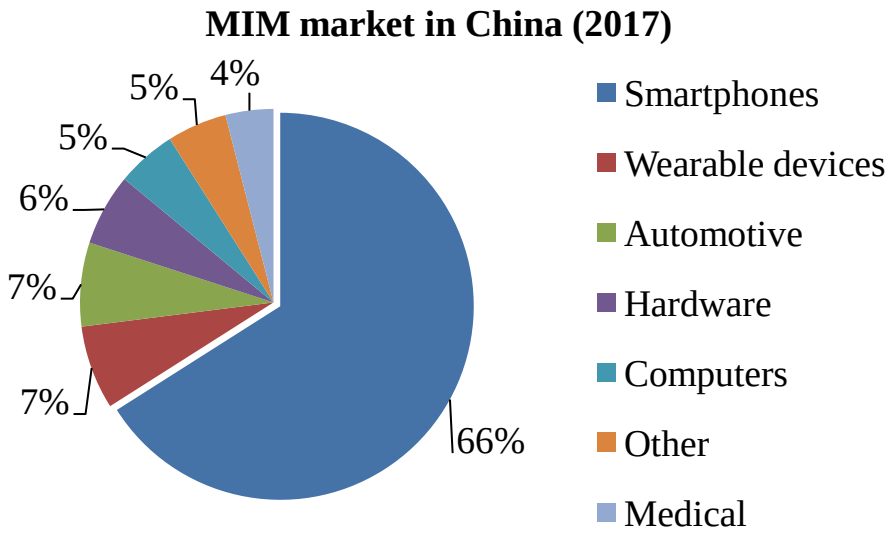

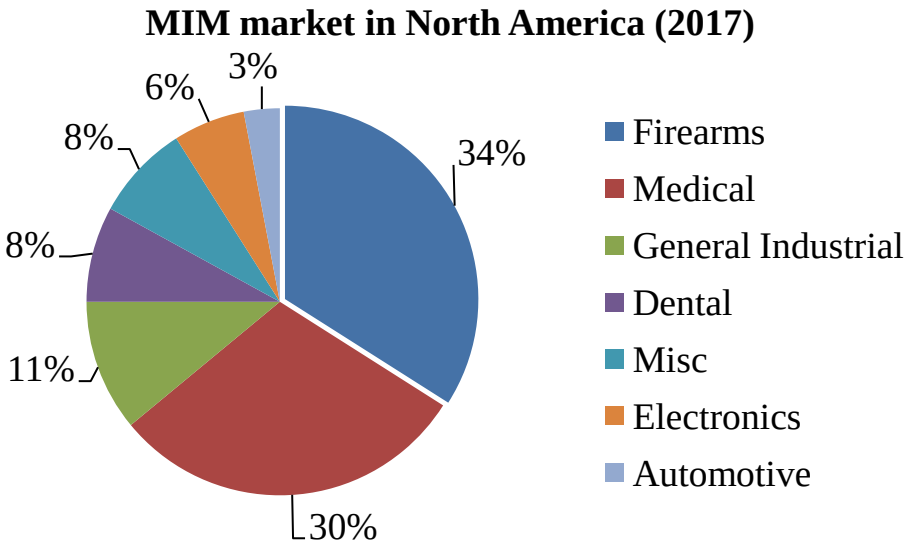

Fig. 5 - Applications for MIM parts in Europe, China and North America (Williams 2018)

1.3 Competitors of PIM

With respect to German (German, 1997) PIM should not be applied to productions of parts with low geometrical complexity, where die compaction, stamping, slip casting or die casting are sufficient. Because of set-up and tooling costs, the minimum production quantity for PIM is estimated to 5,000 units per year. Table 3 compares design features of different metal shaping technologies. As a main alternative of PIM, conventional machining, powder metallurgy (PM), investment casting (according to dimensional accuracy) were considered (Fig. 6), but currently, it is also additive manufacturing (AM).

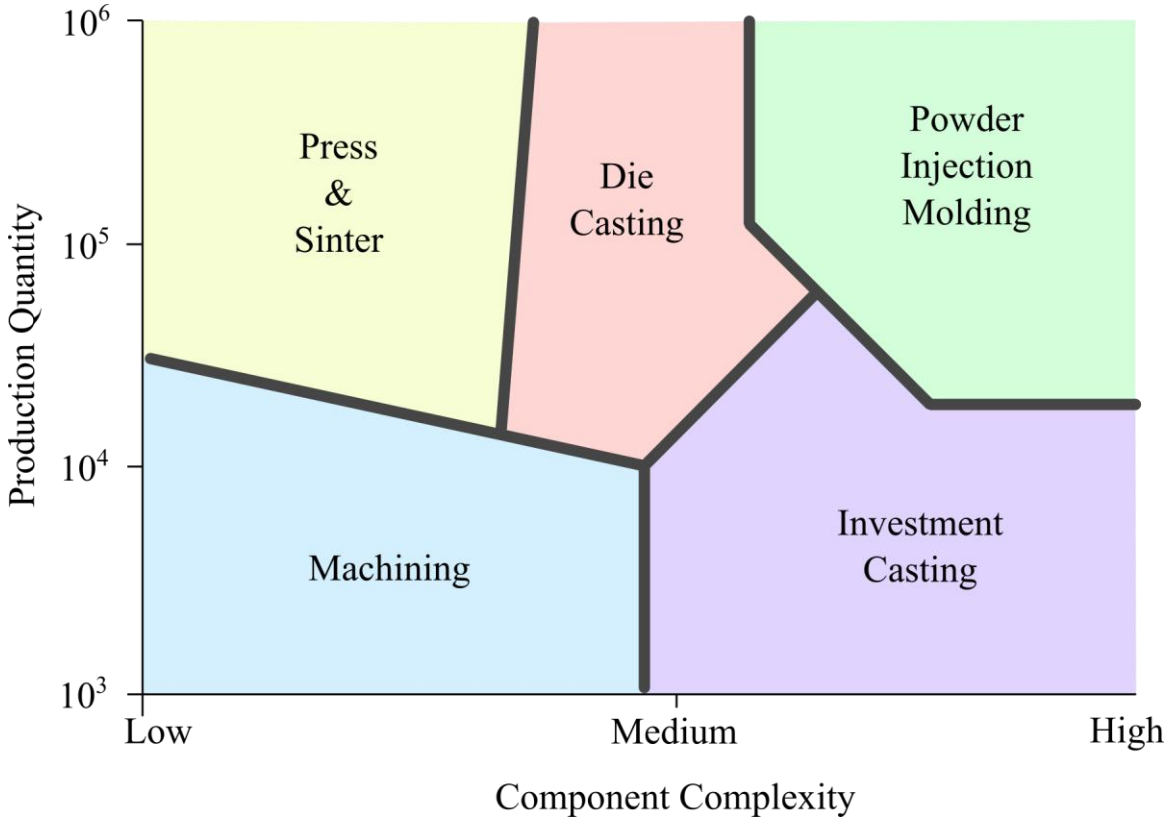

Fig. 6 - Preferred production technology with respect to component complexity and annual production quantity (German, 1997)

Table 3 - Comparison of MIM attributes with other fabrication techniques (Heaney, 2012, Duda, 2016)

Feature	MIM	PM	Casting	Machining	AM
Component size (g)	0.03 - 300	0.1 - 10^3	1 +	0.1 +	0.1
Wall thickness (mm)	0.025 - 15	2 +	5 +	0.1 +	0.1 +
Theor. density (%)	95 - 100	85 - 90	94 - 99	100	> 45
Theor. strength (%)	95 - 100	75 - 85	94 - 97	100	< 100
Surf. roughness (µm)	0.3 - 1	2 +	3 +	0.4 - 2	4 - 20
Production volume	2000 +	2000 +	500 +	1 +	1 +

Additive manufacturing (AM) is progressive method of building three-dimensional parts layer by layer guided by a 3D model. This process evolves creation of complex shapes with customized features without need of expensive tooling change. Nowadays, AM is accepted in a wide range of industry sectors, e.g. Ti-6Al-4V bracket for Airbus 350 with the optimized design resulting in 30 % weight reduction (Herzog, 2016).

With respect to automation of production (Srinivasan, 2018), AM technology has potential to enter mass production, and therefore, becomes a novel competitor of PIM technology.

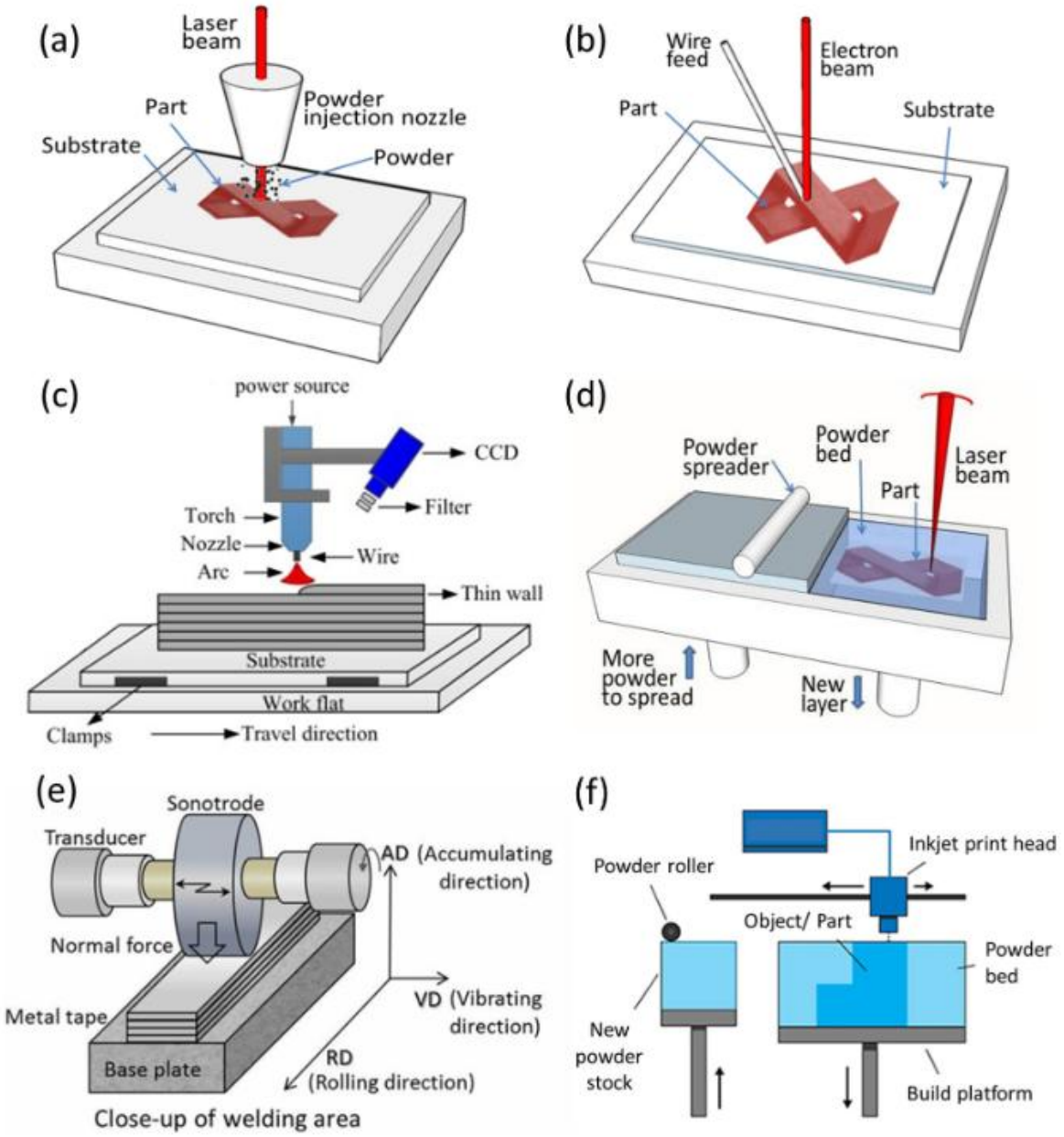

Fig. 7 – Different metal AM technologies (DebRoy, 2018)

All methods on Fig. 7 are commercially using different names (e.g. SLS-Selective Laser Sintering and SLM – Selective Laser Melting, where both are using powder bed and laser source of heat, and differ in process conditions), therefore, DebRoy (DebRoy, 2018) presented the nomenclature of different AM technologies according to principles of part creation and source of energy. Fig. 7 (a) represents Directed Energy Deposition with Laser (DED-L), where powder as a feedstock is used. Laser is tracking the shape of layer and powder is melted and transported to the focus area of laser. Fig. 7 (b) shows electron beam (DED-EB) as a source of energy and filler wire is feeding into the molten pool. On the other hand, in case of Fig. 7 (c), metal wire is melted according to arc and welded into substrate of previous layer. In all DED processed the heat source

and metal material are moving according to multi-axis system. With Fig. 7 (d) a powder bed fusion processes start with laser source of energy (PBF-L). Final part is formed, where laser exposes the energy on thin powder layer. Movement of layer is tracked with respect to a 3D model and after finish of layer, powder bed is z-levelled down and new powder layer is deposited. Fig. 7 (e) represents an ultrasonic additive manufacturing (UAM), where thin metal sheets are in shape of layers, and stacked on top of each other. Metal sheets are softened with ultrasonic vibrations and bonded together in solid state. Fig. 7 (f) shows binder jetting technology (BJ), where the same principle of powder bed as in (d) is used, the difference is only the principle of bonding. In this technology, a polymeric binder is used and deposited on powder with respect to shape of future part.

Additive manufacturing technique is crucial for the final part properties. At present, AM employs the powders developed for PIM. Both processes prefer wide powder size distributions to obtain high final densities. According to Anderson (2018), the crucial properties of feedstock are powder size range and size distribution within this range, powder shape, powder surface properties and powder alloy composition. Every AM technology has different requirement for powder size distribution (Nguyen, 2017); e.g. Inconel 718 ranging from 15 µm to 63 µm is suitable for DED-L (Sadowski 2016), while Helmer *et* al. (Helmer, 2016) used powders from 45 µm to 105 µm for DED-EB. Mostafaei (2019) showed the effect of a narrow particle size distribution on final density in case of BJ technology (Fig. 8).

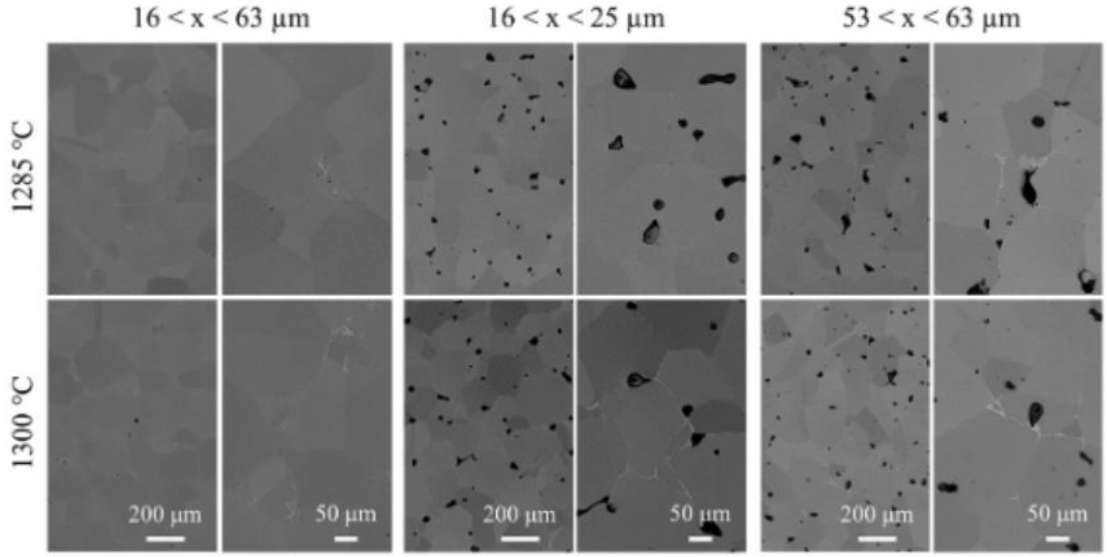

Fig. 8 – Dependence of particle size distribution on final density in Binder Jetting AM method (Mostafaei, 2019)

Spierings *et* al. (Spierings, 2011) used 316L stainless steel powder with three different size distributions and showed that the material with the highest

mean of D_{90} has the lowest ultimate tensile strength (approx. 600 MPa) in contrast with the lowest mean of D_{90}, where it reached 750 MPa.

All previously listed technologies employ metal powder or sheet and external source of energy, or polymeric binder for joining particles together. Technology which takes over basic principles of PIM technology (future part is made from feedstock, i.e. mixture of polymeric binder and metal powder) is fused deposition manufacturing (FDM) technology.

During FDM, printing material is heated up to melting temperature of polymer and afterwards it is extruded from nozzle to substrate of previous layer. All extruders for FDM are based on a piston principle, where piston is non-melted filament. Kukla et al. (Kukla, 2016) used TPE polymeric binder and polyolefin backbone with 55 vol.% of stainless steel 316L, Fig. 9. They pointed out that Young´s modulus and viscosity have a crucial role on printability – in their case apparent viscosity under 1000 Pa.s at about 100 s^{-1} and elastic modulus 800 MPa.

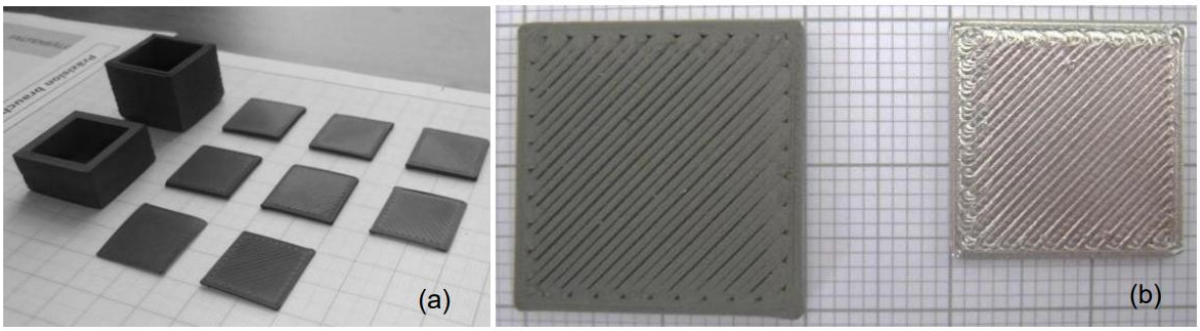

Fig. 9 – PIM feedstock used in FDM AM technique (a) after printing, (b) comparison of printed (left) and final part after sintering (right), (Kukla, 2016)

Bose *et* al. (Bose, 2018) focused on fine-grained tungsten heavy alloy and capability of its processing with conventional powder metallurgy, and recently developed AM approach. Nano-duplex W-Cr powder was mixed to obtain theoretical density of fully sintered part of 17.7 g/cm^3. The final density and Vickers hardness were compared for both technologies in Tab. 4.

Table 4 – Comparison of properties for press and 3D printed WHA material

	Density [%]		**Vickers hardness [HVN]**	
Sintering temperature	1500 °C	1600 °C	1500 °C	1600 °C
Pressed material	99.8 ± 0.2	99.0 ± 0.4	911 ± 66	946 ± 26
3D printed material	96.4 ± 0.7	98.4 ± 0.3	966 ± 66	945 ± 80

As FDM process is most like polymer extrusion with much lower pressure in die although with die swell after the lips or hot end of the extruder. Hebda *et* al. (Hebda, 2019) used four feeding rates for filament and with the help

of computed tomography he showed that in FDM method the flatness of perimeter walls is an issue (Fig. 10).

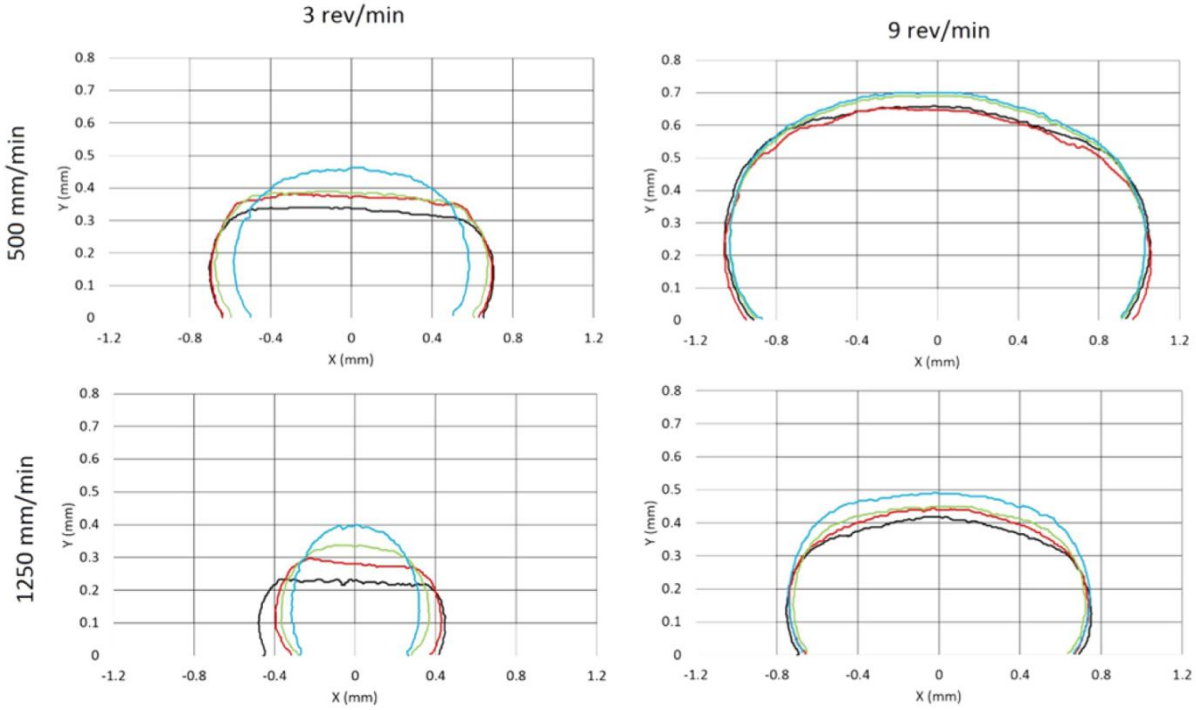

Fig. 10 – Dependence of extrusion rate, feeding rate and gap between nozzle and bulding platform to uniformity of extruded cross-section during FDM (Hebda, 2019)

The answer to solve a poor dimensional accuracy/geometrical tolerance could be combination of AM with conventional machining, Fig.11.

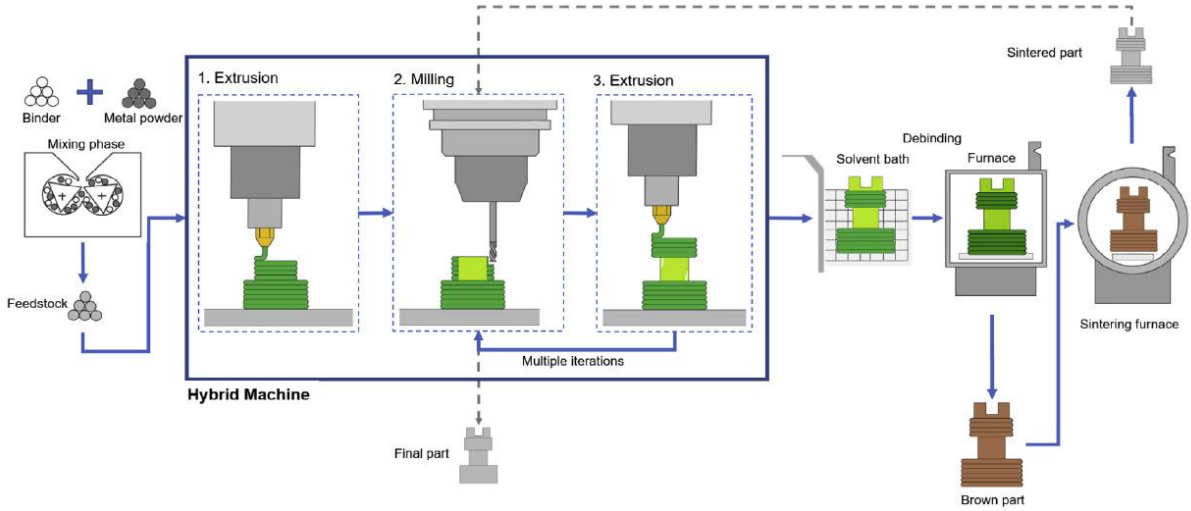

Fig. 11 - Combination of FDM with milling for tailoring the crucial dimensions (Parenti, 2018)

Parenti *et* al. (Parenti, 2018) used water-soluble binder (Embemould K83) filled with 60 vol.% of 316L (D_{50} = 8.8 μm, Sandvik Osprey), Fig 12.

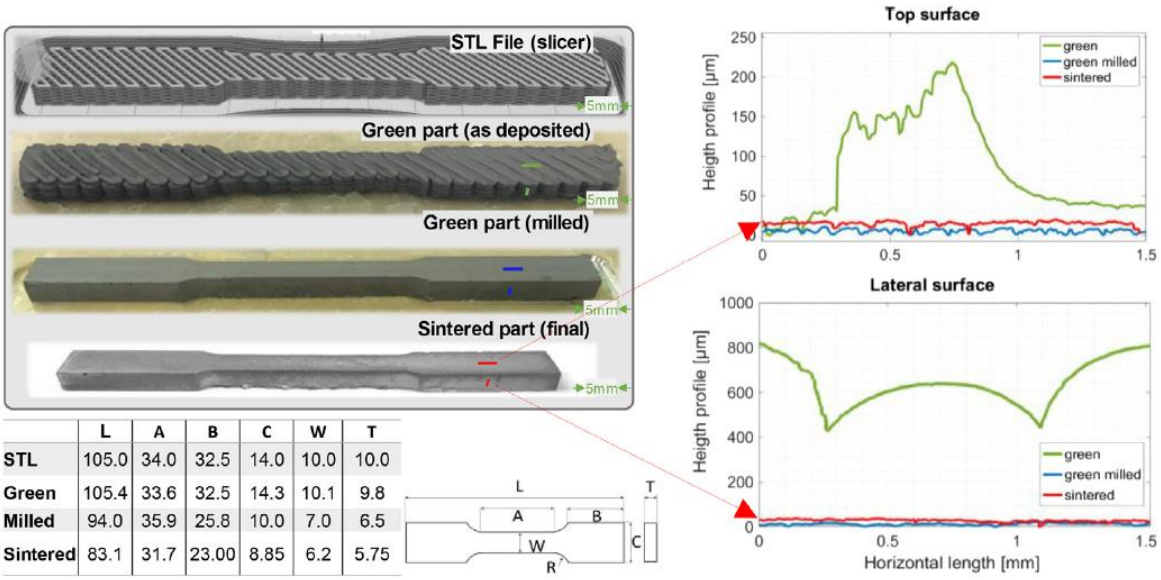

	L	A	B	C	W	T
STL	105.0	34.0	32.5	14.0	10.0	10.0
Green	105.4	33.6	32.5	14.3	10.1	9.8
Milled	94.0	35.9	25.8	10.0	7.0	6.5
Sintered	83.1	31.7	23.00	8.85	6.2	5.75

Fig. 12 – Surface roughness before and after milling (Parenti, 2018)

After printing, the arithmetic mean of a surface roughness was approximately *Sa* = 70 - 120 µm and after milling operation surface quality has been improved to *Sa* = 1.4 - 2.8 µm, which is more closer to surface roughness obtained with powder injection molding.

2. SIMULATIONS

In numerical simulations, a material flow is based on continuum assumption when mass conservation equation, momentum conservation equation, energy conservation equation and constitutive equations must be respected. For the whole family of equations to describe behavior during mass transportation Generalized Newtonian Fluid constitutive equation has been trivialized to:

$$\tau = -\eta\dot{\gamma}$$

where τ is shear stress, η is shear viscosity and $\dot{\gamma}$ is shear rate. During injection molding a variety of defects may occur. These defects could be caused by design, e.g. retraction from design recommendations, non-standard mold design or manufacturing out of tolerances. From processing, the defects may appear due to non-optimal debinding and sintering parameters, improper mixing or inadequate molding parameters such as molding pressure, injection speed, duration of holding pressure (Heaney, 2012). Examples of defects, which result from injection molding, are air entrapment, sink marks, cracks, internal voids, warpage and mainly powder concentration gradients. Prediction of defects using simulation tools should lead to optimization of design of part and tool as well as selection of proper molding conditions (Ilinca, 2004).

2.1 Rheological models for prediction of viscosity

For description of flow characteristics rheological models with different complexity are used. Complexity of model is expressed with number of parameters and the more complex rheological model is, the more difficult it is to find analytical solution.

Solid fillers, such as e.g. calcium carbonate or titanium dioxide in polymer composites processing, and also metal or ceramic powders in PIM technology, have the effect of increasing the viscosity. At high loadings, the increase can be dramatic and followed by that yield stress at low shear rates. When determining viscosity of highly filled systems it is important to note that presence of solid filler significantly accelerates the erosion of dies as well (Dealy 2000).

For very dilute suspensions of rigid spheres, the viscosity of the system is given by the Einstein equation:

$$\eta = \eta_0(1 + 2.5\varphi)$$

where φ is a volume fraction of a filler.

As the concentration increases, the filler effect on viscosity is more significant. For concentrations about 10 % it is necessary to introduce quadratic term and extend equation to:

$$\eta = \eta_0 \left(1 + 2.5\varphi + k\varphi^2\right)$$

where η_0 is viscosity of first newtonian plateau a k is empirical constant.
For monodispersed rigid spherical particles, Krieger-Dougherty equation is used very often (e.g. Loebbecke, 2009, Samanta, 2008):

$$\eta = \eta_0 \left(1 - \frac{\varphi}{\varphi_{\max}}\right)^{-[\eta]\varphi \max}$$

For rigid monodisperse spheres, the maximum packing φ_{max} is represented to a face centered cubic arrangement and reaches the value 74 %. If a sphere position is random, maximum packing decrease to 64 %.
Maximum packing can be modified with the filler polydispersity. With the wider filler size distribution, the maximum packing is increasing (e.g. Agassant 2017).
Gutierrez (Gutierrez, 2016) published an extensive study focused on rheological models which viscosity is function of one fitting parameter – maximum packing fraction.

For pseudoplastic (shear thinning) materials, the simplest model is called *power law* with only two parameters:

$$\eta = m\dot{\gamma}^{n-1}$$

where m is coefficient of consistency and n is non-Newtonian index.
Power law model is still very popular because of its simplicity and absence of first Newtonian plateau in PIM feedstocks (Xinbo, 2014).

Cross model is a three-parameter viscosity model, which intercepts viscosity at both low and high shear rate regions.

$$\eta = \frac{\eta_0(T_1)}{1 + \left[\frac{\eta_0(T)}{\tau^*}\dot{\gamma}\right]^{n-1}}$$

where τ^* is shear stress at the transition between first Newtonian plateau and shear thinning region. If zero shear rate viscosity η_0 is calculated according to Williams-Landel-Ferry equation, Cross model is turned to WLF-Cross model, which is widely used in numerical simulations of injection molding. In this case, WLF zero shear viscosity reflects the temperature and pressure effect more precisely:

$$\eta_0 = D_1 \exp\left\{\frac{-A\left[T-\left(D_2+D_3 p\right)\right]}{A_2+T-D_2}\right\}$$

where A_1, A_2 and D_1, D_2, D_3 are material parameters obtained from data fitting.

Carreau model is a four-parameter constitutive equation that also matches first Newtonian plateau, shear thinning region and also high shear rate region, where however polymer melts are usually not processed due to an excessive heating accelerating polymer degradation.

$$\frac{\eta(\dot{\gamma})-\eta_\infty}{\eta_0-\eta_\infty} = \frac{1}{\left[1+\left(\lambda\dot{\gamma}\right)^2\right]^{\frac{1-n}{2}}}$$

where η_∞ represents the second Newtonian plateau viscosity, λ is relaxation time.

2.2 Governing Equations

During the filling stage of molding process, a continuum approach is used to establish the system of governing equations. Mass and momentum conservation should be adopted with the assumption of incompressible melt flow and then the continuity equation is expressed as (Heaney 2012):

$$\frac{\partial u}{\partial x}+\frac{\partial v}{\partial y}+\frac{\partial w}{\partial z}=0$$

where *x*, *y*, *z* represents Cartesian coordinates and *u*, *v*, *w* are velocity components in an orthogonal coordination system. Navier-Stokes equations for molten feedstock should be described as:

$$\frac{\partial P}{\partial x}=\frac{\partial}{\partial z}\left(\eta\frac{\partial u}{\partial z}\right) \quad and \quad \frac{\partial P}{\partial y}=\frac{\partial}{\partial z}\left(\eta\frac{\partial v}{\partial z}\right) \quad and \quad \frac{\partial P}{\partial y}=0$$

where *P* is the pressure, η is the viscosity of the feedstock and *z* is the thickness of the flow domain.

In respect with injection molding of two-phase component, variation of concentrations of each phase will represent segregation effect during filling stage. Therefore, velocity of material is a function of velocity of each phase:

$$V_{ef} = \phi_s V_s + \phi_f V_f$$

where V_{ef}, V_s, V_f are effective velocity, velocity of solid phase and velocity of fluid phase, respectively and ϕ_s denotes to volume fraction of solid and ϕ_f is volume fraction of fluid phase (Barriere 2002).

During filling saturation conditions should be verified:

$$\phi_s + \phi_f = 1 \qquad and \qquad \frac{\partial \phi_s}{\partial t} + \frac{\partial \phi_f}{\partial t} = 0$$

According to precondition of incompressibility of both phases, densities remain constant and therefore, apparent density for each phase in the mixture is related to its volume fraction as:

$$\rho_s = \phi_s \rho_{s0} \qquad and \qquad \rho_f = \phi_f \rho_{f0}$$

where ρ_s and ρ_f are apparent densities of solid and fluid phase, respectively, and symbol *0* in density represents intrinsic densities of corresponding phase. Therefore, mass conservation should be verified by the flow of each phase:

$$\frac{\partial \rho_p}{\partial t} + \nabla.\left(\rho_p V_p\right) = 0$$

This approach is currently integrated into Sigmasoft simulation software (Thornagel 2010, Duretek 2017).

2.3 Numerical Simulations of Flow in PIM

Simulation of PIM process is an issue due to distinct properties in comparison with polymer (conventional injection molding) and metal powder (powder metallurgy). Many studies performed with the help of commercially available softwares as Moldex3D (Andrews 2010, Walale 2018), Moldflow (Kate 2016) and PIMsolver (Atre 2007) have been released without verification with experimental results .

Bilovol *et* al. (Bilovol, 2003a) compared three CAE programs to computational simulations of PIM injection molding, namely C-mold, Moldflow and ProCAST. The obtained results were compared with the experimental data. C-mold and Moldflow used Cross-WLF viscosity approximation, on the other hand ProCAST used Carreau-Yasuda viscosity model. The experiment showed that a wider part of the cavity is filled faster than narrower part. However C-mold software has not assume any hesitation of feedstock (Fig. 13).

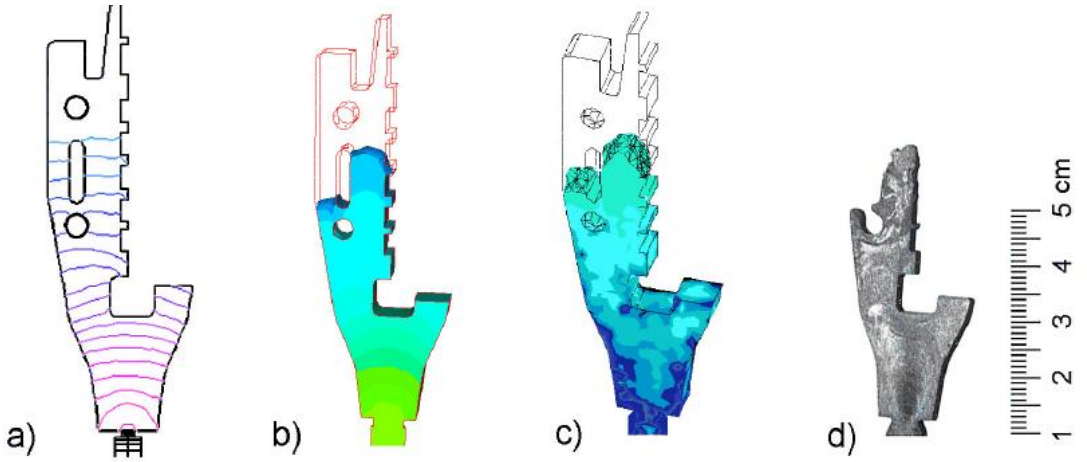

Fig. 13 - CAE simulation in C-mold (a), Moldflow (b), ProCAST (c), data from experiment (d) (Bilovov 2003a)

Bilovol (Bilovol, 2003b) also investigated a temperature distribution in CAE and compared it with real conditions. As a thermocouple, protruded Cr-Al type over cavity surface has been used. From the data obtained, it is evident that response time up to 0.5 s of bi-metal thermocouple leads to inaccurate data (position T3). C-mold predicts temperature development due to viscous flow and dissipation of shearing lead to increase of temperature between position T1 and T2 (Fig. 14). This phenomenon could be attributed to diameter of gating system (0.99 mm), where shear rate is predicted up to 5,000 s^{-1}. On the other hand, differences between T1 and T2 in ProCAST are not noticeable, and Moldflow ignores any viscous flow due to smooth decrease of temperature from gate to last filled location. Situation could be changed, if a finer mesh would be used.

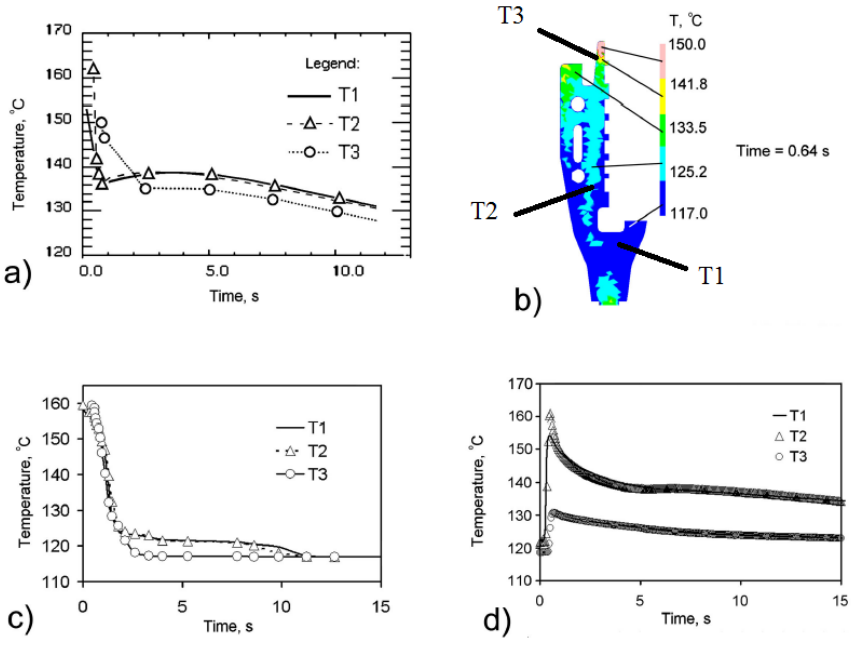

Fig. 14 - Prediction of temperature in C-mold (a), Moldflow (b), ProCAST (c) compared to real experiment (d) (Bilovol 2003b)

Drummer *et* al. (Drummer, 2014) compares flow front development in Sigmasoft software with experimental data. For his experiment, the first Newtonian plateau in Cross-WLF viscosity curve was substituted with Herschel-Bulkley viscosity model taking into account yield stresses (Fig. 15). This substitution has considerable influence, when the cavity is filled through a small gate, and presence of large surface of the melt with no contact to the mold wall is evident.

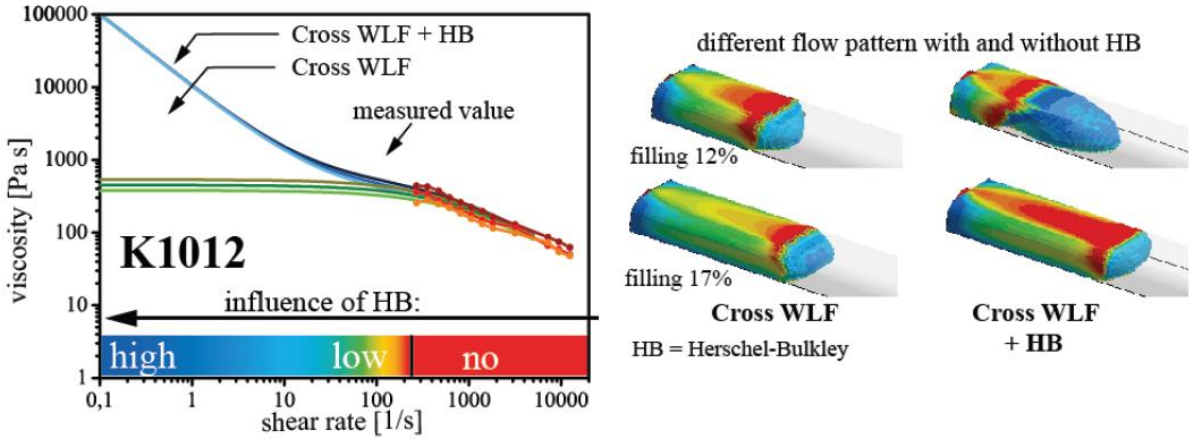

Fig. 15 - Replacement of the first Newtonian plateau from Cross-WLF with Herschel-Bulkley (Drummer 2014)

Marhöfer (Marhöfer, 2016) realized Moldflow simulation with comparison to experimental data. His investigation was focused on required pressure to fill the mold cavity. From results it is evident that requested pressure is approx. 20 % higher than predicted in Moldflow, and filling stage is about 45 % longer in comparison to Moldflow, Fig.16.

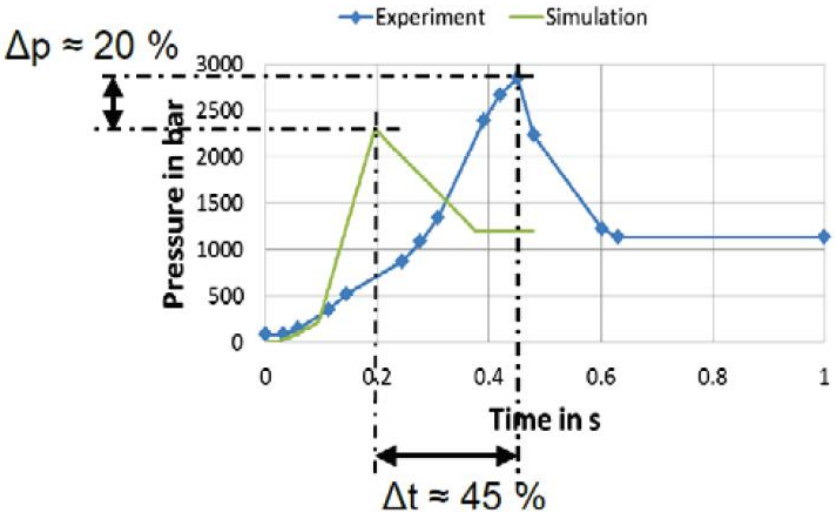

Fig. 16 - Injection pressure from Moldflow and real experiment (Marhöfer 2016)

This time extension might be caused by inertia of moving part of injection molding machine. On the other hand, Marhöfer (Marhöfer, 2016) operated with default thermal properties, and Moldflow is primary suitable for injection molding of plastics; typical thermal conductivity for plastics is λ_{PP} = 0.2 $W.m^{-1}.K^{-1}$, while for feedstocks it is 2,000 % higher ($\lambda_{17\text{-}4PH}$ = 4 $W.m^{-1}.K^{-1}$). Therefore, it is necessary to pay attention to material characteristics in order to minimize the error in input in boundary conditions in CAE software. Afterward, CAE simulations in PIM may be useful in the predictions of several problems during injection molding, and results may be incorporated in the tool design.

3. TOOLING

3.1. Tooling from Perspective of Moldability

Injection mold represents a complex task of production tools, where design engineering, material science, production engineering and quality control must be linked. Although design of injection mold for PIM feedstocks is similar to thermoplastic injection molding, few differences should be kept in mind during designing of the tool.

Generally, shrinkage in highly filled materials is rarely higher than 2 %, in PIM technology the final shrinkage after sintering step reaches the value between 15 % to 20 %. In some special applications as PSH PIM (Powder Space Holder Powder Injection Molding) to obtain porous structures with small porosity diameter, shrinkage may be up to 32 % (Heaney, 2012)

Shrinkage δ is calculated as a function of the length of the mold cavity L_0 and length of sintered part L:

$$\delta = \frac{L_0 - L}{L_0}$$

However, for a tool designer, it is more valuable to use a tool cavity expansion factor expressed as Z:

$$Z = \frac{L_0}{L} \quad \xrightarrow{or} \quad \frac{1}{1-\delta}$$

According to higher thermal conductivity of PIM feedstocks, obviously PIM injection molding machine has a longer nozzle than usual. The reason is due to minimizing of a sprue bushing length. Sprue bushing in thermoplastic injection molding works well with taper up to 1.5°, on the other hand, in PIM it is recommended to use taper of 5° due to stickiness of feedstock to the bushing surface. During injection molding, many occurring defects should be predicted with CAE simulations (entrapped air, weldlines, etc.). PIM powders are incompressible, and PIM feedstocks are more abrasive to the tools than thermoplastics. Therefore, parts in contact with a melted compound should be hardened or coated with wear resistant coating layers. Due to high filler volumes, injected parts are brittle and tend to stick to a parting line. Therefore, PIM tools should be produced in tighter tolerances in comparison with conventional injection molding to prevent flashing. Generally, in case of highly filled materials, mechanical properties may be significantly affected with weld line formation.

Xie *et* al. (Xie, 2010) molded PP matrix (DOW C705-44) filled with wood filler with 0.8 mm - 1.1 mm (Type 9) and 0.07 mm – 0.15 mm (type C100) particle sizes,. Both fillers may be classified as fibers with different *L/D* ratios. Due to higher size of Type 9, filler particles cannot be well entangled and distributed in weld line area, and therefore, the negative effect on tensile strength is significant, Fig. 17.

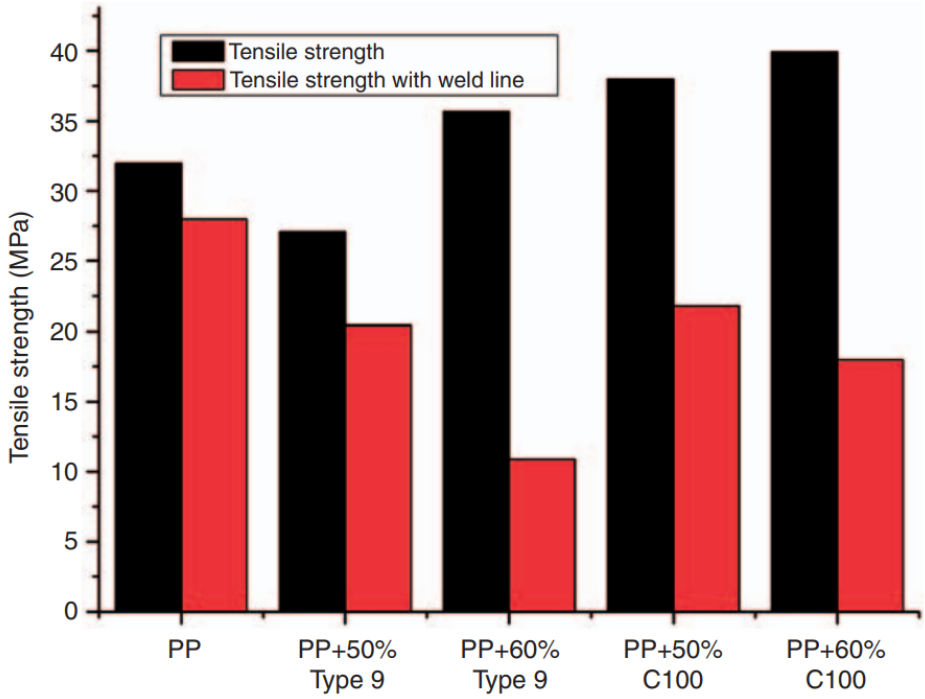

Fig. 17 - Influence of PP + fiber filler on tensile strength with/without weld line

Zhou *et* al. (Zhou, 2014) performed research on a flake filler. He used PP homopolymer with 40 wt.% of talc filler. From his results it is evident that flake filler has also negative effect on tensile strength, Fig.18.

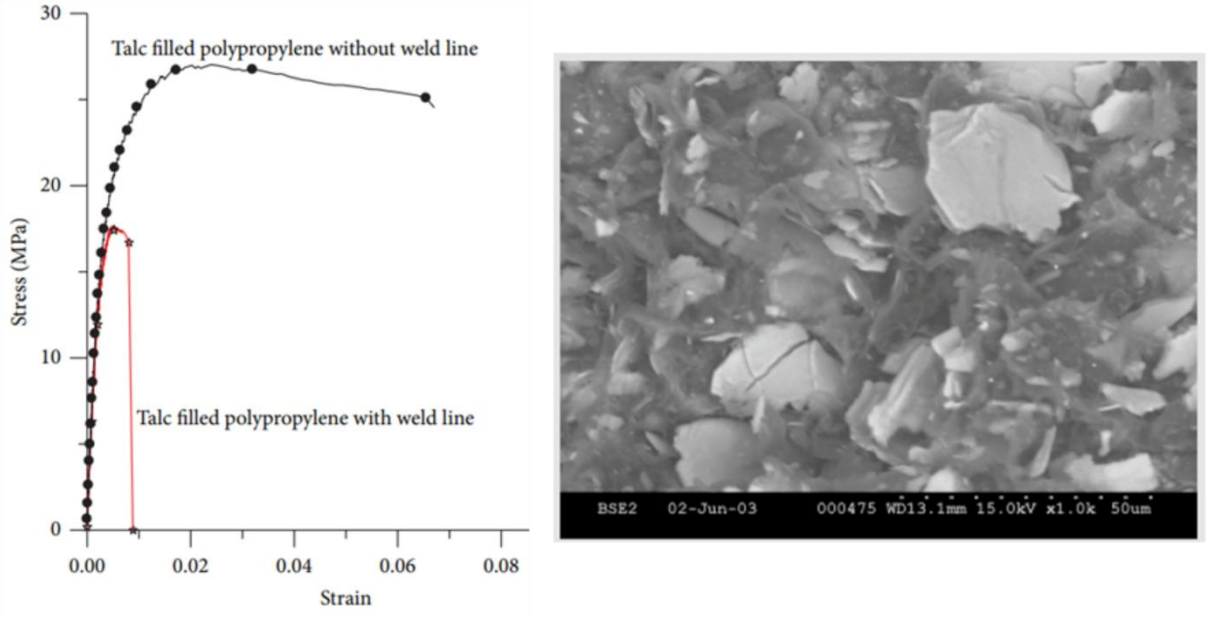

Fig. 18 - Influence of PP + flake filler on tensile strength with/without weld line

The reason of poor tensile strength at the interface of two melt flow fronts is primarily the parallel molecular orientation, and secondary, the presence of defects at this area as V-notch and encapsulated air from insufficient evacuation (Fig. 19).

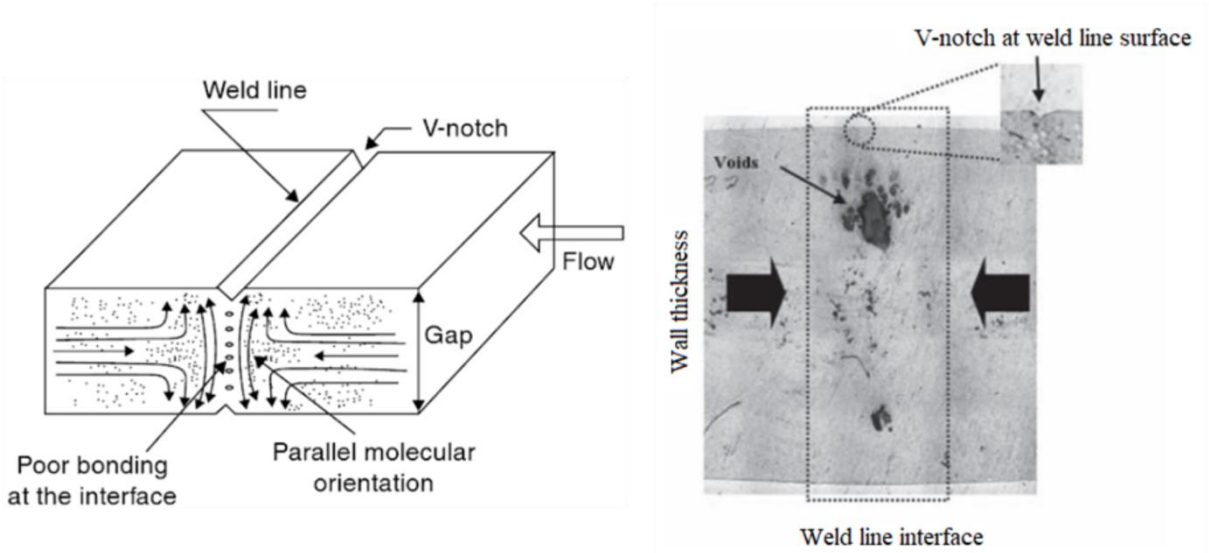

Fig. 19 - Poor bonding at the interface of weldline and V-notch (Suresh, 2012 and Jariyatammanukul, 2009)

Chen *et* al. (Chen, 2007) published in his study effect of melt and mold temperature on overall tensile strength of ABS with and without weld line, Fig. 20. After photoelastic testing he found that increased melt and mold temperatures induce lower residual stresses in parts without weld line, and therefore, higher tensile strength can be reached. On the other hand, lower temperatures lead to incomplete molecular diffusion of macromolecules in weld line area resulting in decreased tensile strength.

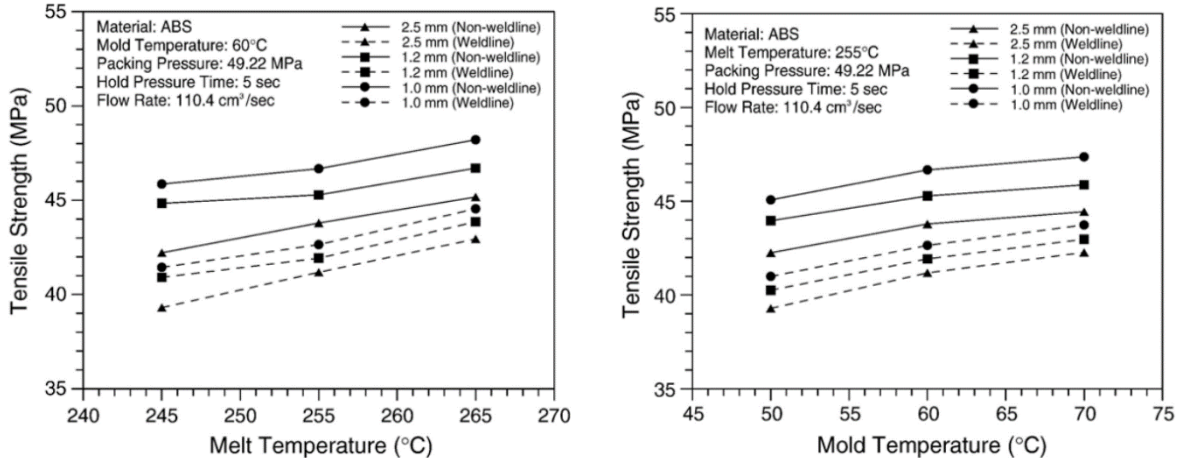

Fig. 20 - Effect of melt temperature on tensile strength with/without weld line (Chen, 2007)

Chookaew (Chookaew, 2018) investigated influence of mold temperature and distance from obstacle that forms weld line in rubber injection molding (Fig. 21) and showed that elevated temperature may positively affect weld line strength.

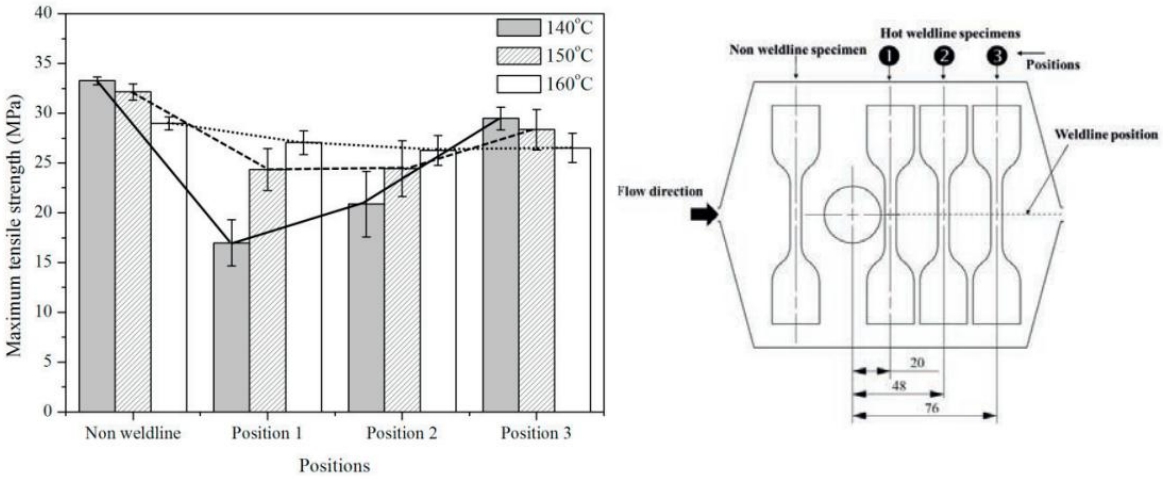

Fig. 21 - Effect of temperature and position of weld line on tensile strength for rubber injection molding (Chookaew, 2013)

Tensile strength of weld line depends on temperature. Thus, cooling rate has been investigated by Chen *et* al. (Chen, 2009) for ABS using different coatings of mold cavity, where PTFE is polytetrafluorethylene, TiN is titanium nitride and P20 is non-coated toolsteel (Fig. 22). Different coatings and different thicknesses of coatings have influence on tensile properties due to variation in the thermal conductivities and cooling rates. The values (in μm) 22, 10, 4 and 20, respectively, represent the thickness of the coating.

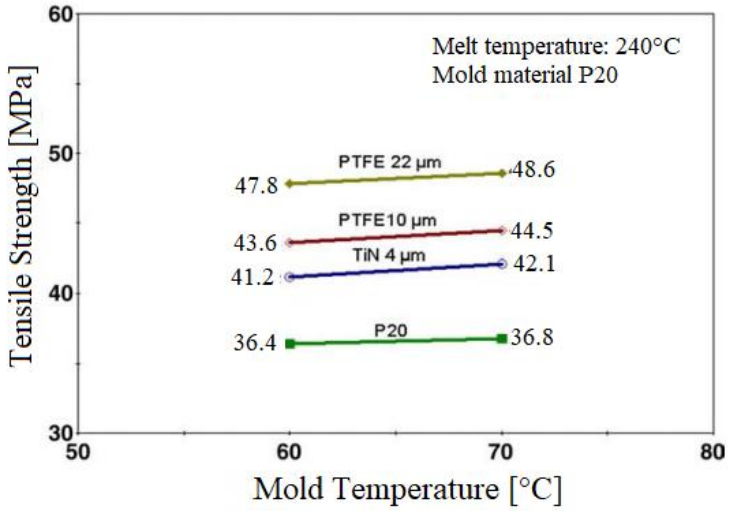

Fig. 22 – Weld line tensile strength with different thermal conductive interfaces (Chen 2009)

According to these findings, a present investigation will be focused on a weld line strength with different thermal conductivities of mold inserts, and a influence of processing parameters of highly filled compounds on a weld line strength.

According to high thermal conductivity of highly filled feedstocks in comparison to thermoplastics, a fast response of monitoring unit is necessary. Therefore, to monitor temperature. three methods are considered (Fig. 23).

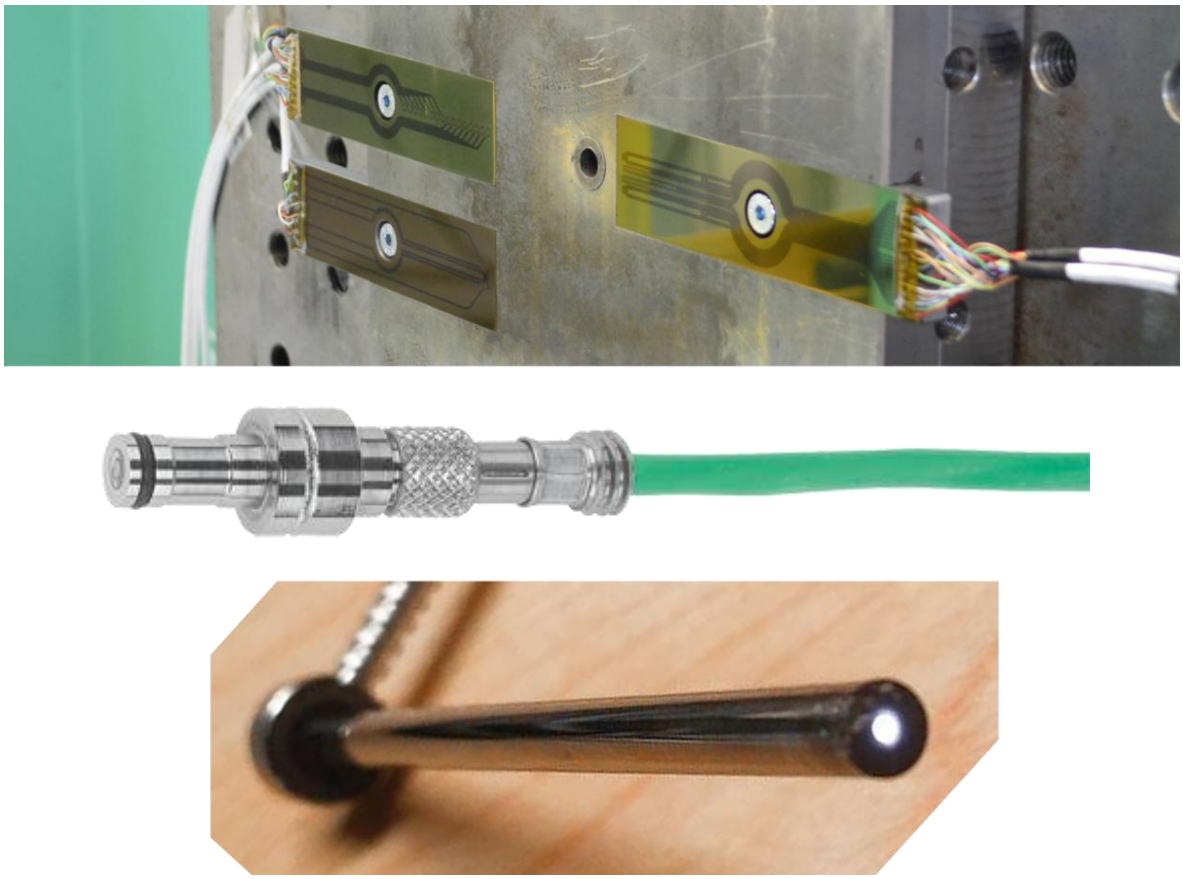

Fig. 23 - Thin film sensors (up) metal thermocouple (middle) infra-red sensor (bottom) (Kistler, 2019)

Thermocouple and thin-film sensors can be considered as contact measuring methods (Biehl, 2006, 2016, Kyas, 2012), on the other side infra-red (IR) temperature sensors are based on infrared radiation, and thus considered as non-contact measurements. From results of Martinsen *et* al. (Martinsen, 2017) it seems that the integrated thin film sensors are measuring surface temperature of the polymer surface. The same finding was reported by Guerrier *et* al. (Guerrier, 2017), where maximum temperature of ABS (217°C) during filling was recorded below T_g (70 °C). IR sensors monitor material temperature as a bulk with response time up to 10 ms. (Bendada, 2014)

3.2. Tooling from Perspective of Life-Time

Wear could be defined as a material removal from a surface due to interactions with a mating surface. Almost all machines lose their durability and reliability due to wear, and the possibilities and functionalities of new advanced machines are reduced due to a wear too. Hence, a wear control has become a strong need for the advanced and reliable technologies. Wear results in a material removal by physical separation due to micro-fractures, by chemical dissolution, or by melting at the contact interface. Therefore, as can be seen in Fig. 24, there are several types of wear: adhesive, abrasive, fatigue, and corrosive (Bhushan 2000, Moore 2013).

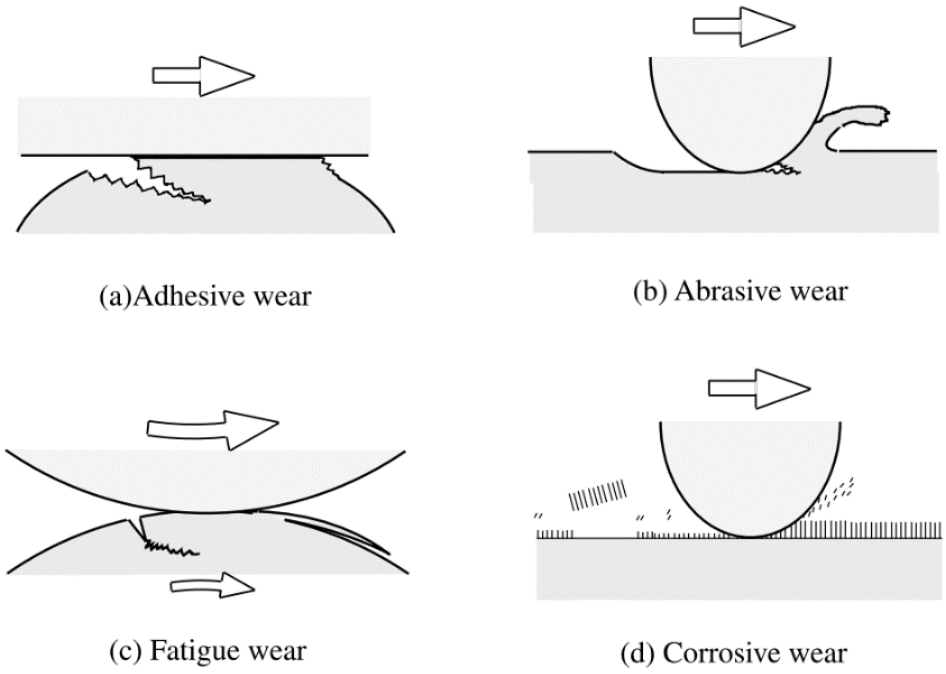

Fig. 24 – Types of wear (Bhushan 2000)

In PIM technology, a polymer binder is highly loaded with round (spherical) or irregular (low *L/D* ratio) shaped powders. In some non-conventional PIM techniques, as molding of porous structures, fibers with high *L/D* ratio are used as well (Heaney 2012, Kim 2016). A significant degradation of surface quality is mostly visible at first in a cavity gate, where the change of melt cross section (from runner to gate) profile becomes significant, which leads to an increase of pressure, shear rate and wear (Kim 2016). In general, fillers based on hard particles cause high wear due (Rosato 2000)

Injection molds show surface degradation resulting from different wear mechanisms causing a decrease of surface quality of a molded product. The most important wear mechanism of injection molds for PIM technology in common processing parameters is when hard particles from a feedstock reach a mold cavity and deteriorate surface quality of tools via abrasive wear causing

cutting, wedge forming and ploughing of surface (Fig. 25). Clearly, wear will have a considerable effect on powder-binder separation during molding.

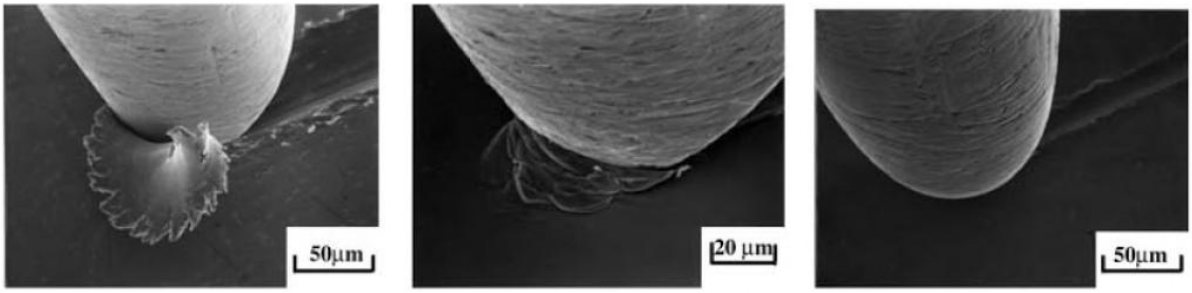

Fig. 25 – Cutting (left), wedge forming (middle), ploughing (right) abrasive mode (Kato 1988)

Spherical and irregular powder shapes are most common in PIM. To analyze a wear resistance of metal substrates, polyoxymethylene (POM) binder system has been used (Schneider 2005). This binder has been filled with 50 vol.% of spherical zirconia (ZrO_2) powder, 55 vol.% of irregular alumina (Al_2O_3) and 55 vol.% of stainless steel 17-4PH filler with particles ranging from (0.3 to 0.4) μm, (0.4 to 0.6) μm and (4 to 6) μm, respectively. All feedstocks were injected into the testing mold 1400 times, and the volumetric wear of the unalloyed, low- and high- alloyed steels has been evaluated (Fig. 26).

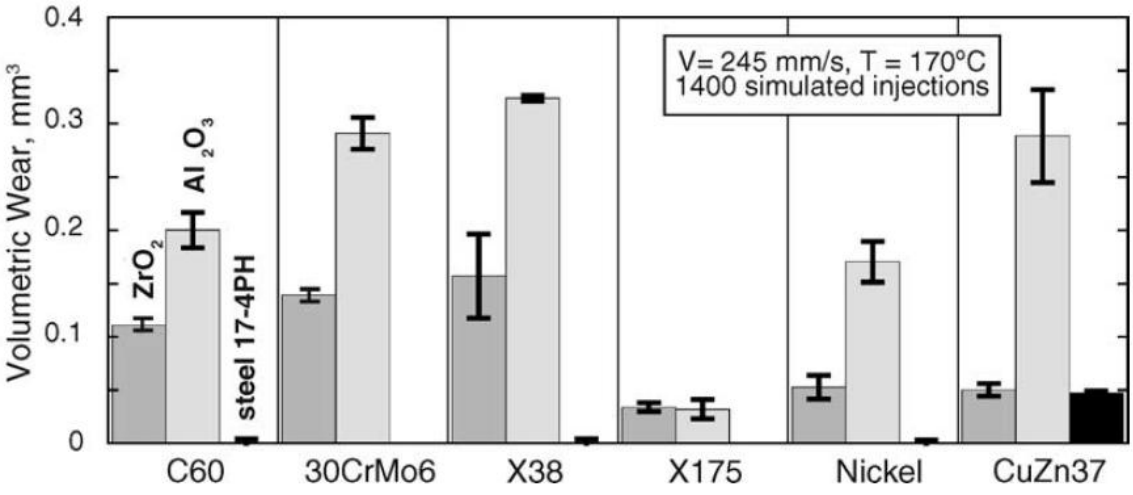

Fig. 26 - Volumetric wear of different mold materials (Schneider 2005)

Mold materials were represented with C60 - unalloyed carbon steel with defined carbon content 0.8 %, 30CrMo6 – low alloyed steel with carbon content 0.3 % , and chromium 1.35 %), X38 - hardened high-alloyed steel (0.38 % C, 5 % Cr, 1 % Mo), X175 – PM steel (1.75 % C, 9 % V, 5 % Cr). Nickel insert was made by electroplating, and alloy CuZn37 represented typical brass material (67 % Cu, 37 % Zn).

The best resistance to the wear proved the PM steel X175, which consists of 20 % of fine carbides homogeneously distributed in a martensitic matrix (Schneider 2005). The effect of carbides in a steel matrix is significant,

when the distance between hard carbides in a homogenous structure is not more than a dimension of an abrasive particle (Mennig 1995). Therefore, especially ceramic powders are highly abrasive to the tools for processing, and as it can be seen from Fig. 26, irregular ceramic particles are more abrasive than spherical ones.

Rate of wear is a function of many parameters, for instance pressure, particle shape and size, exposure time or number of cycles. It is not possible to eliminate wear effect of materials, but only to control it. Improving the wear resistance is a challenge to increase a repeatability of the process due to dependence of wear on surface parameters, slip effect and phase separation leading to dimensional, mechanical and visual alters. Therefore, it is necessary to extend the life-time of the mold and delay the period when all of these problems occur. Deterioration of surface quality due to wearing may lead to the most severe issue during injection molding of highly filled materials - phase separation. Phase separation is an initiator of other defects as delamination in PIM, out-of-tolerance shrinkage and dimensions. For highly filled polymers as wooden plastics composites (WPC), phase segregation leads also to visual defects and impossibility of usage of WPC in visual applications (see Fig. 27).

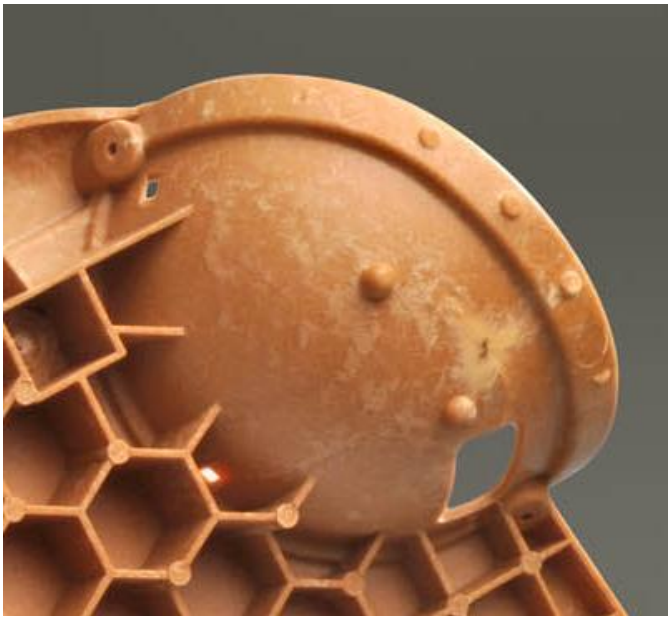

Fig. 27 - Phase separation on highly highly filledfilled WPC compound (Duretek, 2016)

4. PHASE SEPARATION OF HIGHLY FILLED COMPOUNDS

Powder/binder separation, in literature also referred as phase segregation, is the most frequently observed issue in PIM (German 1997, Heaney 2012, German 2013). Powder binder separation, created during injection molding stage, causes quality failure as uneven porosity, warpage, cracks or visual defects. The main factors influencing phase separation are different densities of feedstock components, high speed and high pressure of injection molding process (German 2007, Hausnerova 2011, Jenni 2008). Discussion with leading research institution in this area (Walcher 2013) revealed that the surface roughness finer than $Ra = 0.8$ μm can be another cause of separation.

4.1. Theoretical Approach to Evaluation of Phase Separation

During injection molding stage it is necessary to have a homogenous mixture of powder and binder, and thus uniform distribution of a powder in feedstock granules. If this condition is accomplished, introducing of errors incoming from a mixing stage can be eliminated (Thornagel 2009).

Thornagel (Thornagel, 2009) demonstrated that during injection molding powder particles are forced by a local shear rate gradients to leave such areas of high shearing. As it is shown in Fig. 28, the particles in the middle of the flow domain within the plateau of shear rate continue their way without the change in the direction. The particles, which flow in the areas of the non-plateau shear rate gradients, are forced to rotate. The rotation becomes the bigger, the bigger the shear rate gradient is. Then, a change in the flow direction of the particles is initiated due to their rotation (Hausnerova 2011, Thornagel 2009).

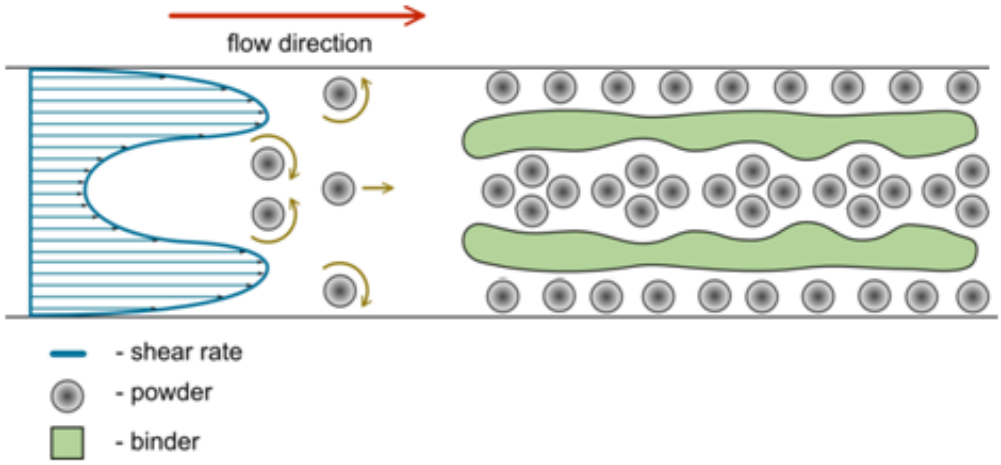

Fig. 28– Powder/binder separation caused by local shear rate gradients (Thornagel 2009)

Development of shear rate gradients is governed by a design of a mold cavity. Thus, the mold design plays the crucial role in the description of this issue. During the filling stage, a feedstock has a certain powder and binder contents because of low shear rate gradients in a runner system. The situation changes, when the volume unit arrives to the gate area, where the shear rate gradients become higher. According to the concept of separation (Fig. 29), the volume unit travelling in the center of the trajectory, will assign an additional powder. The volume unit flows through low and high shear rate areas to the final destination inside the mold cavity. During the flow, the perceptual content of powder particles is varying, and a phase separation occurs. It should be mentioned that the sudden changes in the flow direction can also cause phase separation and form powder rich areas (Karatas 2008, Heaney, 2012).

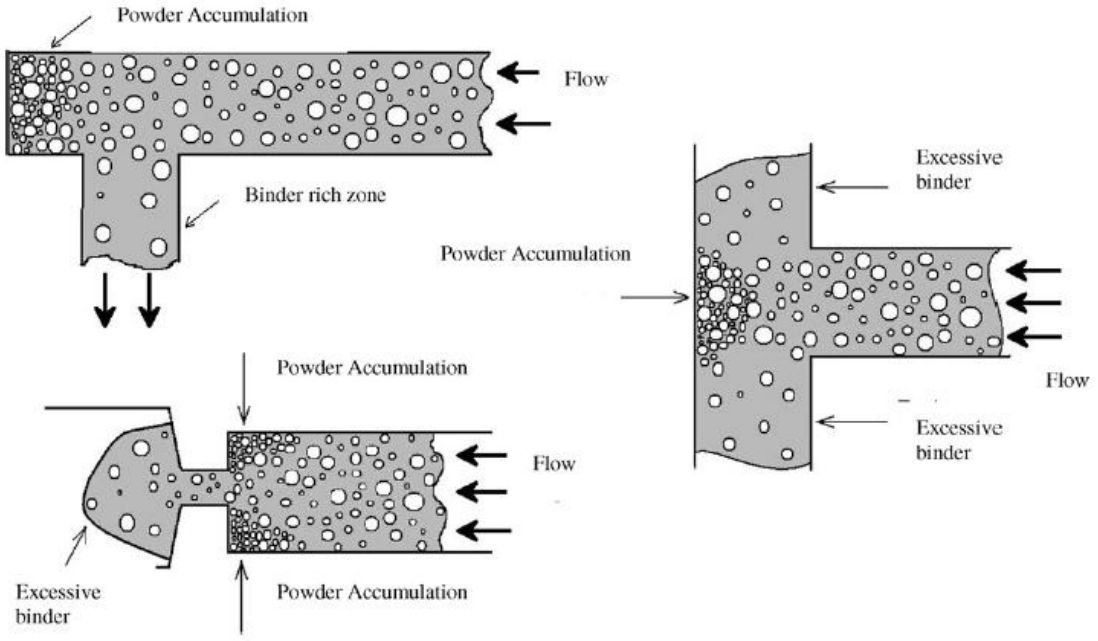

Fig. 29 – Phase separation caused by sudden geometrical changes in mold cavity (Heaney 2012)

A feedstock flow is modeled as a bulk by using of Navier Stokes equations. However, a PIM feedstock is two-phase system. Thus, the Navier Stokes equations should be formulated for each component – powder and binder, and both have to be coupled in an appropriate way as was mentioned in Section 2.2.

4.2. Practical Approach to Evaluation of Phase Separation

For experimental studies and subsequent quantification of a phase separation four types of mold designs have been used. The most widely employed moldability test for plastics measures the filling of a spiral flow channel. Moldability is expressed as a flow length of a material under certain

injection molding conditions. Injection is performed to a cold mold, which results in creating of a frozen layer on a surface between mold and cavity (Fig. 30). As a heat transfers from material to a cold mold, formation of a frozen layer is increasing, and simultaneously, a liquid feedstock area in a center of flow channel is decreasing. In comparison to plastics, PIM feedstocks have higher thermal conductivity, which leads to a faster solidification. This is the reason for higher injection rates used in PIM (German 1997, Karatas 2008).

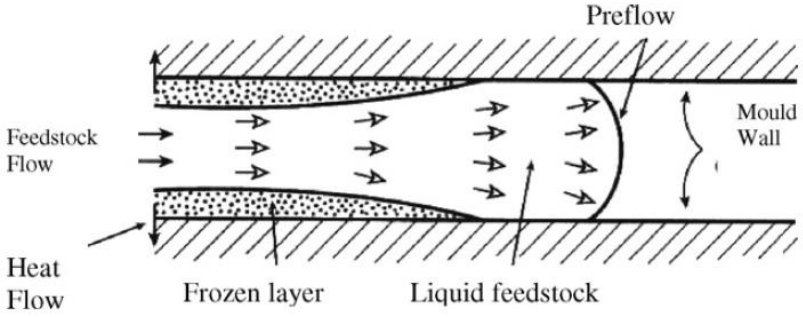

Fig. 30 – Feedstock flow along the mold canal (German 1997)

PIM feedstock in a spiral mold separates because of cold die walls, a powder rich plug is situated at a flow tip. Flow stops, when the value of pressure at the tip of a flow path decreases below the yield strength of the feedstock (German 1997, Hsu 1995).

To express moldability of PIM feedstocks, a zig-zag mold was specially designed at San Diego University back in 90′ (German 1997). Design of this mold is schematically shown in Fig. 31. Material flow is forced to change the flow direction because of side branches. During the flow, powder rich areas develop at the end of the branch, while the binder rich portion of the feedstock with substantially lower viscosity still flows down to the side branch, often before the tip is fully filled, as it is shown in Fig. 31. The zig-zag mold design often provides the basic testing of the suitability of PIM feedstocks for molding (German 1997).

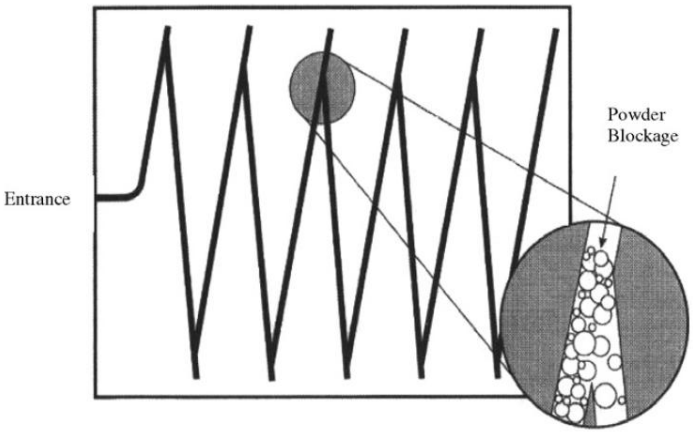

Fig.31 – Zig-zag test mold used for mouldability and separation tests (German 1997)

Furthermore, a phase separation during a flow through a square spiral mold has been studied by Jenni et al. (Jenni 2008, 2009). In this experiment differential scanning calorimetry (DSC) was used for quantifying the separation. A reference material (tungsten feedstock) with different powder loadings (30, 50, 60 vol.%) was examined and a correlation between changes of enthalpy and a binder content in these loadings was found. Afterwards, changes of a powder loading have been evaluated and quantified (Jenni 2008, Jenni 2009). The corner of the square spiral geometry has been selected as the most suitable location to determine the phase separation. First, it was divided horizontally into 3 regions/pieces. Every piece was 1 mm thick and divided to 64 small squares with 1 mm side length. Every square was examined on a DSC, and powder content was evaluated. After the measurement, the powder content 2D DSC patterns were obtained as shown in Fig. 32 (Jenni 2008).

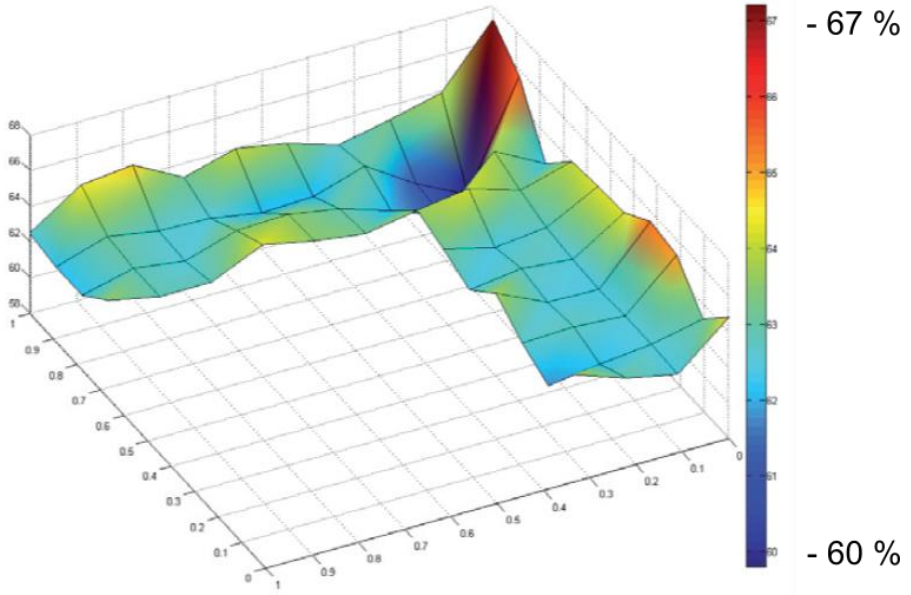

Fig. 32 – 2D DSC measurement of powder distribution in a molded sample (Jenni 2008)

The main disadvantages of this approach to determine a phase separation are inaccuracy, time consumption of sample preparation and post-process data evaluation.

Another possible method to quantify powder/binder distribution is a computer tomography, which represents a non-destructive method of a structure analysis of materials. Yang *et* al. (Yang, 2015) in his study presented an evaluation of defects inside a green body after injection molding with help of computed tomography (Fig. 33). According to his findings, pressure, temperature and injection rate are the keys to eliminate or minimize phase separation and pore formation process during injection molding. Therefore, it is

necessary to understand well the conditions inside molds, especially regarding a future automatization of a PIM process.

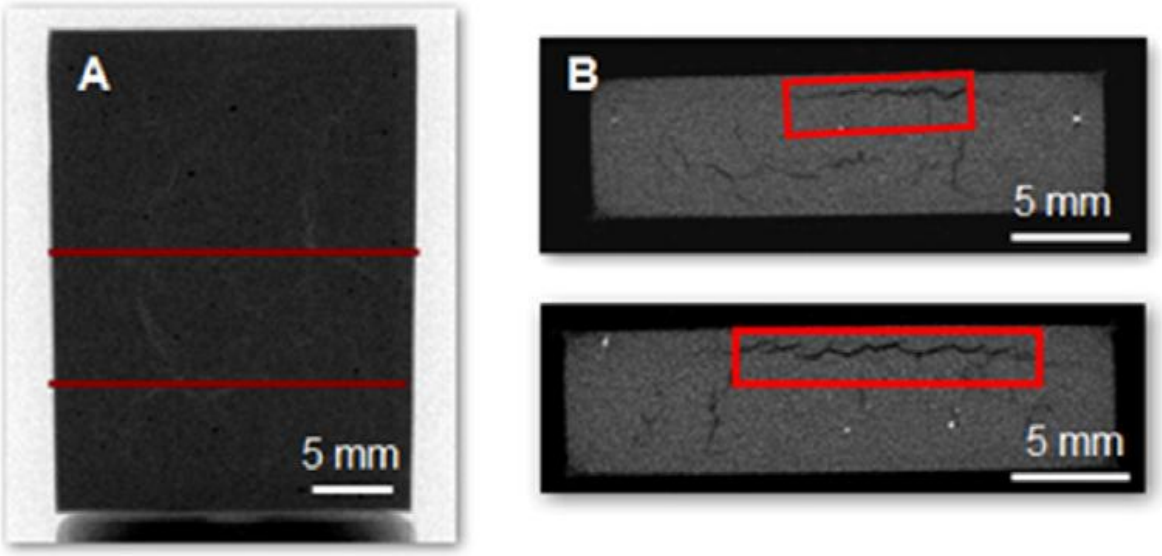

Fig. 33 – Computer tomography of PIM testing sample (a crack near surface visible on a right scan) (Yang 2015)

Recently, a new geometry to quantify phase separation (Fig. 34) has been developed at the Tomas Bata University in Zlin in cooperation with Fraunhofer IFAM, Bremen (Jiranek 2010). The testing sample consists of four sections and each section is connected with the 1 mm long gate in the section profile. The inner side length of first three sections and the outer side length of the last section is 10 mm. The mold cavity contains the inner and outer corners, the radical thickness variations, the areas with the weld lines and very thin film part, which is 0.3 mm deep (Hausnerova 2011).

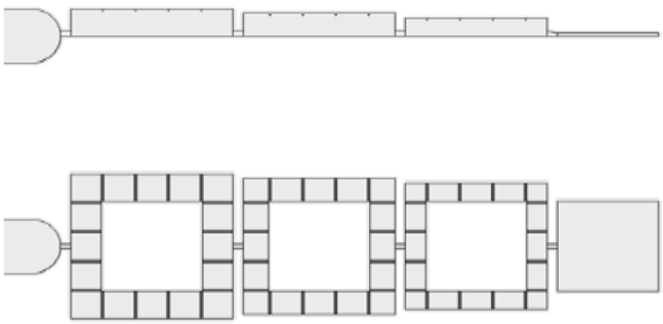

Fig. 34 - TBU/IFAM testing geometry (Hausnerova 2011)

On this geometry, the novel evaluation method based on a scanning electron microscopy with an energy dispersive X-ray (SEM/EDX) has been proposed (Hausnerova 2013). In the methodology, the quantitative EDX mapping as the measure of separation was carried out. To convert qualitative grayscale maps

into quantitative information, it was necessary to assign relative parameter, where 0 % represents purely white area and 100 % completely dark spots. Then, the concentration EDX maps of the powder and/or the binder elements after injection molding have been analyzed mathematically to obtain the single value - so called variability parameter. The variability parameter represents the size of the powder or binder non-uniformity within the tested PIM samples. To avoid inhomogeneities from local concentration imperfections, the EDX maps have been smoothed, when each pixel was considered as an average of (5 x 5) neighboring pixels (Hausnerova 2013). The whole process of quantitative analysis is visualized in Fig. 35.

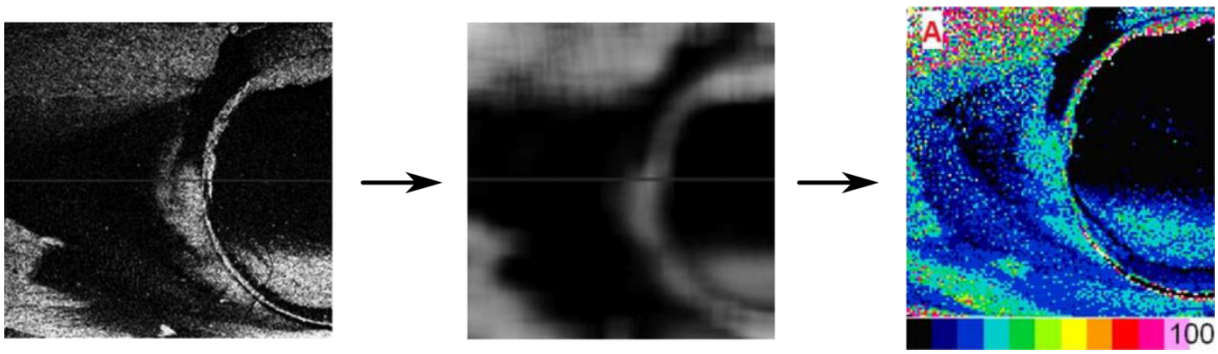

Fig. 35 - Evaluation of powder/binder content based on SEM/EDX analysis (Hausnerova 2013)

AIM OF THE WORK

The aim of this work is to propose a new view on a tool design for highly filled compounds. First task is to modify testing geometry for phase separation proposed recently by TBU and IFAM. Testing geometry intercepting main issue of injection molding of highly filled materials - phase separation - should consider findings of previous studies. Innovative approach to qualification of separation will be presented, on-line monitoring of a temperature inside mold cavity will be measured and related to simulation approach. This task has a promising commercial potential due to a current automation of production. Thanks to on-line temperature control, it will be possible to decide if part will be passed through, or grinded and re-used again in production. For this purpose, non-conventional methods of melt temperature recording will be used, specifically infrared (IR) sensors with quick response time. As additive manufacturing becomes a competitor to injection molding, the concept for production of molds from non-conventional materials for small batches will be introduced.
Main objectives of thesis are:

- material characterization for computational simulations of filling stage and Moldflow simulations of previous geometries for determination of phase separation during mold filling,
- design of a new testing mold for phase separation of highly filled PIM feedstocks with respect to previous studies,
- design of universal frame with inserts for temperature monitoring,
- correlation between Moldflow simulations of temperature profile and IR monitored temperature with the aim to determine the potential places of separation,
- experimental qualification of separation with computed tomography,
- design of testing geometry in universal frame for evaluation of weld lines of highly filled compounds, proposal of mold materials with respect to their thermal conductivity with the aim to affect mechanical properties of weld lines
- determination of tensile strength of weld lines for highly filled compounds used in conventional injection molding and PIM technology supplemented with statistical analysis.

4. METHODS

List of used molded materials:

- high-density polyethylene HD 6719 (Exxon Mobil Corp., USA) with low MFR (19 g/10min, 190 °C, 2.16 kg),
- MIM feedstock 17-4PH D 222E (PolyMIM, Germany) from X5 CrNiCuNb1 6-4 martensitic precipitation age hardenable stainless steel powder,
- WPC sawdust from processing of soft-wood, where particles with the smallest dimension above 400 μm was removed with a mesh analyser.

List of used mold materials:

- High-alloy, hot-work steel X38 CrMoV 5-1 material No. 1.2343 (Meusburger Georg GmbH & Co KG, Austria) for universal frame inserts,
- High-alloy, pre-toughened tool steel X33 CrS 16 material No. 1.2085 (Meusburger Georg GmbH & Co KG, Austria) with increased concent of chromium (16 %) and reduced thermal conductivity (18 $W.m^{-1}.k^{-1}$) for phase separation inserts,
- Unalloyed toolsteel C 45 U mat. No. 1.1730 (HASCO Hasenclever GmbH + Co. KG, Germany) for universal frame with good machinability.
- High strength aluminium alloy AlZn5Mg3Cu, EN AW 7022 (GLEICH Aluminiumwerk GmbH & Co. KG, Germany) for universal frame,
- Pure copper CW004A (ALMS spol. s r.o., Czech Republic) with 99.9 % copper content for universal frame,
- Bronze alloy CC493K (ALMS spol. s r.o., Czech Republic) for universal frame,
- high temperature resistant epoxy resin Gamod Fluid T206 (Dawex Chemical s.r.o., Czech Republic) with resistance up to 200 °C for universal frame,
- thermal filler hexagonal Boron Nitride 15/400 (3M Deutschland GmbH, Germany) with particle size distribution D_{90} up to 300 μm for universal frame,
- Mixture of acrylic monomer with photoinitiator (Stratasys, Ltd., Israel) as a VeroWhitePlus RGD 835 printing material for universal frame.

List of auxiliary materials:

- Isopropyl alcohol with 99.5 % purity (Lach-ner, s.r.o., Czech Republic)
- Silicon rubber Lukopren N1522 (Lučební závody, a.s., Czech republic)
- Lukopren Catalyst N as a cross-link agent for two-component silicon rubber (Lučební závody, a.s., Czech republic),

- methacrylated oligomers, monomers and photoinitiator (Formlabs Inc., USA) as a clear printing resin.

List of used equipment:

- Gas pycnometer Ultrafoam 1200e (Quantachrome GmbH, Germany) for evaluation of filler density,
- Differential scanning calorimetry DSC 1 (Mettler-Toledo s.r.o., Czech Republic) for measurement of specific heat capacity,
- C-therm TCi (C-Therm Technologies Ltd., Canada) with modified transient plane source technique for thermal conductivity measurement,
- Plasticorder PL 2000 (Brabender GmbH & Co KG) with twin screw extruder,
- High pressure capillary viscometer Rheograph 50 (GÖTTFERT Werkstoff-Prüfmaschinen GmbH, Germany) Rheometer,
- 3-axis milling machine HWT C-442 CNC (AZK, Czech Republic) for manufacturing of insert from easy to machine materials,
- 5-axis milling machine DMU 50 (DMG MORI, Germany) for steel machining of universal frame, frame inserts and testing geometry for phase separation,
- 3D printer Objet Eden 250 (Stratasys, Ltd., Israel) for mold insert with low thermal conductivity,
- 3D printer Form 2 (Formlabs Inc., USA) as a master model for creation of casted mold inserts,
- Injection molding machine Arburg 320 C (ARBURG GmbH + Co KG, Germany) for injection molding of highly filled compounds,
- Ejector type IR sensor EPSSZL (Futaba Corp., Japan) for temperature measurement in range of (60-430) °C,
- Pre-amplifier EPT-JB001 (Futaba Corp., Japan) for transformation of
- Main-amplifier EPT-001S (Futaba Corp., Japan) for IR sensor signal,
- Universal datalogger Almemo 2590 (Ahlborn Mess- und Regelungstechnik GmbH, Germany) for recording of measured data from IR sensors,
- Analogue circular thermostat (IKA-Werke GmbH & Co. KG, Germany) for water debinding bath,
- Sintering furnace MIM 3616 (Clasic, s.r.o., Czech republic) with molybdenum heating elements,
- Desktop scanning electron microscope Phenom Pro 2000 (Thermo Fircher Scientific Inc., USA),

- Computed tomography Phoenix V|tome|x L240 (General Electric Co., USA) with acceleration voltage of 300kV/500W and micro-focus tube,
- Universal testing machine Zwick Roell 1456 (Zwick Roell Group, Germany) for tensile strength characterization.

List of softwares:

- Autodesk Moldflow Data Fitting 2018 (Autodesk, Inc., USA) for material characterization for CAE simulations,
- CATIA V5R19 (Dassault Systems) for CAD modelling, mold designing and drawings,
- Autodesk Moldflow Synergy 2016 (Autodesk, Inc., USA) for CAE simulations,
- Autodesk Netfabb Premium 2018 (Autodesk, Inc., USA) for mesh optimisation and generation,
- PreForm (Formlabs, Inc., USA) for 3D printing model preparation,
- Minitab 18 (Minitab, Ltd., United Kingdom) for statistical evaluation of sSimilarities.

For rheological measurement, a capillary rheometer with control-rate mode, where a piston speed is monitored and afterwards converted to shear rate, was used. Capillary used for measurement has flat entrance geometry and dimensions 20 mm and 1 mm for length and diameter, respectively.

To measure density of sawdust for WPC filled compounds, gas pycnometer was employed, where a sealed chamber with sawdust was pressurized with a helium gas and obtained pressure was recorder. Afterwards, pressure was transferred to an empty sealed chamber, whose volume is also known and again, pressure is recorded. According to pressure drop between the testing and the reference chamber it is possible to specify the density of the tested sample. Final density was obtained as an arithmetic mean of three measurements.

For computer simulations, Autodesk Moldflow Synergy 2016 was utilized. According to small thickness of the parts, the dual domain mesh type with at least 10 elements through the part thickness has been selected. Obtained data from material characteristics were fitted in Autodesk Moldflow Data Fitting 2018, exported as the database file and imported into the Moldflow simulation. First, simulations were performed to verify previous findings of Jenni (2009) and Hausnerova (2013) in the area of phase separation, second, simulation of temperature development in the particular selected points of the new proposed mold design to intercept separation.

Tools were designed for Arburg 320C, which is suitable for highly filled materials causing an abrasive wear on mold and molding equipment with clamping force of 70 tones and D = 20 mm in case of screw from injection unit.

Machining of the universal frame and all inserts for testing was done on 3-axis and 5-axis milling machines with SECO tools with suitable geometry for currently machined material.

3D printing of mold insert was done with the help of Objet Eden 250 with 25 μm layer thickness, and master model for casting of silicone mold and, subsequently mold insert from epoxy resin, was done on Formlabs Form 2 3D printer with 50 μm layer thickness.

For mechanical testing, Zwick Roell 1456 machine was used. Due to expectation of high tensile properties, samples were clamped into pneumatic grippers. Testing speed profile was divided into two regions according to ČSN EN ISO 6892-1:

- evaluation of Young modulus up to 0.2 % of relative elongation, where speed was set to 5 mm/min,
- determination of ultimate strength under speed of 20 mm/min.

Then, the ultimate strength was calculated as:

$$R_m = \frac{\sigma_{\max}}{\varepsilon}$$

where, σ_{max} [MPa] is uniaxial stress and ε is corresponding elongation [%].

Testing specimen was designed with respect to EN ISO 2740:2009 - Sintered Metal Materials, Excluding Hardmetals - Tensile Test Pieces. According to Hausnerova *et* al. (Hausnerova, 2014b) one discrepant dimension has been received from MPIF standard - Preparing and Evaluating Metal Injection Molded (MIM) Sintered /Heat Treated Tension Test Specimens. Fundamental dimensions are depicted in Fig. 36.

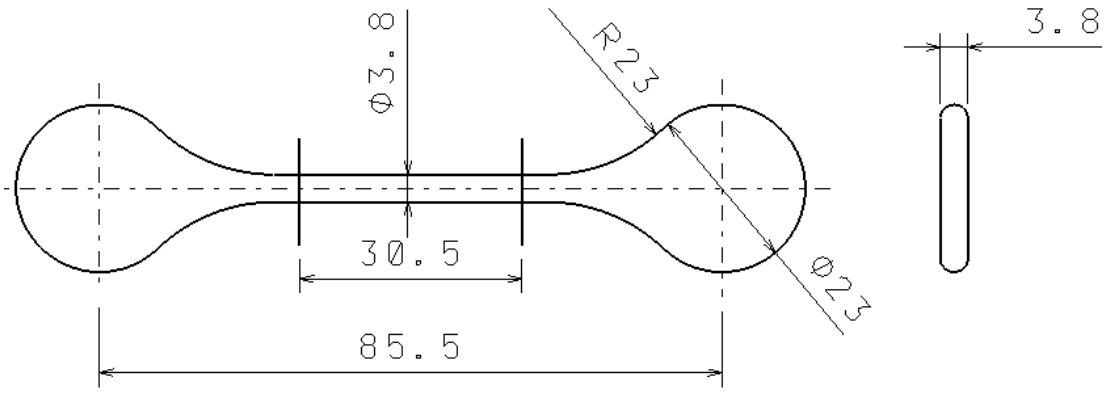

Fig. 36 - Dimensions of Tensile Test Specimens

4.1 Statistical Data Analysis

For determination of an outlier value, Grubbs test (Grubbs, 1969) was selected. Grubbs test is performed as hypothesis test, which is defined as:

H_0: in the data sample is no outlier,
H_a: the maximum or minimum value in the data sample is an outlier
at a significance level of $\alpha = 5$ %

Grubbs test G can be defined as one sided:

$$G = \frac{\bar{x} - x_{\min}}{s} \xrightarrow{or} \frac{x_{\max} - \bar{x}}{s}$$

or for both sides:

$$G = \max\left\{\frac{\bar{x} - x_{\min}}{s}, \frac{x_{\max} - \bar{x}}{s}\right\}$$

where $\bar{x}$ is devoted to arithmetic mean of data sample, x_{min} is a minimum data value, x_{max} is maximum data value a s is standard deviation of the sample data. The p-value is for one-sided test is then estimated as:

$$P \approx nP\left(T \geq \sqrt{\frac{n(n-2)G^2}{(n-1)^2 - nG^2}}\right)$$

or for both sides test:

$$P \approx 2nP\left(T \geq \sqrt{\frac{n(n-2)G^2}{(n-1)^2 - nG^2}}\right)$$

where, n is number of observations and T is a random variable distributed as a T-distribution with n-2 degrees of freedom.

For a normality test, Anderson-Darling method was used. Two hypotheses were established:

H_0: the data sample is drawn from a population with the normal distribution,
H_a: the data sample is drawn from a population with another distribution
at a significance level of $\alpha = 5$ %.

The Anderson-Darling statistic *AD* is expressed by formula:

$$AD = -n - \frac{1}{n}\sum_{i=1}^{n}(2i-1)\left[\ln F(X_i) + \ln(1 - F(X_{n-i+1}))\right]$$

where n is the sample size, $F(X_i)$ is cumulative distribution function for the specified distribution, and i is the number of samples when they are sorted in ascending order.

According to small sample size (n=10) the Anderson-Darling test value has been adjusted with respect to Jäntschi *et* al. (Jäntschi, 2018):

$$AD_{adj} = AD\left(1 + \frac{0.75}{n} + \frac{2.25}{n^2}\right)$$

Therefore, for 10 sample size data of population Anderson-Darling test value has been multiplied with the constant of 1.0975. With respect to D'Augostino *et* al. (D'Augostino, 1986) findings of different *p*-values associated to the Anderson-Darling statistics with a correction for small sample size. Formulas for the calculation of *p*-value for different Anderson-Darling adjusted statistics are depicted in Table 5.

Table 5 – Formula for *p*-value according to the value of Anderson-Darling statistic

Anderson-Darling Statistic	**Formula for *p*-value Calculation**
$AD_{adj} \geq 0.60$	$\exp(1.2937 - 5.703(AD_{adj}) + 0.0186(AD_{adj})^2)$
$0.34 < AD_{adj} < 0.60$	$\exp(0.9177 - 4.279(AD_{adj}) - 1.38(AD_{adj})^2)$
$0.20 < AD_{adj} < 0.34$	$1 - \exp(-8.318 + 42.796(AD_{adj}) - 59.938(AD_{adj})^2)$
$AD_{adj} \leq 0.20$	$1 - \exp(-13.436 + 101.14(AD_{adj}) - 223.73(AD_{adj})^2)$

To test the equal variances, Levene test was employed with the following hypotheses:

H_0: all variances are equal,
H_a: not all variances are equal
at significance level of $\alpha = 5\%$

If the resulting *p*-value is greater than adequate choice of α value, the null hypothesis of equal variances fails to be rejected, and it is confident that the assumption of the equal variances is met.

Levene statistic is defined as:

$$W = \frac{(N-k)}{(k-1)} \frac{\sum_{i=1}^{k} N_i (\overline{Z_{i.}} - \overline{Z}_{..})^2}{\sum_{i=1}^{k} \sum_{j=1}^{N_i} (Z_{ij} - \overline{Z}_{i.})^2}$$

where the size of samples N is divided into k sub-groups, and N_i is the sample size of Z_i–group. Z_{ij} can be defined as mean, median or 10 % trimmed mean value with the respect to the maximum robustness and power of Levene test. According to Derrick *et* al. (Derrick, 2018), for equal of variances test, the median values will be used because of highest robustness of the test.

The calculated Levene test statistic is afterward compared with the upper critical value of F-distribution at a significance level of α. Levene test rejects the null hypothesis that the variances are equal if:

$$W \geq F_{\alpha,k-1,N-k}$$

where F is upper critical value with k-1 and N-k degree of freedom at confidence level of α.

For comparison of the sample data means, one-sided ANOVA method was used. For application of ANOVA two conditions must be accomplished:

- Sample data must origin from specified distribution,
- Sample variance must be equal.

Analysis of variance tests the hypothesis that the means of sample populations are equal. Hypothesis was compiled as:

H_0: all population means are equal,
H_a: at least one population mean is different
at significance level of α = 5 %

One-way ANOVA test statistic is derived from:

$$F = \frac{MST}{MSE}$$

where *MST* means sum of squares due to treatment, and *MSE* represents sum of squares due to error.

$$MST = \frac{SST}{p-1}$$

where *SST* is sum of squares due to treatment and *p* is the overall number of measurements.

$$SST == \sum_{i=1}^{k} n\left(\bar{x}_i - \bar{x}_{overall}\right)^2$$

where *n* is total number of samples in population, x_i is value of arithmetic mean according to *i-th* sub-group, and $\bar{x}$ is arithmetic mean of the sample data.
Denominator is determined in formula:

$$MSE = \frac{SSE}{N - p}$$

where *SSE* is sum of squares due to error, *N* is total number of observations.

$$SSE = \sum_{i=1}^{k} (n-1)s_i^2$$

where *s* is standard deviation. If value of ANOVA test statistic is higher than critical value, it is possible to reject null hypothesis with significance level of α.

Cluster analysis is focused on an establishment of clusters, where cases within the cluster are more similar to each other than are cases in next clusters. Jain *et* al. (Jain, 1999) defined several clustering methods, and the hierarchical clustering method has been selected for this Thesis.

Rearranging into the groups was done with Ward method, where the distance between two clusters is the sum of squared deviations from points to centroids. Distance is calculated with matrix (Kiss, 2017):

$$d_{mj} = \frac{(N_j + N_k)d(j,k) + (N_j + N_l)d(j,l) - N_j d(k,l)}{N_j + N_m}$$

where *N* is the number of variables in *j,k,l,m* clusters.
Distance between two observations was calculated by Euklidean method, where the distance in *n*-dimensional space is defined as (Murtagh, 2011):

$$d^2(p,q) = |p_1 - q_1|^2 + |p_2 - q_2|^2 + \ldots + |p_n - q_n|^2 = \sum_{j=1}^{n} |p_j - q_j|^2$$

The ordinary method of least squares is a statistical method used in linear regression. In linear regression, the dependent variable is defined as:

$$Y = \alpha X + \beta + \varepsilon$$

where α is slope of fitting curve, β is intercept defining Y when X=0, and ε is residual or error of fitting.

To fit the curvature of the sample data, the polynomial regression is used often:

$$Y = \beta_0 + \beta_1 x_i + \beta_2 x_i^2 + ... + \beta_n x_i^n + \varepsilon$$

where n is the degree of polynomial regression.

5 RESULTS AND DISCUSSION

5.1. Material characterization

The highly filled compounds (WPC and PIM) were characterized with the respect to flow simulations. Wood sawdust as a waste material was separated from large fraction above 400 μm with mesh analyzer and afterwards density was characterized with gas pycnometer Ultrafoam 1200e in helium. As a result, density of 0.196 g/cm^3 was obtained. To prepare highly-filled WPC feedstock, first HDPE polymer matrix with sawdust was mixed in ratio 50:50 vol.%. Subsequently, the mixture was further homogenized by extrusion using a twin screw extruder (nozzle temperature: 200 °C, Zone 2: 190 °C, Zone 1: 180 °C, screw rotations: 50 rpm) and granulated. Second highly filled testing material is commercially available MIM feedstock PolyMIM 17-4PH D 222E.

5.1.1. Thermal Conductivity

Thermal conductivity are necessary for determination of cooling rates. Insert materials with the lower thermal conductivity than molded material (17-4PH) were selected with the purpose to maximize the packing phase in molding cycle. Thermal conductivity was measured with C-therm device, where modified transient plane source technique is used. A known current is applied to a sensor's heating element providing a small amount of heat. The current applied to the coil results in the temperature elevation at the interface between the sample and the sensor, subsequently the voltage drop is inducted. Testing samples were machined (in case of copper, aluminium, steel 1.2085, bronze), casted (epoxy resin, epoxy resin + 35vol.% hexagonal boron nitride - hBN), pressed (PIM 17-4PH, WPC) or 3D printed. Testing sample dimensions were 20 mm in diameter and 12 mm/22 mm in height for thermal conductivity bellow/above 90 W.m^{-1}.k^{-1}, respectively.

Table 6 - Thermal conductivity for tested feedstocks and insert materials

Material	$\bar{x}$	s	v
	[MPa]		[%]
Copper	383.941	14.860	3.870
Aluminum	154.024	2.164	1.405
Bronze	64.198	1.504	2.343
Steel 1.2085	17.276	0.311	1.800
Epoxy resin + 35% hBN	0.992	0.015	1.541
Epoxy resin	0.390	0.007	1.700
3D printed	0.204	0.007	3.656
PIM 17-4PH	4.155	0.145	3.483
WPC	0.205	0.005	2.600

5.1.2. Rheology

Viscosity curves were obtained for three temperatures - 180, 190, and 200 °C. The data is depicted in Table 6.

Table 7 – Viscosity curves for 17-4PH and three different temperatures

Temperature	Shear rate	Shear stress	Viscosity
[°C]	[s^{-1}]	[Pa]	[Pa.s]
180	35	76903	2197
	60	94641	1577
	100	115500	1155
	170	145565	856
	290	184343	635
	490	233995	477
	830	297518	358
	1410	371660	263
	2400	491193	204
	4000	657984	164
190	35	76026	2172
	60	92999	1549
	100	112516	1125
	170	137518	808
	290	172191	593
	490	217313	443
	830	271990	327
	1410	340271	24
	2400	436568	181
	4000	561143	140
200	35	75150	2151
	60	91356	1528
	100	109532	108
	170	129470	765
	290	160040	550
	490	200630	412
	830	246463	281
	1410	308883	219
	2400	381943	169
	4000	464301	121

5.1.3. Specific Heat Capacity

For deceleration reason of cooling rate due to phase transformation, a specific heat capacity c_p of molding materials was measured. The data is crucial for simulation of temperature profiles in pre-selected areas, and finding of regression function. Specific heat capacities were evaluated from DSC measurement with 90 °C/min cooling rate.

Table 8 - Specific heat capacity for selected temperatures for 17-4PH

Temperature [°C]	**30**	**50**	**55**	**60**	**65**	**70**
c_p **[J/g^{-1}.°C]**	0.435	0.601	0.772	1.083	0.721	0.611
Temperature [°C]	80	90	100	110	120	130
c_p **[J/g^{-1}.°C]**	0.623	0.537	0.542	0.463	0.421	0.411

5.1.3. Sample Preparation

For injection molding, Arburg 320C suitable for highly filled materials, was used. Processing conditions for the phase separation testing mold and injection molding of MIM feedstock PolyMIM 17-4PH D222E are described in Table 9. Temperature profile was set with respect to material datasheet recommendations, and pressure was adjusted to fullfill the injection mold cavity.

Table 9 - Parameters of injection molding for 17-4PH feedstock for phase separation

Separation Mold	Nozzle	Zone5	Zone 4	Zone 3	Zone 2	Zone 1
Barrel Temperature [°C]	180	176	172	168	164	160
Mold Temperature [°C]	65					
Injection Pressure [bar]	2200					
Injection Speed [mm/s]	100					
Switch-over method	piston distance					
Switch-over value	95% of injected volume					
Holding Pressure 1 [bar]	2000					
Duration 1 [s]	0.5					
Holding Pressure 2 [bar]	2200					
Duration 2 [s]	3.0					
Holding Pressure 3 [bar]	400					
Duration 3 [s]	0.5					
Cooling Time [s]	30					

In case of testing of the influence of the thermal conductivity of mold inserts on the mechanical properties, namely the tensile strength, processing conditions are

listed in Table 10 for PolyMIM 17-4PH feedstock and in Table 11 for WPC compound. Injection pressure was determined as requested pressure to full-fill the insert from copper with the highest pressure drop due to rapid solidification, and for all next inserts was the same to keep comparability of the results.

Table 10 - Parameters of injection molding for 17-4PH for insert testing

17-4PH Insert Mold	Nozzle	Zone 5	Zone 4	Zone 3	Zone 2	Zone 1
Barrel Temperature [°C]	180	176	172	168	164	160
Mold Temperature [°C]	45					
Injection Pressure [bar]	1500					
Injection Speed [mm/s]	50					
Switch-over method	piston distance					
Switch-over value	95% of injected volume					
Holding Pressure 1 [bar]	1400					
Duration 1 [s]	0.5					
Holding Pressure 2 [bar]	1300					
Duration 2 [s]	3 (metal inserts), 10 (polymeric inserts)					
Holding Pressure 3 [bar]	200					
Duration 3 [s]	0.5					
Cooling Time [s]	120					

Table 11 - Parameters of injection molding for WPC for insert testing

WPC Insert Mold	Nozzle	Zone 5	Zone 4	Zone 3	Zone 2	Zone 1
Barrel Temperature [°C]	200	195	190	185	180	170
Mold Temperature [°C]	45					
Injection Pressure [bar]	1700					
Injection Speed [mm/s]	50					
Switch-over method	piston distance					
Switch-over value	95% of injected volume					
Holding Pressure 1 [bar]	1550					
Duration 1 [s]	0.5					
Holding Pressure 2 [bar]	1400					
Duration 2 [s]	3 (metal inserts), 10 (polymeric inserts)					
Holding Pressure 3 [bar]	200					
Duration 3 [s]	0.5					
Cooling Time [s]	120					

Requested holding pressure is calculated as 80 % of maximum filling pressure, and duration of this phase should last up to the solidification of the smallest cross-section of flow domain - gate. Therefore, if thermal conductivity of inserts was below feedstock conductivity (polymeric inserts), duration of packing was set to 10 s (and vice versa for metal inserts with 3 s duration).

For debinding of PolyMIM 17-4PH, a two step binder removal method was used. In first step, green parts were soaked in distilled water with 2 vol.% of corrosion inhibitor (Inhibitor 4000, Zschimmer & Schwarz). Water soluble binder was dissolved for 18 h at temperature 60 °C. After first stage of debinding, the green parts were dried in oven at 80 °C for 6 hours.

Table 12 - Weight and weight loss of 17-PH feedstock before/after debinding stage

	Weight [g]		Loss [%]
	Before	After	
Separation Mold	45.253	43.612	3.6
Insert Mold	17.862	17.199	3.7

Second stage of debinding was performed as thermal debinding at elevated temperature as a part of sintering cycle.

After drying, parts were placed on sintering plates made of Al_2O_3 due to higher sintering temperature of ceramic and no bonding between parts and sintering plate. Pure nitrogen at the pressure of 300 Pa was used as a sintering atmosphere. Sintering cycle was set with the respect to the material datasheet; temperature profile is visualized in Fig. 37.

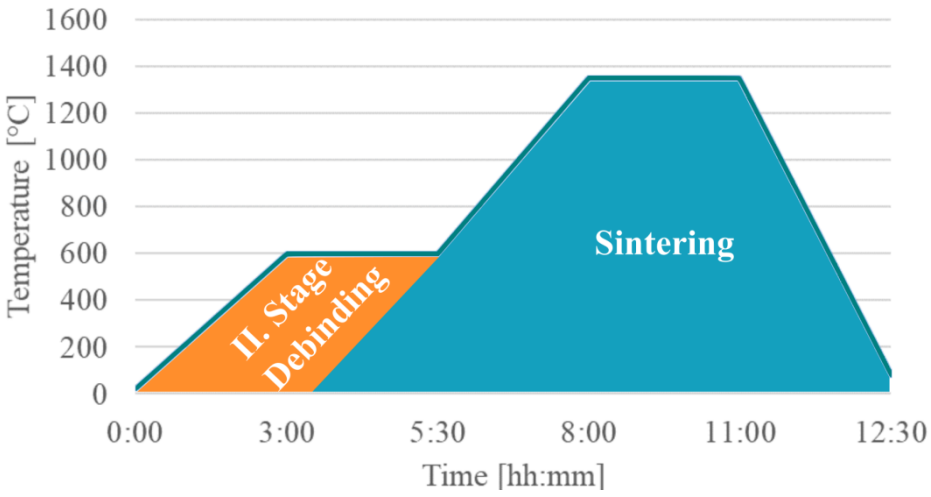

Fig. 37 – Temperature profile for second stage of debinding and sintering of 17-4PH stainless steel PIM parts

5.2. Mold Concept for Universal Frame

Universal mold frame for phase separation test insert and inserts with different thermal conductivity was designed. This frame is characterized by versatility, where core and cavity plates are in a form of inserts, and therefore, one frame is used for both issues. The tool consists of standards used in toolmaking, and cavities in plates are tailored to research needs. Therefore, sprue bushing on universal frame is made from 1.2826 tool steel hardened up to 54 HRC. All other parts are in no-contact with highly filled polymeric melt, thus for plates unalloyed tool steel 1.1730 without hardening was used due to its excellent machinability.

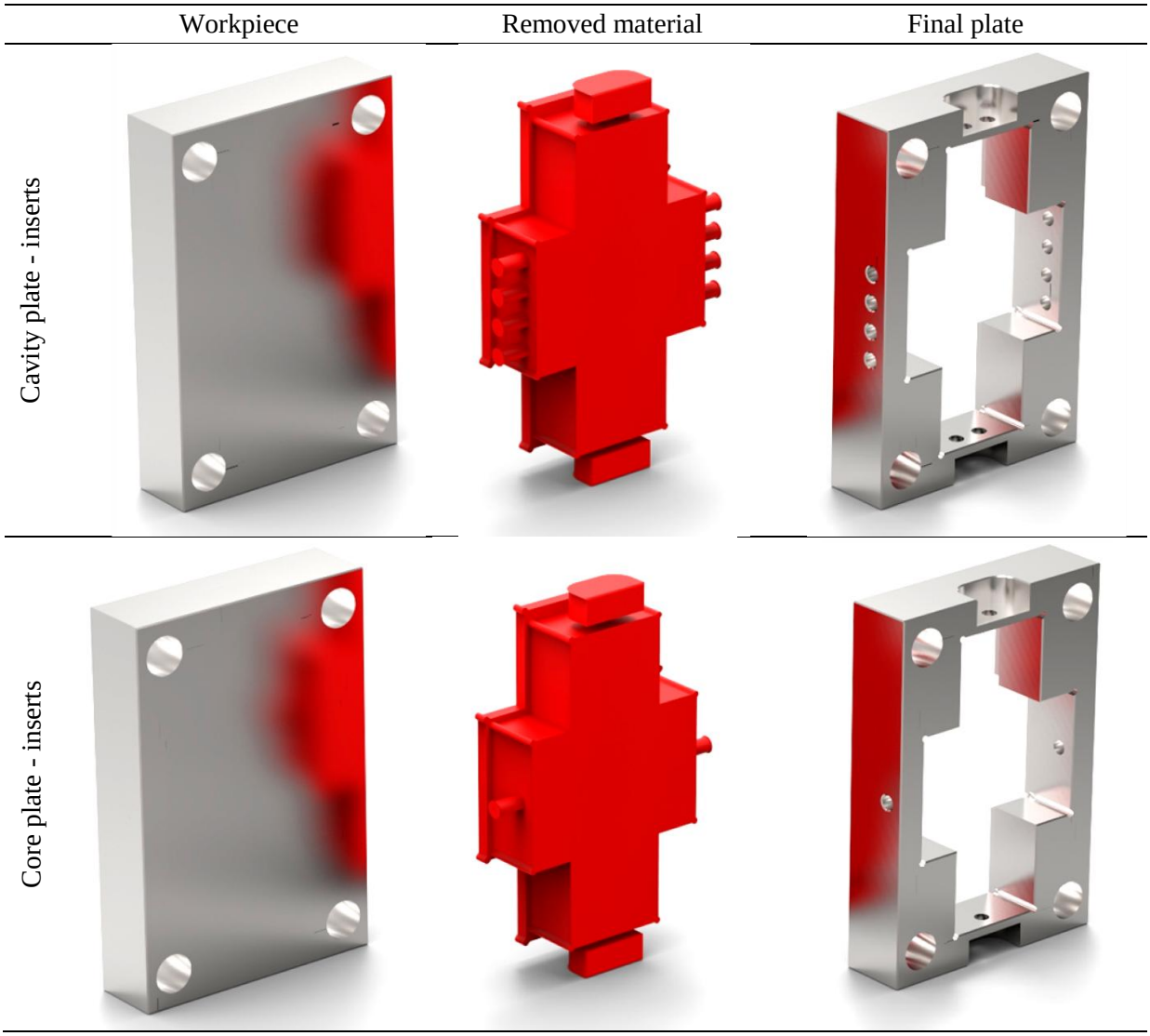

Fig 38 - Comparison of standard plate (left), removed material (middle) and final plate (right) for cavity plate (top) and core plate (bottom)

Design of suitable inserts for universal frame for phase separation and weld line study is proposed and drawings are attached to the work.

5.3. Mold Concept and Verifications for Phase Separation

Based on the previous studies in the field of phase separation during flow of filled compounds (Hausnerova, 2011, German, 1997, Jenni, 2008, Jiranek, 2010), a new mold design is proposed. The testing sample should respect features, which are supporting segregation of powder from binder. Molds for highly filled compounds as those used in powder injection molding obviously contain not only one feature supporting phase separation, but a combination of several elements: dead branches, sudden cross-section profiles changes, outer corners, weld lines. Following this consideration it is necessary to ask the question, how the combination of critical features will affect an overall phase segregation. Previous findings of phase separation was compared to Moldflow simulations for better understanding to design approach.

Square spiral has been meshed by more than 200,000 tetrahedron elements with 1 mm edge length. In region of interest the 3D mesh was densified and element edge length was decreased to 0.2 mm. Simulated material was 17-4PH feedstock. Its rheological properties, specific heat capacity and thermal conductivity were, with support of Autodesk Moldflow Data Fitting, fitted to constants used in Cross model, where temperature-induced physical changes are predicted with Williams-Landel-Ferry equation (WLF). Both models were used in afterwards Moldflow simulation, where filling of current testing molds were simulated. Temperatures of melt and mold have been set on 180 °C and 60 °C, respectively. Filling stage was controlled by flow rate of 20 cm^3/s and evaluation was focused on third corner of testing geometry as was done by Jenni (Jenni, 2008) in Fig. 32 . From results of Jenni's measurement of phase separation with X-ray tomography (Fig. 39, right) it is evident that differences in absorbed X-ray, and therefore different density of final structure trends to copy shear rate distribution (Fig. 39, middle).

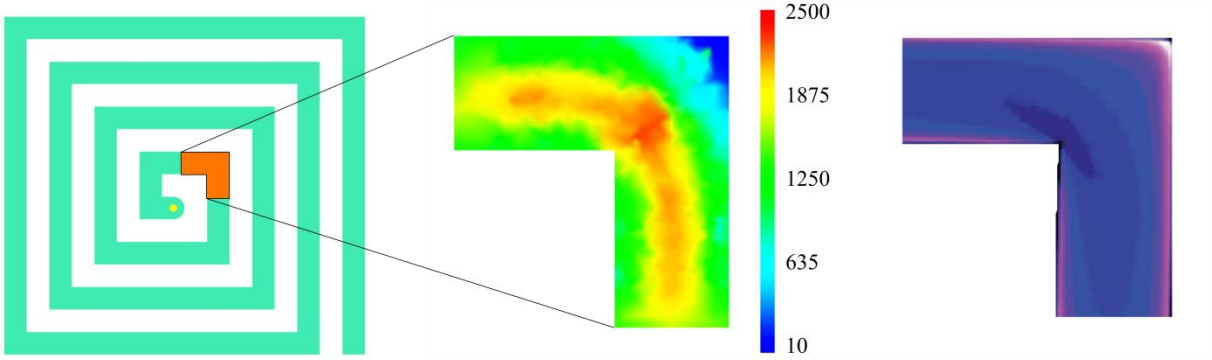

Fig. 39 – Maximum shear rate during filling stage (middle) for Jenni's geometry testing mold with reported phase separation after injection displayed by CT, (right) for 20 cm^3/s flow rate

First, simulation of injection molding stage of testing mold designed in cooperation between TBU and IFAM was performed. Material for simulation

was 17-4PH feedstocks as in previous case with the same processing conditions. 3D model was discretized with 266,000 tetrahedron elements with 0.5 mm edge length. From the simulation (Fig. 40, left) it is evident that the deviation of shearing intensity from the bulk shear rate represents the area, where the phase separation occurred in the real sample, see SEM micrograph in Fig. 40, right.

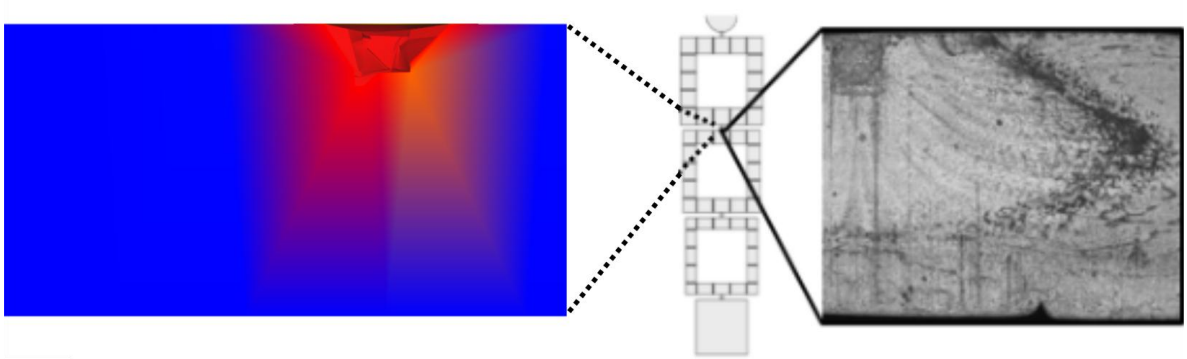

Fig. 40 – Maximum shear rate during filling stage (left) for TBU/IFAM testing mold with reported phase separation after injection displayed on SEM (right) for 20 cm^3/s flow rate

Pursuant to findings of this analysis, a new mold design has been developed with number of supporting elements for phase separation. The mold concept is based on dead branches (Fig. 41) as proposed also by German *et* al. (German, 1997), where phase separation occurs due to different momentums of powder and binder.

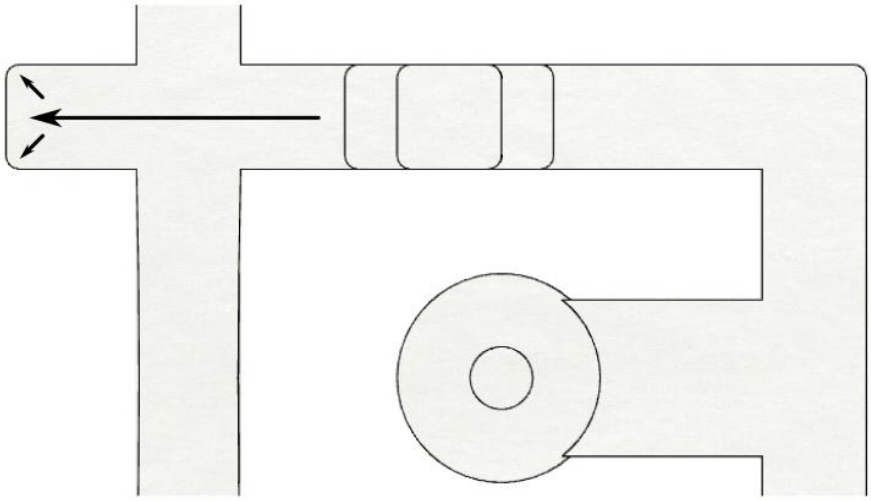

Fig. 41 - Incorporation of dead branches into new testing mold design

Following the finding of Jenni *et* al. (Jenni, 2009) and Hausnerova *et* al. (Hausnerova, 2013), the phase separation occurs in the areas along the sharp corners and the cross section changes, respectively. Therefore, the proposed design consists of combination of both supporting elements and design of this feature is shown in Fig. 42.

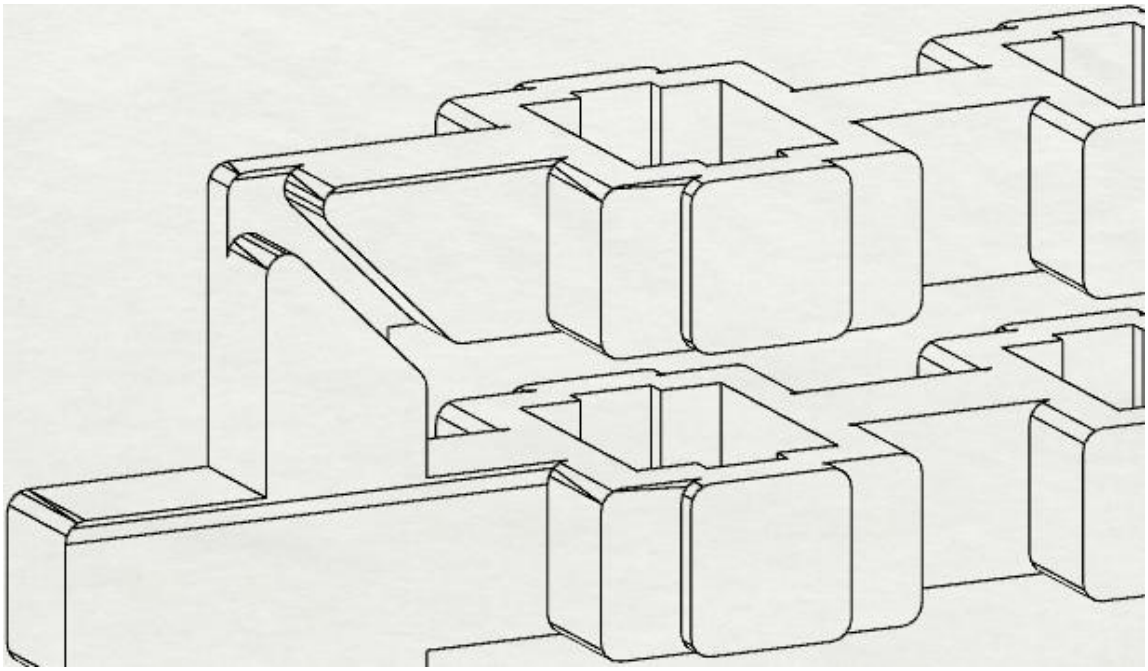

Fig. 42 - Sharp corner at sudden cross-section change in new testing mold design

Further, the proposed design allows to study properties of weld lines due to obstacles incorporated in testing geometry (Fig. 43).

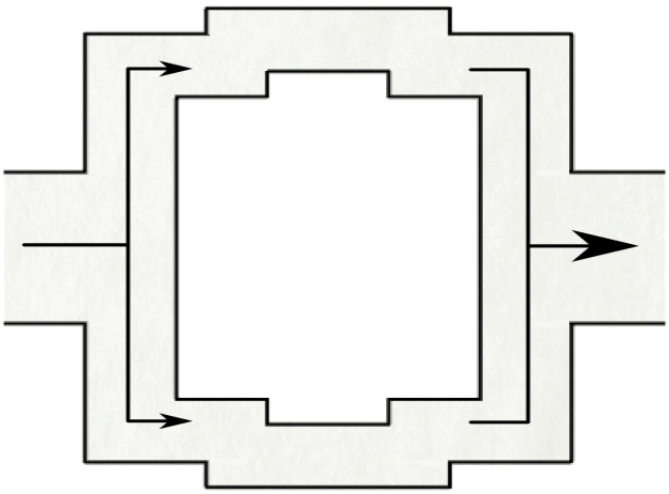

Fig. 43 - Weld line formation due to obstacle in new testing mold

These obstacles create multiple weld lines, which mechanical properties will be investigated, and effect of multiple weld line will be evaluated (Fig. 44).

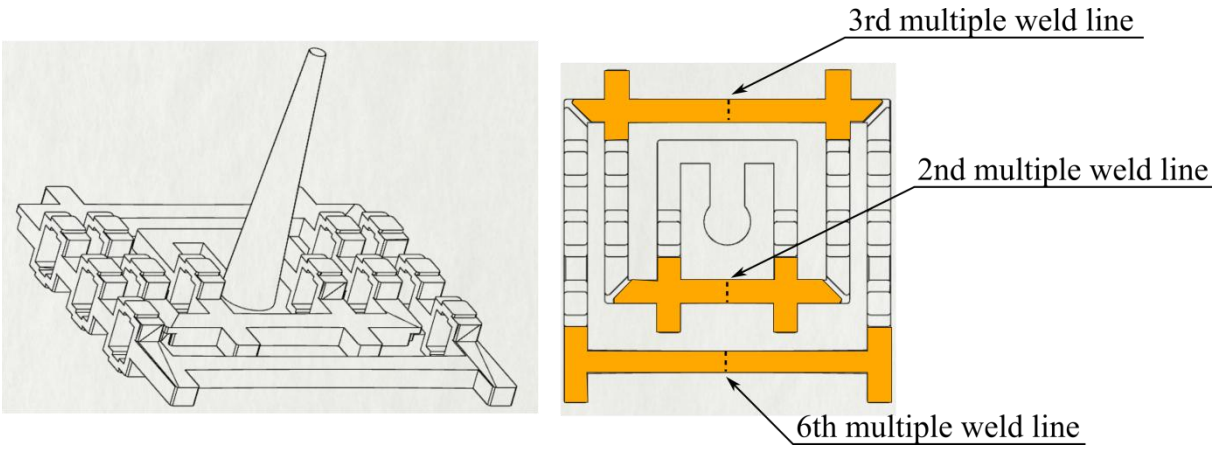

Fig. 44 - Multiple weld lines integrated in new testing mold design

The final geometry of new testing mold concept was registered as the utility model with the registration number CZ 2014-30495 U1. The geometry was designed using Moldflow simulation SW with the same processing conditions and material as in previous verifications (17-4PH, Table 9). Generated 3D mesh consists from 400,000 tetrahedron elements with 0.8 mm edge length. The result of shear rate development is depicted in Fig 45, where it is evident that the element with the highest potential to phase separation is are the sharp corners at the sudden cross-section changes.

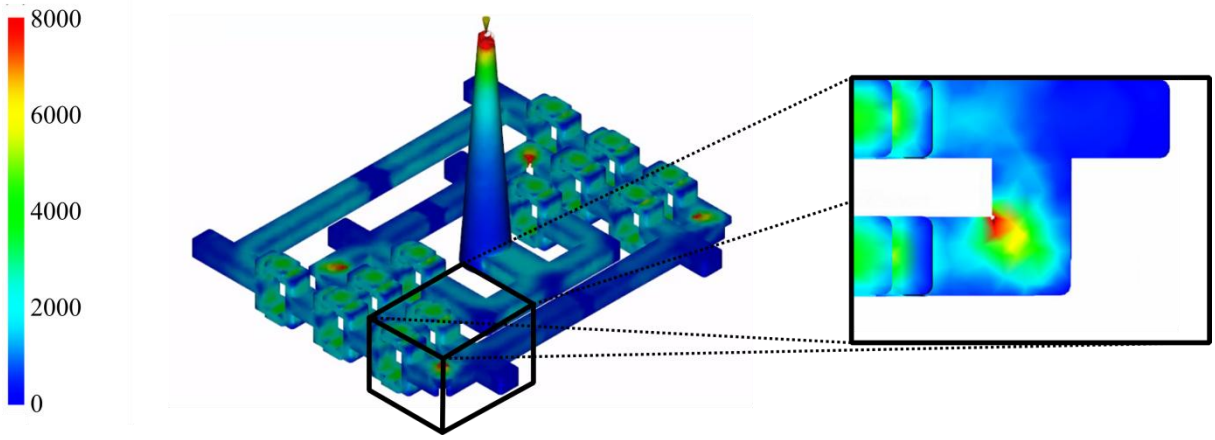

Fig. 45 - Simulation of shear rates (s^{-1}) of new testing mold for 17-4PH feedstock and conditions described in Table 9

According to moldability of the designed part, small changes needed to be done, Fig.46. To ensure the part position on the moving side of the mold after opening, it was necessary to add a fillet on the side, which is in contact with the stationary plate. There are no undercuts on the part and the right position during opening of the mold is supported with no-bevel on the side molded in the moving plate. This solution could lead to a higher ejection force, and consequently, deformation or damage of molded parts. To minimize the stress

concentration in the investigated area (the corner with the sudden cross-section change, Fig. 42), the outer corner was rounded with *R*=1.5 mm. Number of obstacles was reduced due to the absence of formation of a simple weld line. Shape of obstacles was changed from rectangular to cylindrical.

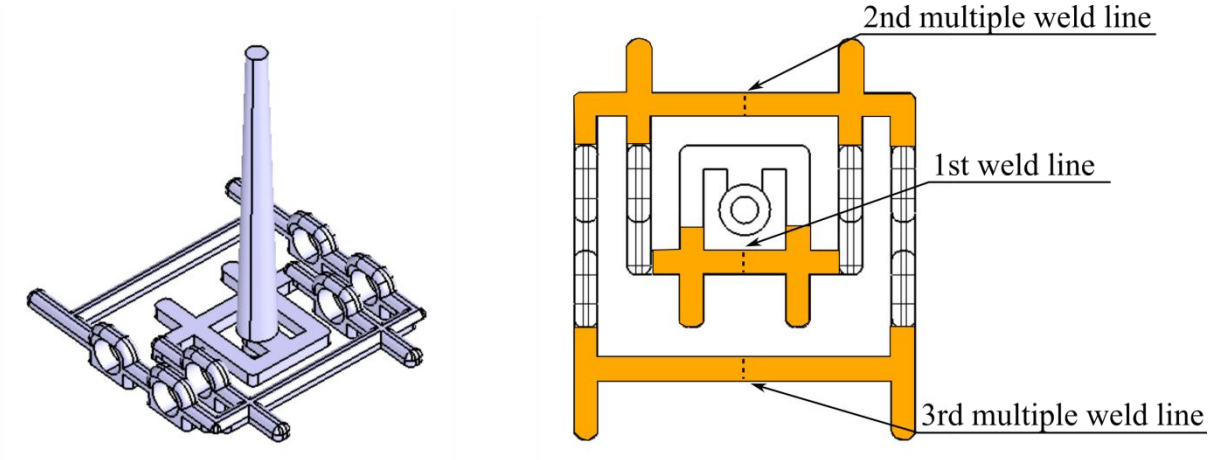

Fig. 46 - Modified testing mold to enhance moldability

Afterward, the flow in the modified testing geometry was simulated again. Model was discretized with a tetrahedron mesh. Due to the presence of the rounded elements, which cannot be neglected, the edge length of the element was set to 0.25 mm, and the number of elements exceed 1,150,000.

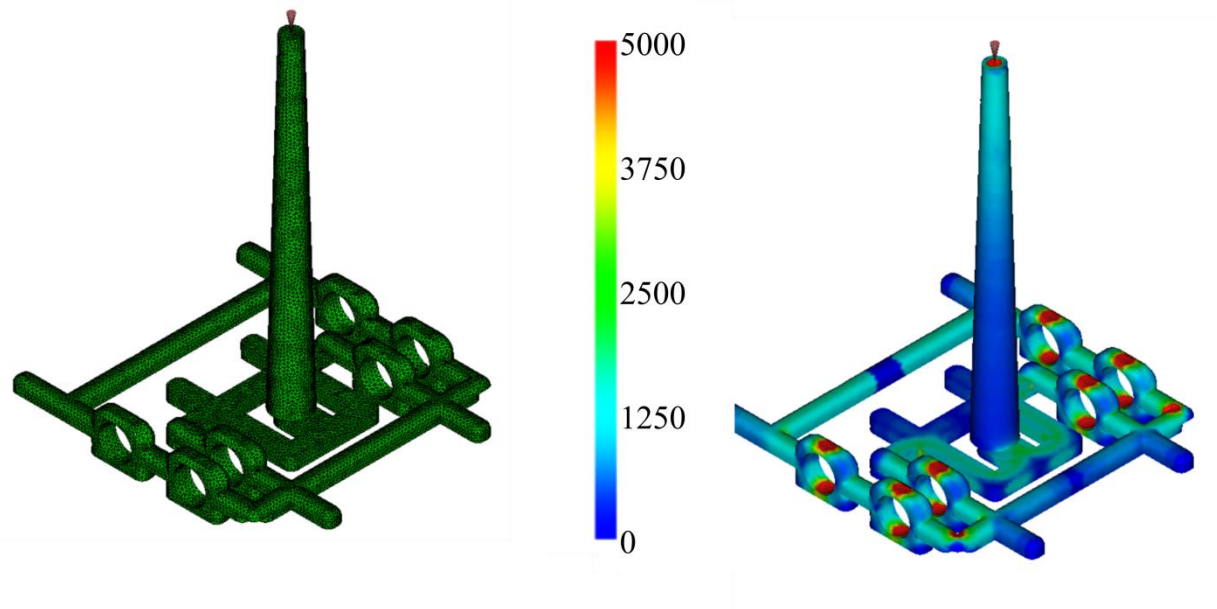

Fig. 47 - Simulation of shear rate (s^{-1}) of final testing mold for 17-4PH feedstock at conditions described in Table 9

During the simulation, the positions of 6 infrared (IR) sensors was determined as shown in the Fig. 48 displaying the temperature distribution in the mold.

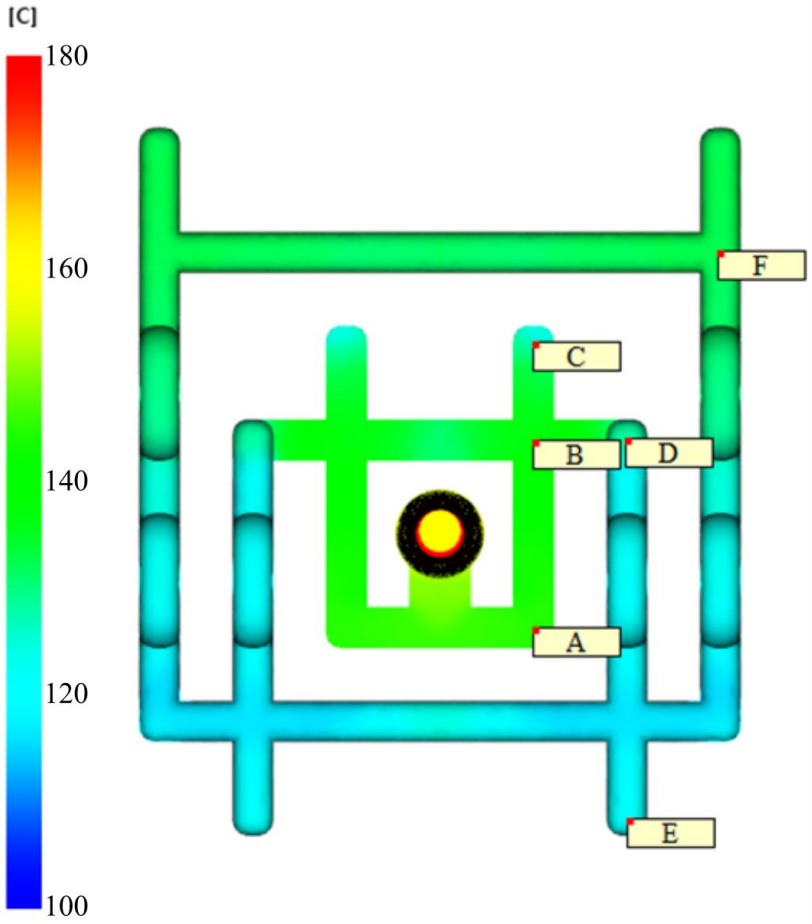

Fig. 48 - Positions of infrared sensors (A-F) determined from the simulation.

Sensor in position A is used to monitor the initial value of the melt temperature after temperature change due to the cold runner system. B sensor is located in the place, where the flow is split into three: first flow forms the first weld line, second reaches the dead branch, where C sensor is located, and third continues mold filling. D sensor depicts the temperature change due to the sharp corner, and the distance between B-C sensors and B-D sensors is kept the same. E sensor belongs to the second dead branch, and the melt reaches this area after passing through the first obstacle, where the cross-section undergoes continuous change. The last sensor F is located close to the end of the filling, and between D-F material passes through 3 obstacles with the continuous cross-section changes, and along the sharp edge with the sudden change in the cross-section profile.

From the simulation, the temperature development (Fig. 49) in these six areas was recorded.

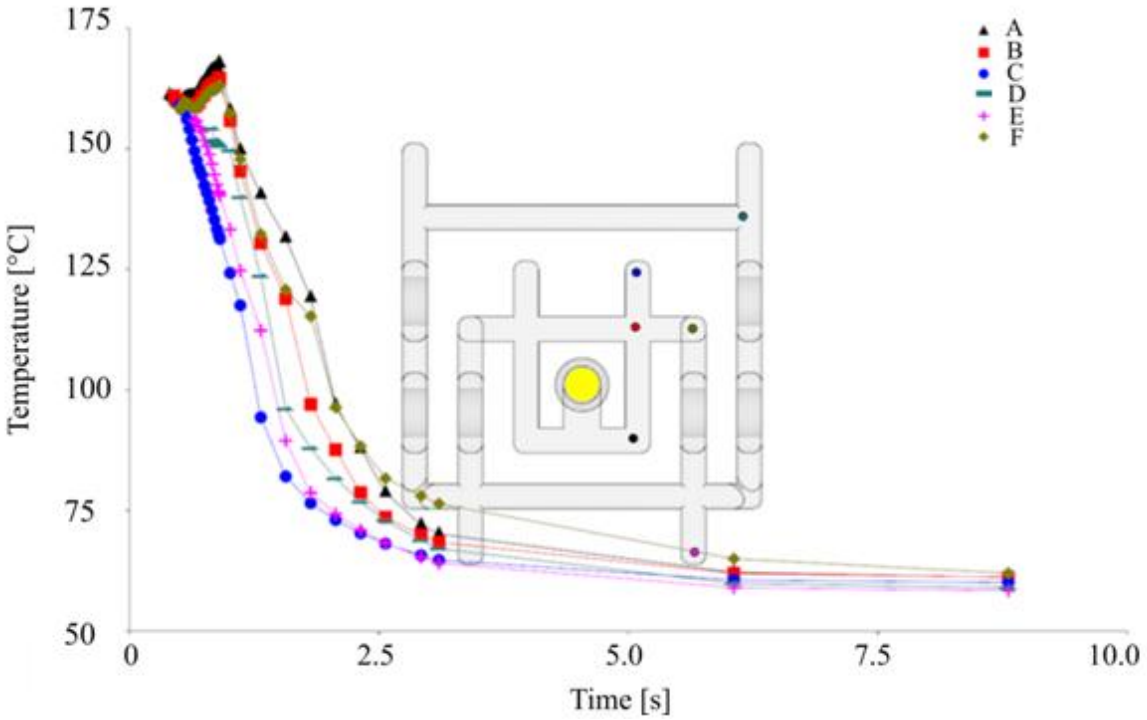

Fig. 49 – Simulation of temperature development at IR-sensor positions

After the construction of the testing mold, the real observations in preselected areas with IR sensors will be done, and results will be compared to verify the simulation results.

5.4 Results for Phase Separation Mold

Ejector-type IR sensor with diameter D = 4 mm (IT6) and length L = 160 mm (IT6) was clamped into ejector plate instead of cylindrical ejector with the same diameter. Clamped IR sensor in ejector plate was connected to pre-amplifier, which converts an optical signal to an analogue electrical signal, which passes through main amplifier, where 100 °C represents 1 V on output. Data from main amplifier is recorded with data logger in 100 ms sampling frequency and stored to PC. The scheme of the temperature monitoring is illustrated in Fig. 48. Orange color highlights the schematic view of the temperature monitoring experiment. To ensure moldability of testing geometry, test arrangement was extended for pneumatic system (represented with blue color) that ensures formation moving of core pins to formation of obstacles presented in Fig. 43.

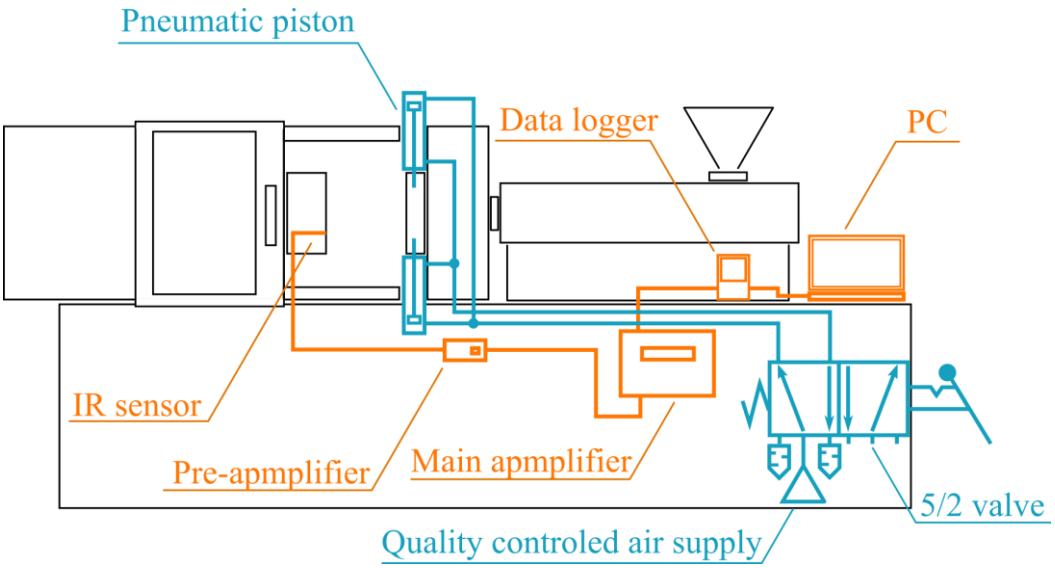

Fig. 50 – Test arrangement of temperature monitoring

Data obtained from IR sensors was aligned according to maximum temperature. Due to the fact that the obtained data are discrete values (Fig. 51), all measurements were repeated 12 times to minimize inaccurate peak values.

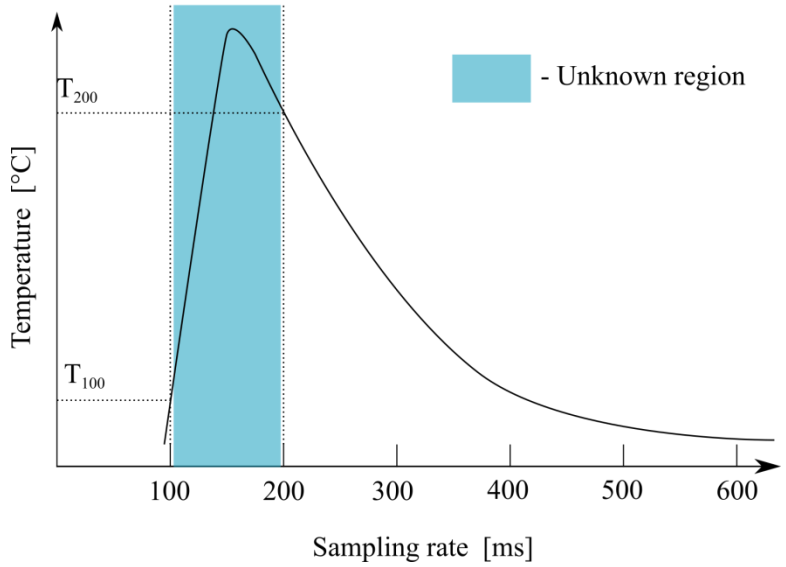

Fig. 51 - The weakest point of IR measurement

5.4.1 Temperature monitoring in separation mold

Table 13 summarizes the data obtained from temperature monitoring of PIM feedstock with IR sensor at the position A as the example.

Table 13 – Obtained data from IR sensor A for first position in testing mold

Number of measurement											**Basic Statistic**					
1.	**2.**	**3.**	**4.**	**5.**	**6.**	**7.**	**8.**	**9.**	**11.**	**12.**	$\bar{x}$	***s***	$\widehat{cv}$	**Min.**	**Max.**	$\tilde{x}$
156.4	155.6	148.2	160.8	165.4	153.2	166.1	174.0	160.5	162.9	153.1	159.7	7.32	4.58	148.2	174.0	160.5
162.2	162.7	151.2	157.9	156.7	153.6	154.2	155.1	149.3	157.6	164.0	156.8	4.75	3.03	149.3	164.0	156.7
157.3	156.8	149.7	155.3	154.7	152.0	152.6	152.8	149.1	155.2	158.1	154.0	2.98	1.94	149.1	158.1	154.7
150.1	153.6	147.6	152.9	149.3	147.8	147.9	148.5	145.1	149.8	151.6	149.5	2.50	1.67	145.1	153.6	149.3
144.4	144.5	140.7	144.4	144.0	142.4	142.6	143.5	140.7	144.2	145.6	143.4	1.59	1.11	140.7	145.6	144.0
136.5	136.3	132.9	136.4	136.1	134.7	134.9	137.7	133.6	135.8	137.4	135.7	1.50	1.10	132.9	137.7	136.1
130.5	130.3	128.3	130.5	130.7	129.1	129.5	128.1	128.1	130.2	131.9	129.7	1.23	0.95	128.1	131.9	130.2
126.0	125.7	123.6	125.7	125.4	124.8	124.7	124.0	122.6	125.7	126.5	125.0	1.17	0.94	122.6	126.5	125.4
120.3	120.0	117.9	120.0	119.8	119.3	118.8	118.2	117.1	120.3	120.7	119.3	1.16	0.97	117.1	120.7	119.8
115.8	115.4	113.6	115.4	115.3	116.0	114.8	114.0	113.0	115.8	117.3	115.1	1.22	1.06	113.0	117.3	115.4
112.3	112.6	110.4	112.4	112.1	111.2	111.6	110.5	110.4	111.8	112.2	111.6	0.84	0.75	110.4	112.6	111.8
107.9	108.5	106.1	108.8	108.0	107.2	107.4	106.3	106.2	107.5	107.9	107.4	0.92	0.85	106.1	108.8	107.5
105.4	105.4	104.0	105.8	105.4	104.8	104.6	102.6	103.2	105.8	106.1	104.8	1.13	1.08	102.6	106.1	105.4
103.3	102.8	100.5	102.7	102.8	102.2	102.4	99.3	99.8	102.1	103.0	101.9	1.38	1.35	99.3	103.3	102.4
99.9	100	98.4	99.8	101.3	99.6	98.8	97.7	97.5	100.1	99.3	99.3	1.13	1.13	97.5	101.3	99.6
97.5	97.6	94.8	97.5	97.3	97.3	96.7	95.5	95.7	97.3	96.4	96.7	0.96	1.00	94.8	97.6	97.3
95.6	95.2	92.4	95.0	94.6	94.7	94.2	93.7	93.0	94.3	94.5	94.3	0.95	1.00	92.4	95.6	94.5
92.9	92.9	87.9	92.9	92.3	91.9	92.2	89.4	90.5	91.3	93.0	91.6	1.67	1.82	87.9	93.0	92.2
90.2	90.6	84.9	90.7	90.7	89.5	89.7	88.0	87.0	89.7	91.0	89.3	1.90	2.13	84.9	91.0	89.7
88.0	89.5	83.7	89.7	88.5	88.1	88.6	85.8	85.9	87.4	88.4	87.6	1.80	2.05	83.7	89.7	88.1

Data from all sensors was investigated with a cluster analysis to find similarities between positions; the results are shown in Fig. 52.

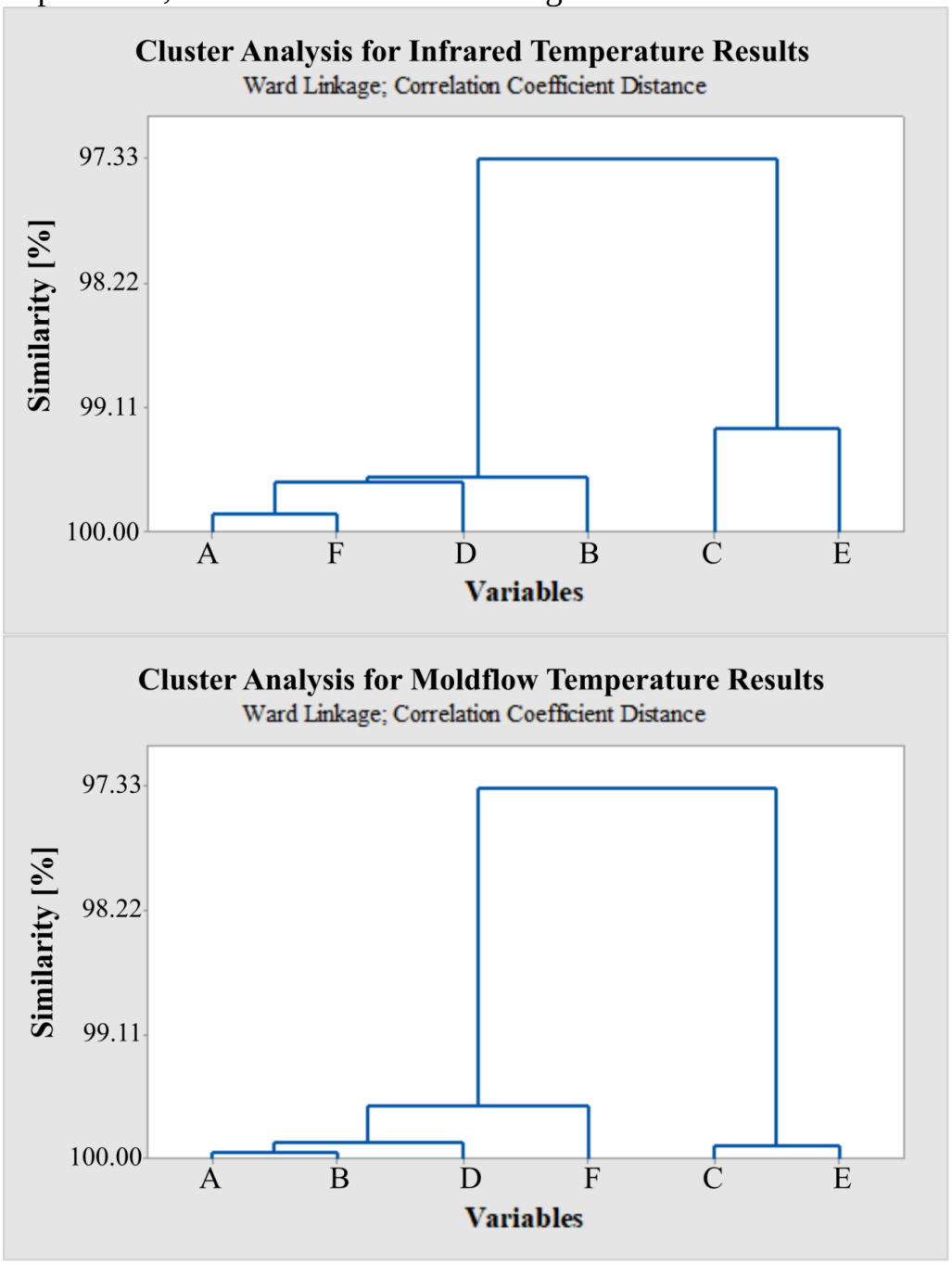

Fig. 52 – Cluster analysis of data from IR sensors (upper) and Moldflow simulation (lower) with Ward linkage method

From the cluster analysis (Fig. 52) it is evident that the temperature development for positions C and E differ in comparison to A, B, D, F positions due to their location in dead branches. While on the sensors A, B, D, F sample core of test specimen is used as a transport channel to fulfill the mold, positions of C and E sensors are in the areas, where the solidification takes place (material is not moving).

To find the best regression model, three types of regression function were used: linear, quadratic and cubic; the models with plots of residual value to fitted value are shown on Figs. 53, 54, and 55, respectively.

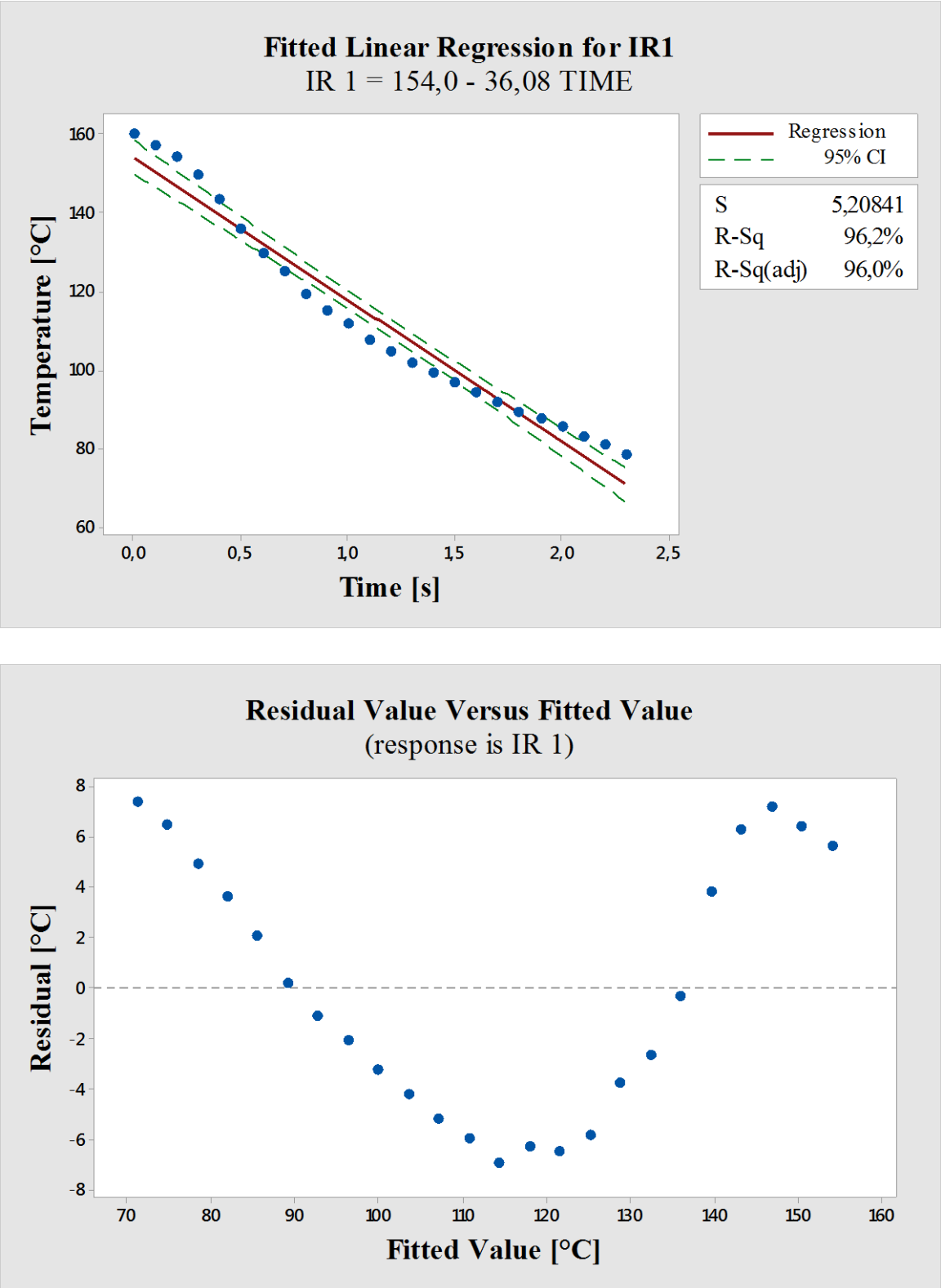

Fig. 53 - Linear regression function and plot of residual value to fitted value for regression function of IR sensor A.

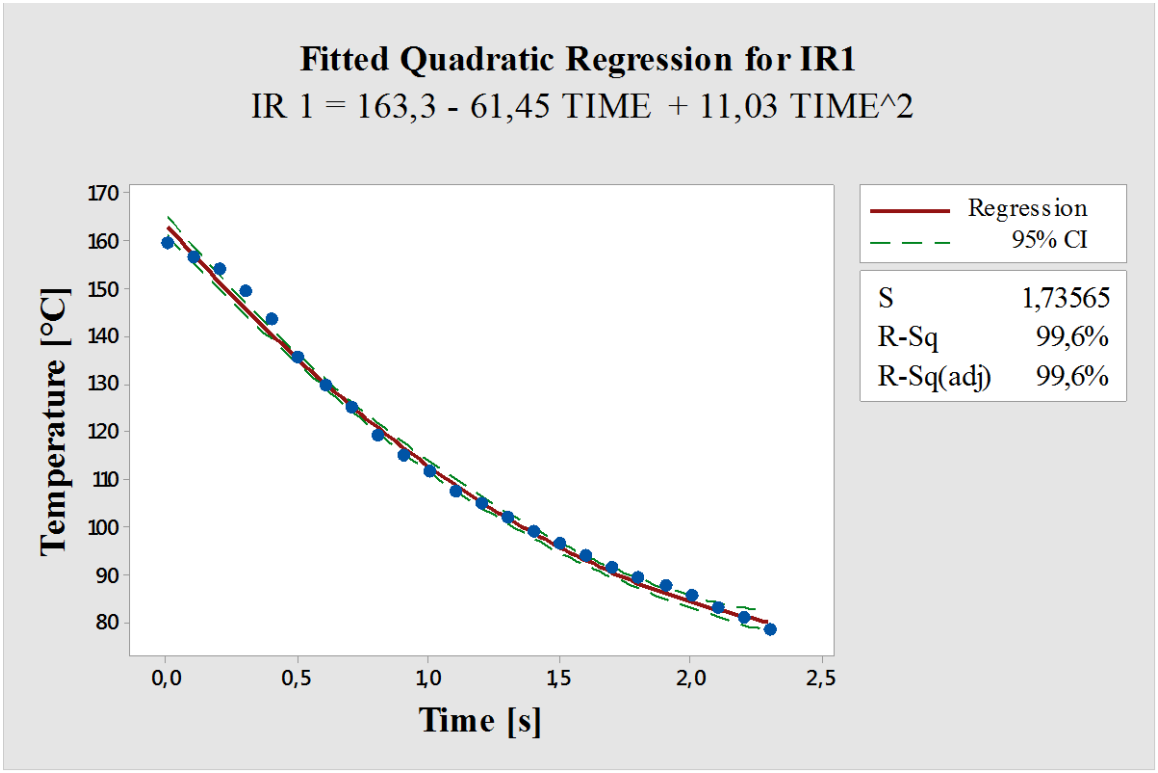

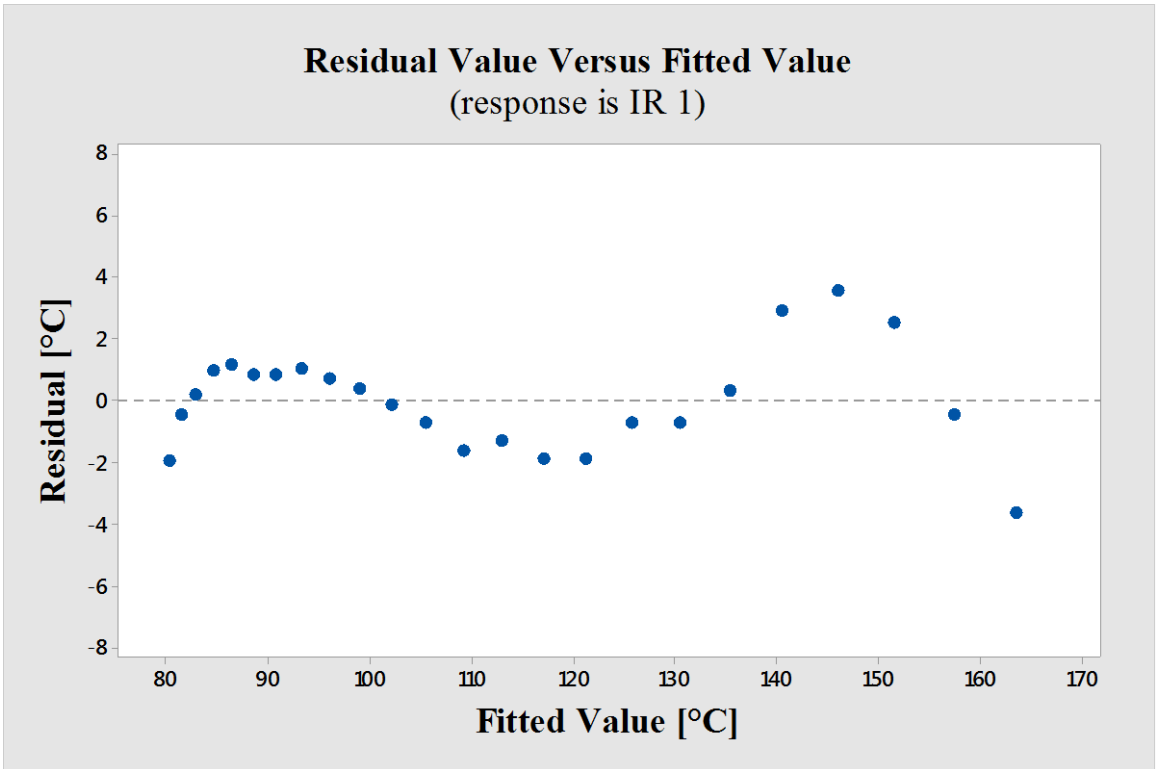

Fig. 54 - Quadratic regression function and plot of residual value to fitted value for regression function of IR sensor A

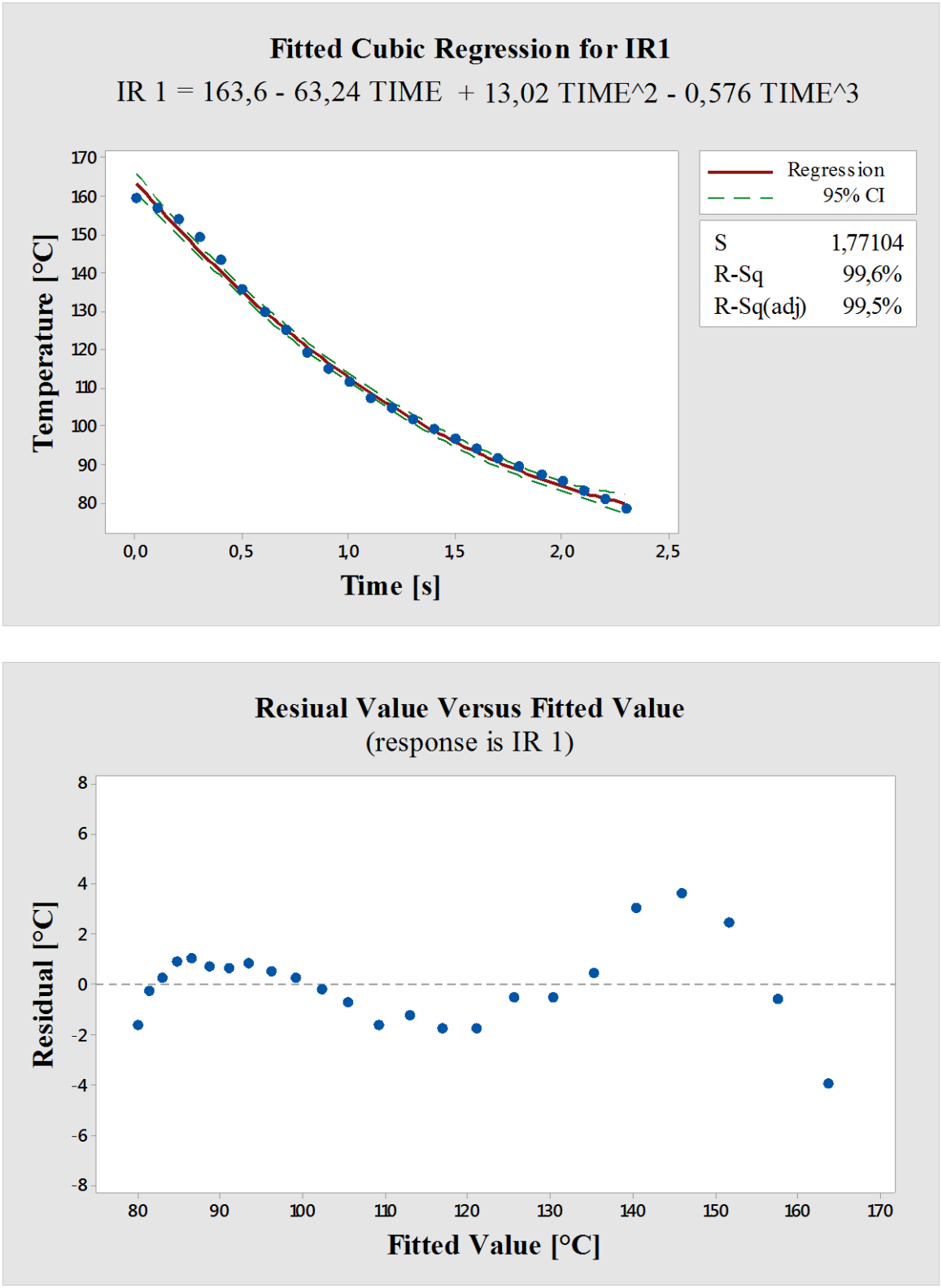

Fig. 55 - Cubic regression function and plot of residual value to fitted value for regression function of IR sensor A.

Subsequently, results of residual values are summarized in Table 14 for all regression functions for A position of IR sensor.

Table 14 - Residual value for fitted regression function for all three regressions

	Type of Regression Function					
	Linear		Quadratic		Cubic	
IR A	Fit	Residual	Fit	Residual	Fit	Residual
159.7	154.02	5.66	163.33	-3.64	163.63	-3.95
156.8	150.41	6.42	157.29	-0.46	157.44	-0.60
154.0	146.81	7.18	151.48	2.51	151.50	2.48
149.5	143.20	6.25	145.88	3.57	145.82	3.63
143.4	139.59	3.83	140.51	2.91	140.38	3.04
135.7	135.98	-0.33	135.36	0.29	135.19	0.46
129.7	132.37	-2.66	130.43	-0.71	130.25	-0.53
125.0	128.77	-3.77	125.71	-0.71	125.54	-0.54
119.3	125.16	-5.83	121.22	-1.89	121.08	-1.74
115.1	121.55	-6.48	116.95	-1.89	116.84	-1.77
111.6	117.94	-6.31	112.91	-1.27	112.83	-1.20
107.4	114.33	-6.90	109.08	-1.64	109.05	-1.62
104.8	110.73	-5.94	105.47	-0.69	105.49	-0.71
101.9	107.12	-5.19	102.08	-0.15	102.15	-0.22
99.3	103.51	-4.21	98.91	0.39	99.03	0.27
96.7	99.90	-3.24	95.97	0.70	96.12	0.55
94.3	96.29	-2.04	93.24	1.01	93.41	0.84
91.6	92.69	-1.12	90.74	0.83	90.91	0.65
89.3	89.08	0.22	88.45	0.85	88.62	0.68
87.6	85.47	2.10	86.39	1.18	86.52	1.05
85.5	81.86	3.64	84.55	0.95	84.61	0.89
83.2	78.25	4.90	82.92	0.23	82.90	0.25
81.1	74.65	6.45	81.52	-0.42	81.38	-0.28
78.4	71.04	7.38	80.34	-1.92	80.03	-1.62

From the results it is clear that the linear regression function is not suitable for the determination of the melt cooling inside injection mold. Maximum residual value is almost 8 °C, and residual values to fitted values deviate in a bell-shape pattern. Therefore, one parameter was added to the model in order to obtain the quadratic regression functions. Then, the residual values decreased to no more than 3.7 °C, but the bell-shape profile is still visible. When the cubic regression was employed, the maximum residue even increased to

almost 4 °C. The same procedure of a regression function was applied to the remaining 5 IR sensors, and the results are summarized in Table 15.

Table 15 - Comparison of regression functions for all six IR sensors

			Standard Error	Adjusted R^2
Type of Regression Function	Linear	IR A	5.208	95.99 %
		IR B	8.041	90.71 %
		IR C	7.118	88.23 %
		IR D	4.856	95.67 %
		IR E	8.294	82.16 %
		IR F	5.373	95.31 %
	Quadratic	IR A	1.736	99.55 %
		IR B	3.241	98.49 %
		IR C	1.423	99.53 %
		IR D	3.194	98.13 %
		IR E	3.401	97.00 %
		IR F	1.626	99.57 %
	Cubic	IR A	1.771	99.54 %
		IR B	3.269	98.48 %
		IR C	1.366	99.57 %
		IRD	3.205	98.11 %
		IR E	1.243	99.60 %
		IR F	1.596	99.59 %

Table 16 - Overal results for regression functions for all IR sensors

	Linear regression	Quadratic regression	Cubic regression
IR A	95.99 %	99.55 %	99.54 %
IR B	90.71 %	98.49 %	98.48 %
IR C	88.23 %	99.53 %	99.57 %
IR D	95.67 %	98.13 %	98.11 %
IR E	82.16 %	97.00 %	99.60 %
IR F	95.31 %	99.57 %	99.59 %

Adjusted regression coefficient R^2 representing the proximity of the data to the fitted regression curve was divided into three sections, Table 16. Results of R^2 between (98-100) % was considered as a good fit (green color), (98-96) % represents sufficient fitting (orange color) and the R^2 value bellow 96 % is considered as insufficient model fit (red color). The linear regression model is not suitable for determination of temperature development. Quadratic and cubic

model are eligible. Since the model should be simple, less parameter - quadratic model was used further.
The same philosophy was applied on data from Moldflow (MF) analysis (Table 17.)

Table 17 - Comparison of regression functions for all six MF sensors

			Standard Error	Adjusted R^2
Type of Regression Function	Linear	MF A	5.182	97.57 %
		MF B	6.247	96.57 %
		MF C	10.916	87.03 %
		MF D	6.674	95.32 %
		MF E	12.846	81.12 %
		MF F	9.010	91.75 %
	Quadratic	MF A	4.652	98.04 %
		MF B	4.650	98.10 %
		MF C	2.476	99.33 %
		MF D	5.027	97.34 %
		MF E	2.747	99.14 %
		MF F	5.414	97.02 %
	Cubic	MF A	1.495	99.80 %
		MF B	2.112	99.61 %
		MF C	2.528	99.30 %
		MF D	3.559	98.67 %
		MF E	2.546	99.26 %
		MF F	4.068	98.32 %

Table 18 - Overal results for regression functions for all MF sensors

	Linear regression	Quadratic regression	Cubic regression
IR A	97.57 %	98.04 %	99.80 %
IR B	96.57 %	98.10 %	99.61 %
IR C	87.03 %	99.33 %	99.30 %
IR D	95.32 %	97.34 %	98.67 %
IR E	97.57 %	98.04 %	99.80 %
IR F	96.57 %	98.10 %	99.61 %

The same methodic for evaluation of regression functions of Moldflow results as for IR sensors is adopted. From Table 18 is noticeable that linear regression is not suitable for our purpose and quadratic regression is sufficiently precise with small number of parameters.

5.4.2 Experimental Qualification of Separation

Fifth corner of test specimen for phase separation has been inspected in detail. The reason for this location is that it contains sharp edges, rapid variations in a cross section and flow direction, and according to simulations, this feature supports phase separation (Section 5.3).

Furthermore, a higher melt temperature was measured at sensor location F, than in case of previous sensor location (E). Therefore, the potential of the separation due to increased dissipation heat (initialized by shear rate) is evident.

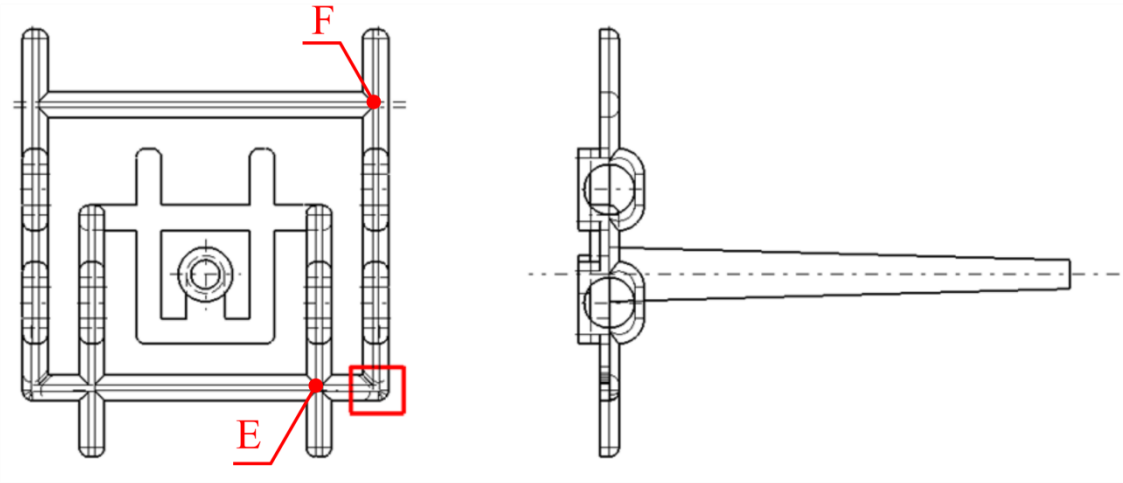

Fig. 57 - Position of fifth corner selected for detailed inspection

From SEM, the powder/binder separation is evident on the surface (Fig. 58) what brings the question if the same trend is inside the testing specimen. Therefore, a computed tomography (CT) was employed, Fig. 59.

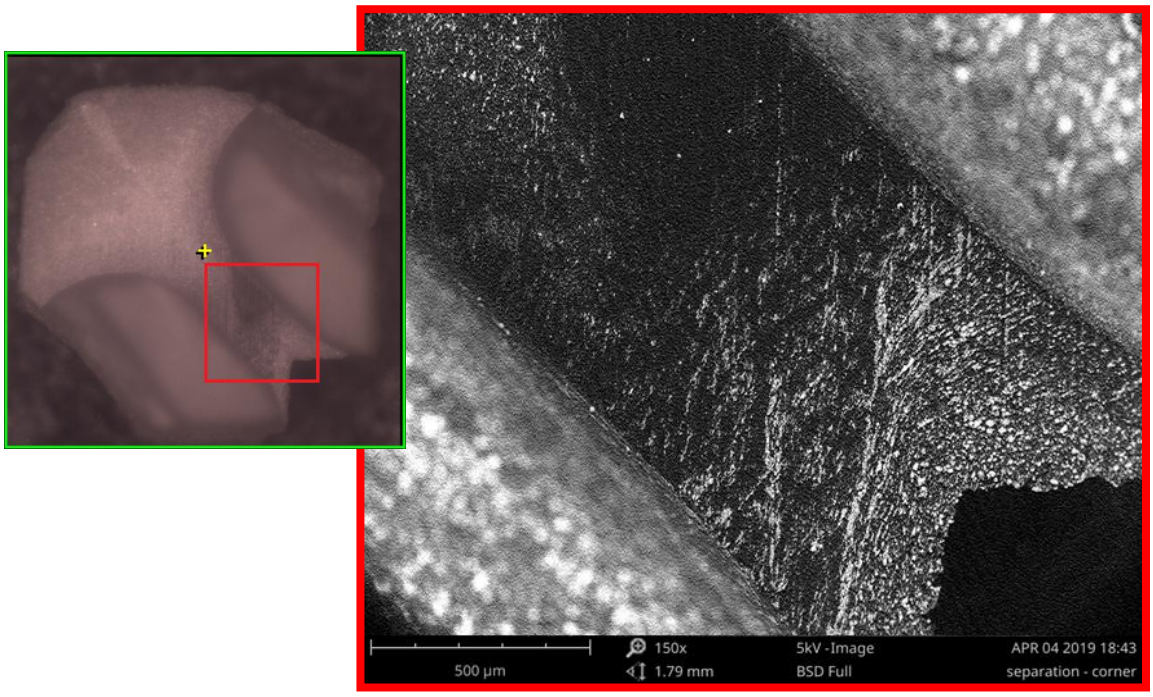

Fig. 58 - SEM selected mold element for phase separation of 17-4 PH feedstock

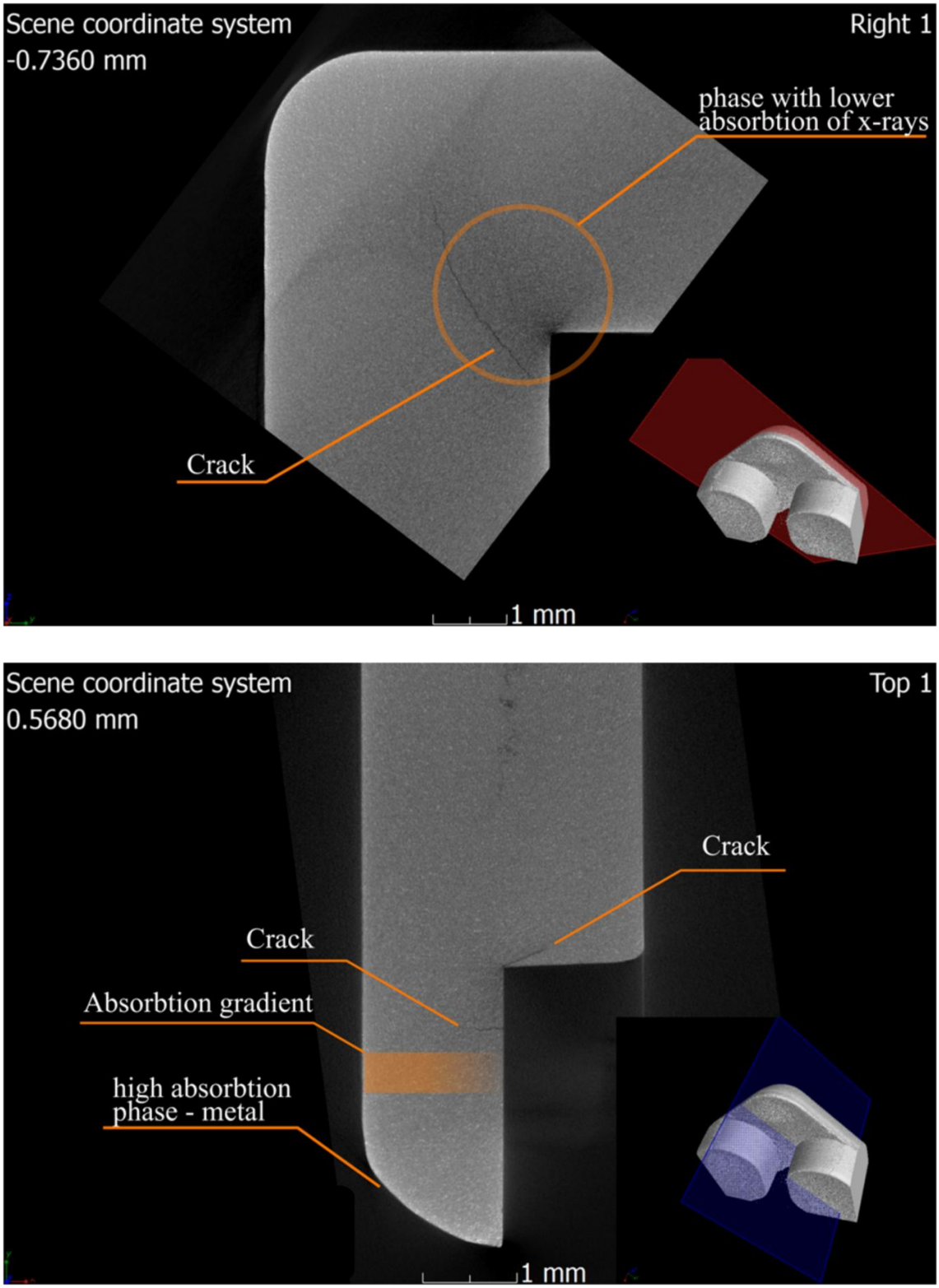

Fig. 59 - CT imaging of test sample

From the results of CT imaging, where X-ray absorption differs in thickness, it is evident that phase separation is not problem only on the surface, but it occurs in a bulk. Small absorption is at the corner, where exceed of binder is predicted due to shear rate gradient. Also, cracks, as accompanying effect of separation, are evident in Fig.59.

5.5 Mold Concept of Insert Mold

Specimens for tensile tests were molded at two modifications: without weld line, when only one gate has been used, and with weld line, when filling has been supported with a second gate.

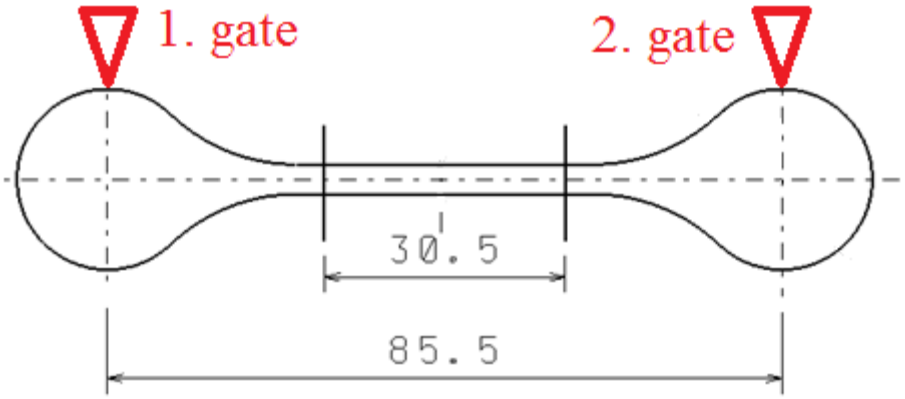

Fig. 60 - Gating possibilities in insert mold for tensile strength testing

Copper, aluminum alloy, and bronze inserts were machined by milling and drilling. Machining was performed in the laboratories of the Department of Production Engineering TBU. The tool paths were generated with NX CAM post-processor and outer dimensions of insert were tailored to IT5 tolerance.
Second group of inserts is based on polymers. 3D printed mold insert produced on Polyjet 3D printer with layer thickness of 25 microns was made of acrylic monomer with photoinitiator with post thermal treatment to increase HDT temperature up to 95 °C, when the specimen is loaded with 0.45 MPa. Another mold insert was produced by casting of epoxy resin compound (Fig. 61). First of all, the positive model was designed, and therefore 3D printed on Formlabs Form 2 3D printer from mixture of methacrylated oligomers, monomers and photoinitiator with 50μm layer thickness. After printing, the non-cured resin was washed in 99,5 % isopropyl alcohol for 10 minutes, and finally post-cured in 465 nm UV light for 2 hours. To this model, a silicon rubber was casted to obtain the negative copy. As a silicon material, Lukopren N1522 with 2 wt.% of activator of vulcanization due to high tear resistivity was chosen. Subsequently, pure epoxy resin and epoxy resin with thermal conductive filler were casted into the silicon mould. As a casting material for mold insert, high temperature resistant epoxy resin Gamod Fluid T206 with thermal conductive hexagonal boron nitride (hBN) has been used. According to low density of hBN, 15 wt. % (approx. 35 vol.%) of a filler has been used in the compound.

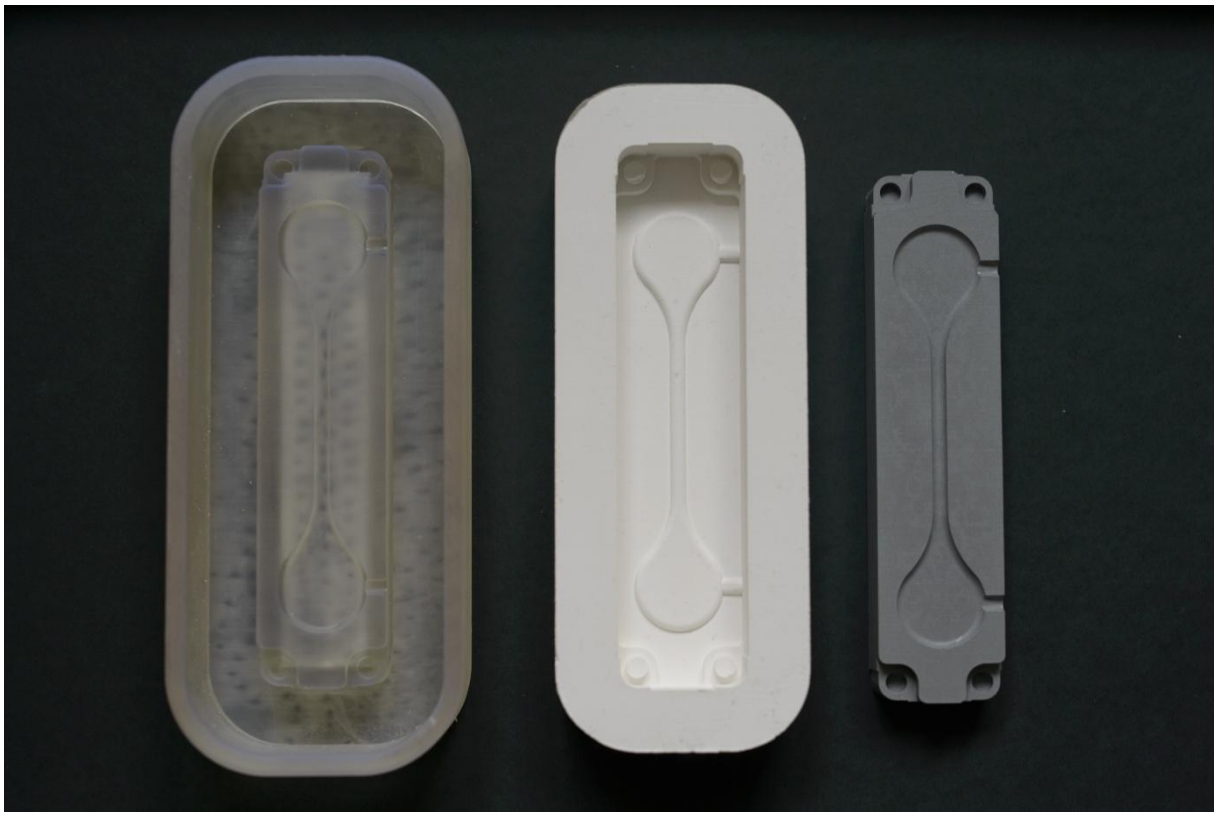

Fig. 61 - 3D printed model (left), negative silicon mold (middle), final insert from epoxy resin (right)

This modification of resin with hBN increased the thermal conductivity for 148 %. Overall mechanical and thermal properties of all mold inserts are summarized in Table 19.

Table 19 - Overall mechanical and thermal properties of inserts

Material of mold inserts		***R*m**			***λ***		
		[MPa]			[$W.m^{-1}.k^{-1}$]		
		$\bar{x}$	s	u	$\bar{x}$	s	u
Aluminium		453.5	22.6	5.0	383.90	14.86	3.87
Copper		167.3	12.7	7.6	154.03	2.16	1.40
Bronze		301.1	8.4	2.8	64.15	1.50	2.34
3D printed		54.2	3.7	6.8	0.992	0.015	1.54
epoxy resin	**+ 0 vol.% hBN**	47.3	12.8	27.1	0.389	0.007	1.70
	+ 35 vol.% hBN	21.4	4.1	19.2	0.204	0.008	3.66

Both PolyMIM 17-4PH and WPC compounds were utilized to test the influence of weld line on tensile strength.

5.6 Tensile strenght of molded highly filled compounds related to weld lines

Tensile test specimens molded in all inserts. In case of PIM compound (17-4PH feedstock), debinding and sintering was carried out prior mechanical testing. The results are summarized in Tables 20-23.

Table 20 - 17-4PH tensile strength for inserts without weld line

No.	Tensile Strength [MPa]					
	Copper	Aluminium	Bronze	ER + hBN	ER	3D printer
1	1080	1180	1180	1200	1170	1280
2	1110	1220	1230	1260	1160	1280
3	1080	1220	1190	1240	1240	1270
4	1090	1210	1270	1270	1210	1260
5	1100	1200	1130	1100	1190	1190
6	1080	1180	1170	1190	1230	1240
7	1090	1200	1180	1240	1230	1230
8	1130	1160	1250	1150	1230	1220
9	1040	1240	1230	1260	1210	1280
10	1080	1210	1240	1240	1190	1240
$\bar{x}$	1088	1202	1207	1215	1206	1249
$\tilde{x}$	1085	1205	1210	1240	1210	1250
S	23.48	23.48	43.47	55.03	27.57	30.35
Y	2.16	1.95	3.60	4.53	2.29	2.43

Table 21 - 17-4PH Tensile Strength for inserts with weld line

No.	Tensile Strength [MPa]					
	Copper	Aluminium	Bronze	ER + hBN	ER	3D printer
1	1180	1150	1140	1260	1260	1310
2	1240	1220	1280	1240	1180	1260
3	1170	1230	1190	1160	1170	1270
4	1210	1170	1170	1260	1140	1260
5	1230	1230	1230	1190	1230	1190
6	1240	1210	1190	1240	1220	1220
7	1150	1170	1250	1170	1170	1290
8	1150	1170	1230	1180	1230	1180
9	1190	1200	1190	1220	1240	1240
10	1200	1230	1250	1270	1260	1200
$\bar{x}$	1196	1198	1212	1219	1210	1242
$\tilde{x}$	1195	1205	1210	1230	1225	1250
s	34.06	30.48	42.90	40.95	41.90	43.67
υ	2.85	2.54	3.54	3.36	3.46	3.52

Table 22 - WPC Tensile Strength for inserts without weld line

No.	Tensile Strength [MPa]					
	Copper	**Aluminium**	**Bronze**	**ER + hBN**	**ER**	**3D printer**
1	22.2	26.4	24.5	26.3	28.5	28.2
2	22.7	26.4	21.2	28.7	27.3	30.0
3	23.0	24.3	23.9	25.8	26.9	28.7
4	20.1	27.8	21.0	27.4	29.3	28.5
5	20.8	24.9	22.1	27.3	27.6	27.8
6	21.6	27.0	24.9	27.8	27.9	29.3
7	22.4	28.3	23.8	26.8	26.8	30.4
8	21.6	22.3	23.0	25.2	26.9	30.1
9	20.8	26.2	23.2	28.2	27.5	27.0
10	21.2	26.7	25.3	28.5	26.3	28.9
$\bar{x}$	21.64	26.03	23.29	27.2	27.50	28.89
$\tilde{x}$	21.60	26.40	23.50	27.35	27.40	28.80
S	0.93	1.77	1.49	1.17	0.89	1.08
Y	4.31	6.80	6.38	4.29	3.23	3.75

Table 23 - WPC Tensile Strength for inserts with weld line

No.	Tensile Strength [MPa]					
	Copper	**Aluminium**	**Bronze**	**ER + hBN**	**ER**	**3D printer**
1	5.79	7.14	8.39	7.65	7.05	7.25
2	5.22	6.57	7.10	8.72	8.76	9.37
3	7.87	5.20	7.04	9.11	7.45	8.50
4	6.86	6.55	6.58	8.64	7.96	7.68
5	7.01	6.32	9.40	8.22	6.85	8.72
6	5.77	6.70	6.94	7.06	8.12	7.39
7	4.34	5.86	6.77	6.87	7.68	9.35
8	7.05	5.34	7.47	8.11	6.96	9.85
9	4.29	4.92	8.21	9.05	7.25	9.23
10	5.76	6.87	7.49	8.51	6.92	9.02
$\bar{x}$	5.99	6.14	7.53	8.19	7.50	8.63
$\tilde{x}$	5.78	6.43	7.28	8.36	7.35	8.87
s	1.19	0.77	0.88	0.78	0.63	0.91
υ	19.89	12.51	11.66	9.53	8.36	10.53

5.6.1 Outlier Test

Obtained data was inspected to the outlier value. Bellow, the analysis for the copper insert and PIM feedstock is presented as the example (Table 24, Fig. 62).

Table 24 - 17-4PH Tensile strength for inspected cooper insert

No.	Tensile Strength [MPa]					
	Copper	Aluminium	Bronze	ER	ER + hBN	3D printer
1	1090	1180	1180	1170	1200	1280
2	1110	1220	1230	1160	1260	1280
3	1080	1220	1190	1240	1240	1270
4	1090	1210	1270	1210	1270	1260
5	1100	1200	1130	1190	1100	1190
6	1080	1180	1170	1230	1190	1240
7	1090	1200	1180	1230	1240	1230
8	1130	1160	1250	1230	1150	1220
9	1040	1240	1230	1210	1260	1280
10	1080	1210	1240	1190	1240	1240
$\bar{x}$	1088	1202	1207	1206	1215	1249
$\tilde{x}$	1085	1205	1210	1210	1240	1250
s	23.48	23.48	43.47	27.57	55.03	30.35
υ	2.16	1.95	3.60	2.29	4.53	2.43

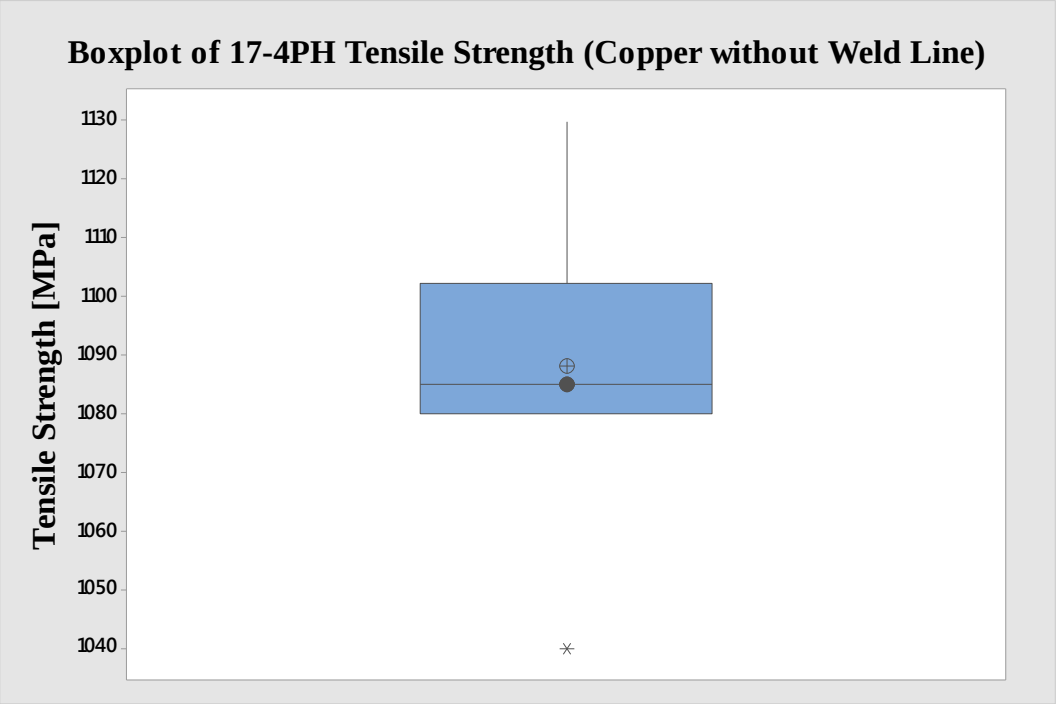

Fig. 62 - Boxplot of 17-4PH tensile strength for copper insert

The value of tensile strength 1040 MPa (Number of observation 9) seems as an outlier value and can strongly affect obtained data. Therefore, the attention on outlier is paid, and this value will be further inspected with Grubbs test.

According to previous findings in Box Plot diagram, the hypothesis for Grubbs test are formulated as:

H_0: There are no outliers
H_a: The smallest data value is an outlier
at significance level α = 5%

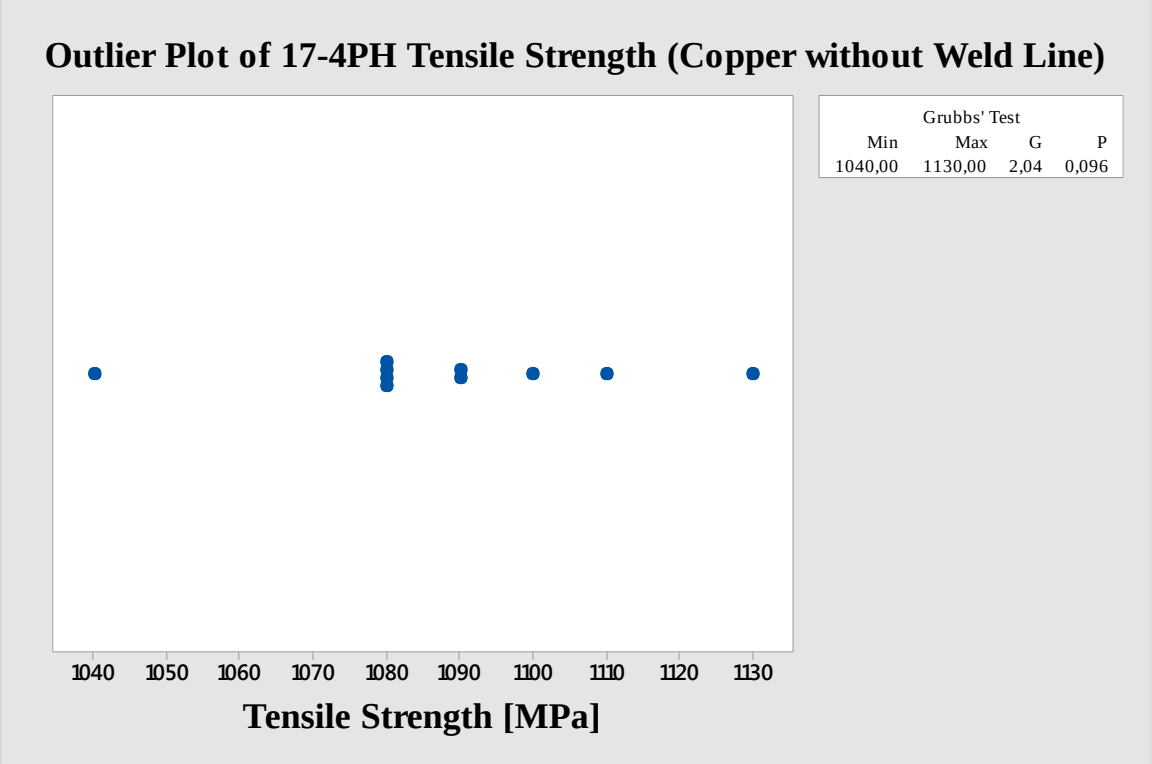

Fig. 63 – Outlier plot of 17-4PH tensile strength for Copper insert without weld line

$$G = \frac{\bar{x} - x_{\min}}{s} = \frac{1088 - 1040}{23.5} = 2.0425$$

From the Grubbs test can be claimed that the smallest data value 1040 MPa is 2.04 standard deviations less than mean of a sample data. The *p*-value (0.096) indicates that if the obtained data are from the same normally distributed population, the possibility of obtaining such small value is 9.6 %.
After performing a 1-sample *t*-test on 10 observations, the inverse cumulative probability of which equals the critical value of 1.8331. According to the absolute value of Grubbs test G = 2.0425, which is higher than the *t*-statistic value (1.8331), it is possible to fail to reject the null hypothesis and conclude that the smallest value is not an outlier.

5.6.2 Overall statistics of Outlier Test

This statistic has been done for all sample data of the population, Table 25.

Table 25 – Outlier tests statistics for 17-4PH feedstock

		Insert	Outlier Test			
			Outlier	G-value	P-value	Valid
17-4PH	without Weld Line	Copper	min	2.04	0.096	H_0
		Aluminium	min/max	1.79	0.516	H_0
		Bronze	min	1.77	0.273	H_0
		ER + hBN	min/max	1.67	0.749	H_0
		ER	min	2.09	0.078	H_0
		3D	min	1.97	0.147	H_0
	with Weld Line	Copper	min	1.35	0.829	H_0
		Aluminium	min	1.57	0.485	H_0
		Bronze	min/max	1.67	0.727	H_0
		ER + hBN	min/max	1.67	0.372	H_0
		ER	min/max	1.44	1.000	H_0
		3D	max	1.56	0.508	H_0
WPC	without Weld Line	Copper	min	1.65	0.395	H_0
		Aluminium	min	2.11	0.071	H_0
		Bronze	max	1.35	0.824	H_0
		ER + hBN	max	2.3	0.104	H_0
		ER	min	1.71	0.329	H_0
		3D	min	1.74	0.298	H_0
	with Weld Line	Copper	max	1.57	0.49	H_0
		Aluminium	min/max	1.6	0.918	H_0
		Bronze	max	2.12	0.068	H_0
		ER + hBN	max	2.1	0.112	H_0
		ER	min	1.70	0.346	H_0
		3D	min	1.52	0.552	H_0

It is possible to fail to reject the null hypothesis (p-value > αalpha), and conclude that not enough evidence is available to suggest the null as false at the 95 % confidence level.

5.6.3 Normality Test

Test of normal distribution was performed with Anderson-Darling method . In Table 26 copper insert is analyzed as an example. Anderson-Darling is:

$$AD = -n - \frac{1}{n}\sum_{i=1}^{n}(2i-1)\left[\ln F(X_i) + \ln(1 - F(X_{n-i+1}))\right]$$

Table 26 - Data for Anderson-Darling test

Data	Sorted	Count	$F(Y_i)$	$1\text{-}F(Y_{N+1-i})$	Si
1080	1040	1	0.0204	0.0368	-7.1922
1110	1080	2	0.3666	0.1743	-8.2503
1080	1080	3	0.3666	0.3046	-10.9604
1090	1080	4	0.3666	0.4660	-12.3679
1100	1080	5	0.3666	0.4660	-15.9016
1080	1090	6	0.5339	0.6333	-11.9259
1090	1090	7	0.5339	0.6333	-14.0942
1130	1100	8	0.6953	0.6333	-12.3000
1040	1110	9	0.8256	0.6333	-11.0209
1080	1130	10	0.9631	0.9795	-1.1048

$F(Y_i)$ and $1\text{-}F(Y_{N+1-i})$ are values calculated from the standard normal cumulative distribution function, which arises when mean is 0, the standard deviation is 1, and *Si* is auxiliary function which formula is:

$$S_i = \sum_{i=1}^{n}(2i-1)\left[\ln F(X_i) + \ln(1 - F(X_{n-i+1}))\right]$$

Anderson-Darling statistic is therefore simplified to:

$$AD = -n - \frac{1}{n}\sum_{i=1}^{n} S_i$$

$$AD = -10 - \frac{-105.1184}{10}$$

$$AD_{adj} = 0.5118$$

According to small sample size Anderson-Darling statistic is adjusted to:

$$AD_{adj} = AD\left(1 + \frac{0.75}{n} + \frac{2.25}{n^2}\right)$$

$$AD_{adj} = 0.5118\left(1 + \frac{0.75}{10} + \frac{2.25}{10^2}\right)$$

$$AD_{adj} = 0.5617$$

Table 27 - Selection of correct formula (highlighted in green) for adjusted *AD* value

Anderson-Darling Statistic	Formula for p-value Calculation
$AD_{adj} \geq 0.60$	$\exp(1.2937-5.703(AD_{adj})+0.0186(AD_{adj})^2)$
$0.34 < AD_{adj} < 0.60$	$\exp(0.9177-4.279(AD_{adj})-1.38(AD_{adj})^2)$
$0.20 < AD_{adj} < 0.34$	$1-\exp(-8.318+42.796(AD_{adj})-59.938(AD_{adj})^2)$
$AD_{adj} \leq 0.20$	$1-\exp(-13.436+101.14(AD_{adj})-223.73(AD_{adj})^2)$

Therefore, *p-value* for small sample size is calculated as:

$$p-value = \exp(0.9177 - 4.279(\mathrm{AD}_{\mathrm{adj}}) - 1.38(\mathrm{AD}_{\mathrm{adj}})^2) = 0.1463$$

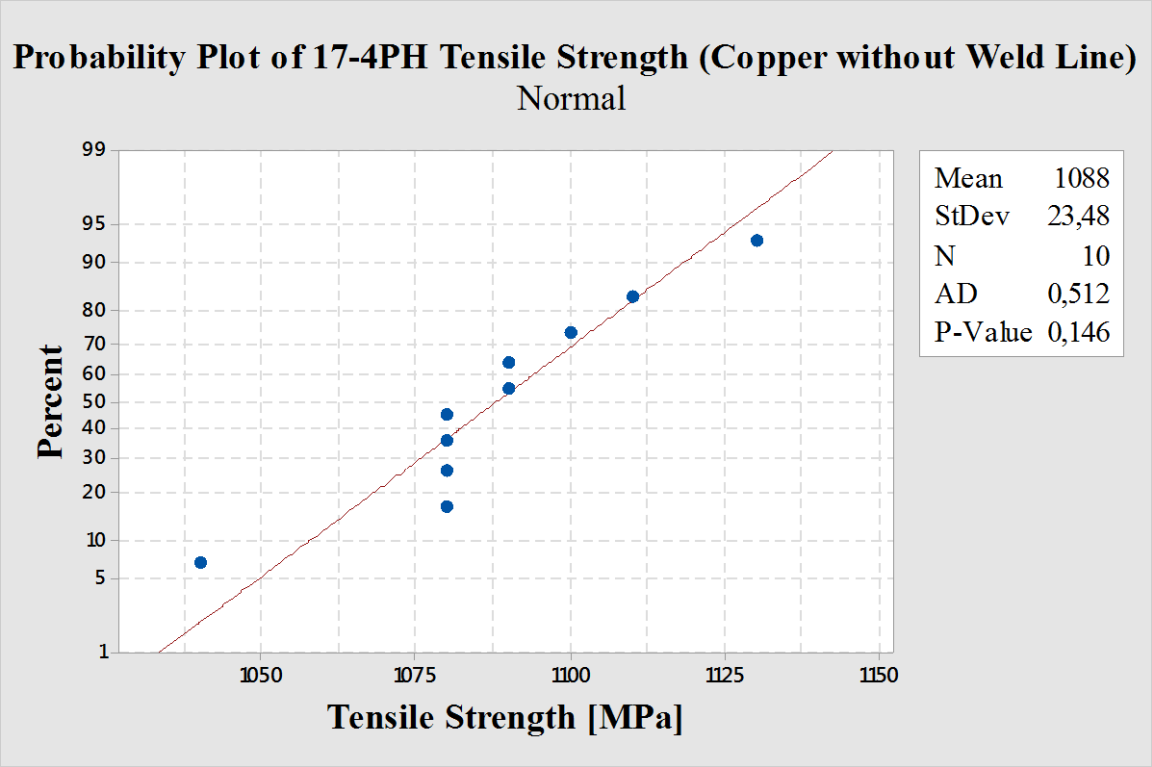

Fig. 64 - Probability plot of 17-4PH according to AD statistic

5.6.4 Overall statistics of normality test

The same principles of analysis was adopted for the remaining inserts and both PIM and WPC filled compounds, and the results of Anderson-Darling statistics is collected in Table 28.

Table 28 - Results for 17-4PH normality test

		Insert	P-value	Valid
17-4PH	without Weld Line	Copper	0.146	H_0
		Aluminium	0.681	H_0
		Bronze	0.512	H_0
		ER + hBN	0.304	H_0
		ER	0.091	H_0
		3D	0.326	H_0
	with Weld Line	Copper	0.625	H_0
		Aluminium	0.094	H_0
		Bronze	0.547	H_0
		ER + hBN	0.265	H_0
		ER	0.270	H_0
		3D	0.805	H_0
WPC	without Weld Line	Copper	0.869	H_0
		Aluminium	0.328	H_0
		Bronze	0.738	H_0
		ER + hBN	0.522	H_0
		ER	0.873	H_0
		3D	0.902	H_0
	with Weld Line	Copper	0.487	H_0
		Aluminium	0.301	H_0
		Bronze	0.187	H_0
		ER + hBN	0.339	H_0
		ER	0.423	H_0
		3D	0.270	H_0

For all cases, the *p*-value is larger than the significance level $\alpha = 5\%$, the decision is to fail to reject the null hypothesis, and therefore, with the probability of 1-α the obtained data originates in normal distribution. If significance level was set to $\alpha = 10\%$ values in orange color will reject the null hypothesis and accept alternative.

5.6.5 Test for Equal Variances

To do one-way ANOVA test, variances of the population have to be equal. Levene test was performed for tensile strength from copper insert with/without weld line as an example. Input data are in Table 29.

Table 29 - Data for Levene test for 17-4PH feedstock and copper insert with/without weld line

Var.	Tensile Strength [MPa]	
	Copper	Copper Weld Line
1	1080	1180
2	1110	1240
3	1080	1170
4	1090	1210
5	1100	1230
6	1080	1240
7	1090	1150
8	1130	1150
9	1040	1190
10	1080	1200
$\tilde{x}$	1085	1195

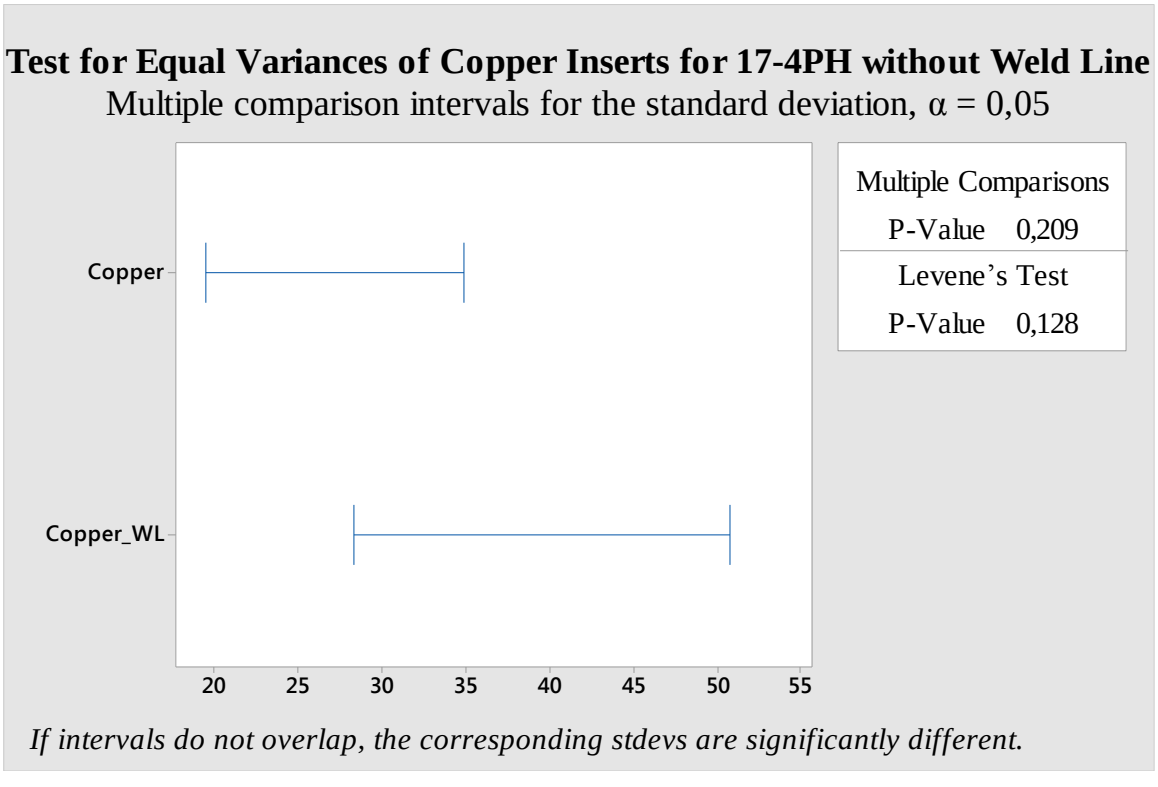

Fig. 65 – Statistic for Levene test for equal variances of copper inserts for17-4PH without weld line

$$W = \frac{(N-k)}{(k-1)} \frac{\sum_{i=1}^{k} N_i (\overline{Z_{i.}} - \overline{Z}_{..})^2}{\sum_{i=1}^{k} \sum_{j=1}^{N_i} (Z_{ij} - \overline{Z}_{i.})^2} = \frac{(10-2)}{(2-1)} \frac{\sum_{i=1}^{k} N_i (\overline{Z_{i.}} - \overline{Z}_{..})^2}{\sum_{i=1}^{k} \sum_{j=1}^{N_i} (Z_{ij} - \overline{Z}_{i.})^2} = 2.5413$$

Upper critical value for *F*-distribution at significance level of α = 5 % with *k*-1 and *N*-*k* degrees of freedom is calculated as an inverse cumulative probability with result of

$$F_{\alpha,k-1,N-k} = F_{5\%,1,8} = 5.318.$$

When statistic of Levene test is lower than the upper critical value for *F*-distribution, it is possible to fail to reject the null hypothesis and not accept the alternative hypothesis. Therefore, it is not statistically significant evidence at α = 5 % to show that there is a difference in variances.

5.6.6 Overall Statistics of Test for Equal Variances

Test for Equal variances was performed same way for all remaining pairs of the data as for copper inserts. Overall results are shown in Table 30.

Table 30 - Results for 17-4PH test for equal variances

	Insert	$\bar{x}$	F-critical	F-value	P-value	Valid
17-4PH	Copper	1088	5.318	2.541	0.128	H_0
	Copper WL	1196				
	Aluminium	1202		1.477	0.240	H_0
	Aluminium WL	1198				
	Bronze	1207		0.013	0.911	H_0
	Bronze WL	1212				
	ER + hBN	1215		1.498	0.237	H_0
	ER + hBN WL	1219				
	ER	1206		0.064	0.802	H_0
	ER WL	1210				
	3D	1249		1.581	0.225	H_0
	3D WL	1242				

Table 31 - Results for WPC test for equal variances

	Insert	$\bar{x}$	F-critical	F-value	P-value	Valid
WPC	Copper	21.6	5.318	0.406	0.532	H_0
	Copper WL	5.99				
	Aluminium	26.03		1.827	0.193	H_0
	Aluminium WL	6.14				
	Bronze	23.29		2.742	0.115	H_0
	Bronze WL	7.53				
	ER + hBN	27.20		0.596	0.450	H_0
	ER + hBN WL	8.19				
	ER	27.50		1.405	0.251	H_0
	ER WL	7.50				
	3D	28.89		0.219	0.645	H_0
	3D WL	8.63				

For all instances the null hypothesis was fail to reject at the significance level α = 5 % and therefore, one-way ANOVA comparison of the tensile strength means will be performed.

5.6.7 One-way ANOVA

Table 32 - Data for One-way ANOVA test for 17-4PH, copper insert

17-4PH Tensile Strength			
Var.	Tensile Strength [MPa]		
	Copper without Weld Line	Copper with Weld Line	Overall
1	1080	1180	
2	1110	1240	
3	1080	1170	
4	1090	1210	
5	1100	1230	
6	1080	1240	
7	1090	1150	
8	1130	1150	
9	1040	1190	
10	1080	1200	
$\bar{x}$	1088	1196	1142
$\tilde{x}$	1085	1195	
s	23.48	34.06	
υ	2.16	2.85	

When sample data are from normal population (we fail to reject H_0 at significant value α = 5 % in all sub-groups) and all variances are equal (we fail to reject H_0 at significant value α = 5 % in all sub-groups), One-way ANOVA for comparison of the sample data means was done:

$$F = \frac{MST}{MSE}$$

where numerator and denominator are calculated as:

$$SST == \sum_{i=1}^{k} n(x_i - \bar{x})^2 = \sum_{i=1}^{k} 10(1088 - 1142)^2 + 10(1196 - 1142)^2 = 58320$$

$$MST = \frac{SST}{p-1} = \frac{58320}{2-1} = 58320$$

$$SSE = \sum_{i=1}^{k} (n-1)s_i^2 = (10-1)23.43^2 + (10-1)34.06^2 = 15400$$

$$MSE = \frac{SSE}{N-p} = \frac{15400}{20-2} = 855.55$$

$$F = \frac{MST}{MSE} = \frac{58320}{855{,}55} = 68.1667$$

Upper critical value for F-distribution at significance level of α = 5 % with k-1 = 1 and N-k = 8 degrees of freedom is calculated as an inverse cumulative probability with result of:

$$F_{\alpha,k-1,N-k} = F_{5\%,1,8} = 5.3177$$

Calculated test statistic for ANOVA method is higher than the critical value for F-distribution and also p-value for One-way ANOVA of tensile strength sample data means from cooper inserts with and without weld line is P-value = 0.00. Therefore, it is possible to reject the null hypothesis H_0 at the 0.05 significance level.

5.6.8 Overall results of One-way ANOVA for 17-4PH and WPC

Table 33 - Results for 17-4PH and WPC one-way ANOVA

	Insert	One-Way ANOVA				
		$\bar{x}$	F-critical	F-value	P-value	Valid
17-4PH	Copper	1088	5.318	68.167	0.000	$H_{alternative}$
	Copper WL	1196				
	Aluminium	1202		0.108	0.746	H_0
	Aluminium WL	1198				
	Bronze	1207		0.067	0.799	H_0
	Bronze WL	1212				
	ER + hBN	1215		0.067	0.804	H_0
	ER + hBN WL	1219				
	ER	1206		0.034	0.856	H_0
	ER WL	1210				
	3D	1249		0.173	0.682	H_0
	3D WL	1242				
WPC	Copper	21.6		1066.8	0.000	$H_{alternative}$
	Copper WL	5.99				
	Aluminium	26.3		1062.6	0.000	$H_{alternative}$
	Aluminium WL	6.14				
	Bronze	23.29		832.9	0.000	$H_{alternative}$
	Bronze WL	7.53				
	ER + hBN	27.20		3385.3	0.000	$H_{alternative}$
	ER + hBN WL	8.19				
	ER	27.50		1829.5	0.000	$H_{alternative}$
	ER WL	7.50				
	3D	28.89		2050.5	0.000	$H_{alternative}$
	3D WL	8.63				

From the results of one-way ANOVA it is possible to see that the effect of weld line during injection molding of 17-4PH is statistically significant only when the copper insert was used. In case of conventional injection molding, weld line effect is significant regardless of used insert material.

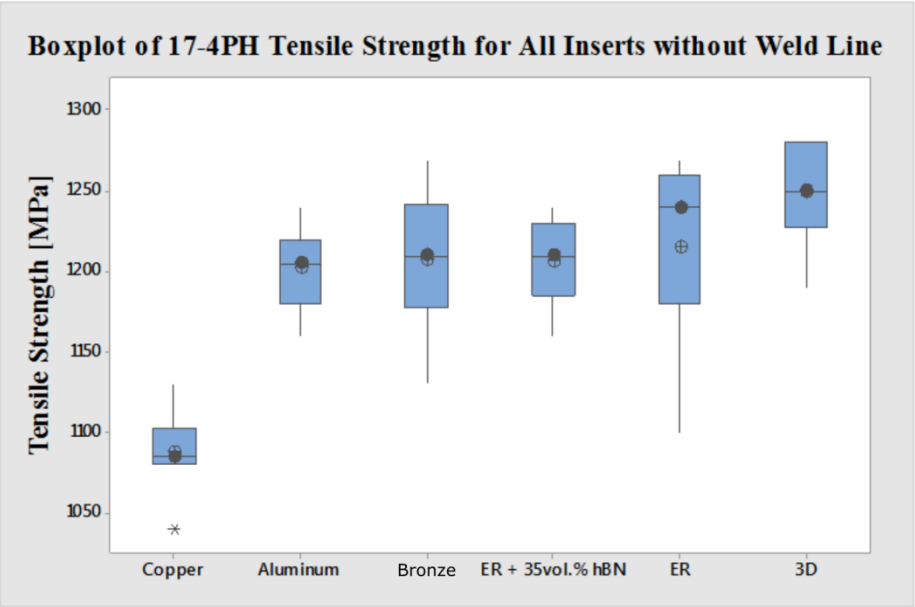

Fig. 66 - Boxplot of Tensile strength of 17-4PH for all insert without weld line

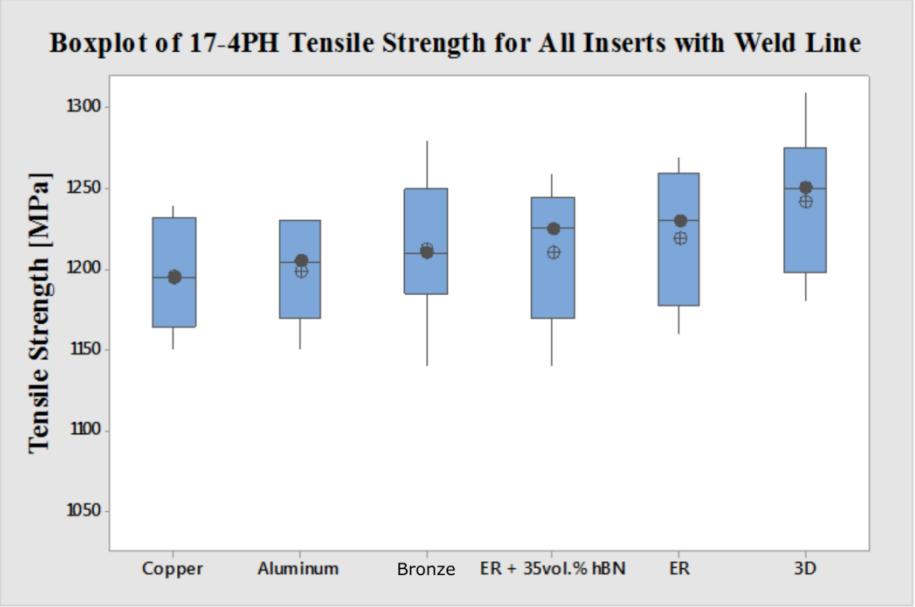

Fig. 67 - Boxplot of Tensile strength of 17-4PH for all insert with weld line

Influence of weld lines on tensile strength of 17-4PH compounds is not significantly affected by thermal conductivity of mold inserts (Rm,copper WL = 1196MPa, Rm, 3D WL = 1242 MPa). Increase of strength with slower cooling is about 4 %. On the other hand, when weld line is not formed, filling trajectory is longer and rapid solidification of 17-4PH feedstock due to high thermal conductivity results in lower tensile strength (Rm,copper = 1088MPa, Rm, aluminium = 1202MPa). Due to this finding, weld line formation has an effect of filling time reduction without a significant change of tensile strength.

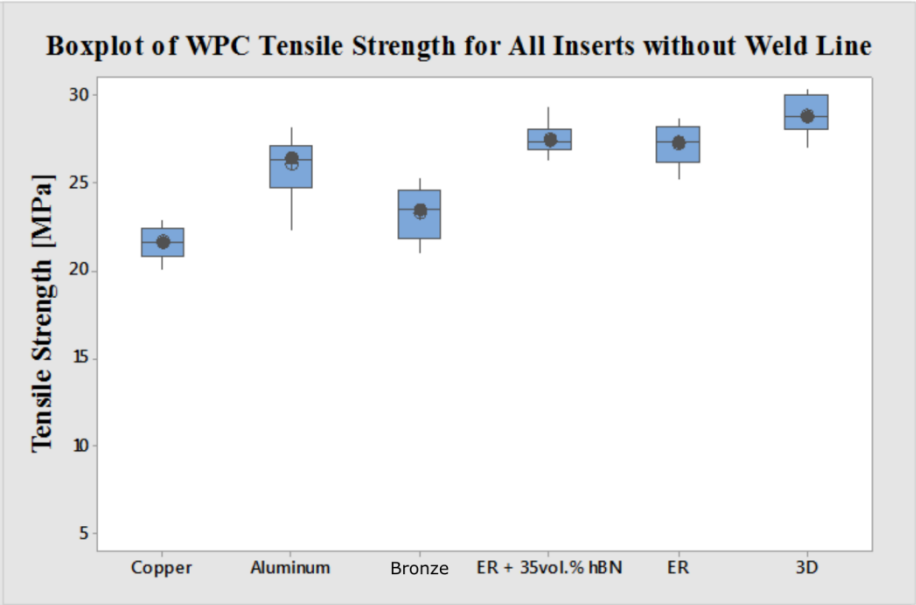

Fig. 68 - Boxplot of Tensile strength of WPC for all insert without weld line

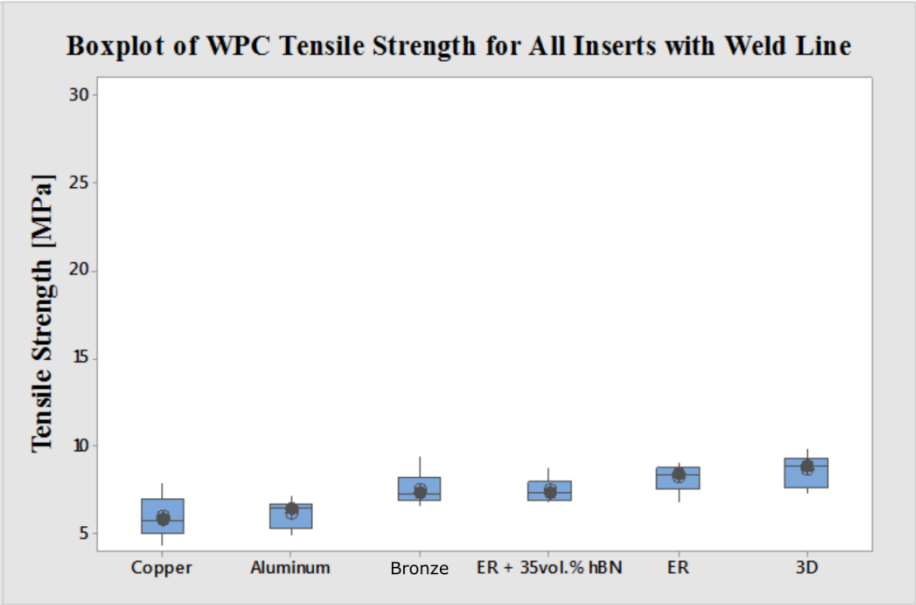

Fig. 69 - Boxplot of Tensile strength of WPC for all insert with weld line

On the other hand, from the boxplot diagrams (Figs. 68, 69) it is evident that cooling rate has effect on tensile strength of WPC compounds. When polymeric insert (λ = 0.2 W.m-1.k-1) is used instead of copper (λ = 394 W.m-1.k-1), tensile strength is for 33 % higher (Rm,copper = 21.64MPa, Rm, 3D = 28.89 MPa). Further, thermal conductivity affects tensile strength when weld line is formed. Positive effect of inserts with low cooling rate is up to 45 % (Rm,copper WL = 5.99MPa, Rm, 3D WL = 8.63MPa). Therefore, slower cooling rate results in higher tensile strength. Higher tensile properties are also result of elongated effect of packing due to slower solidification of the smallest cross section profile, for this case - gating system, that is confirmed with increased tensile strength in case of no weld line.

CONCLUSION

Presented Doctoral Thesis deals with mold design concept for injection molding of highly filled materials, where experiment is divided into two sections - mold design is studied from the perspective of phase separation and weld line formation.

Materials examined were 17-4PH stainless steel feedstock employed in powder injection molding (PIM) and wooden plastic composite (WPC) based on high density polyethylene matrix. As initial characteristics, melt rheology and thermal properties were determined and considered in Moldflow simulations.

With respect to previous findings in the area of phase separation, injection molding was simulated for two testing geometries, where shear rate gradient was found as a good indicator of phase separation. Injection molding is a processing route typical for complex shapes of molded parts, where the cross section changes often take place. For this reason, the new testing geometry for phase separation was designed, and an approach to determine the phase separation was developed.

Further, taking into account the fact that the main cause of phase separation are shear rate gradients, the monitoring of temperature may be useful in qualification of phase separation. To measure the temperature inside a mold cavity, non-conventional infrared sensors in 6 locations were tested. This method allows on-line monitoring of phase separation, which may be eventually inducted by deterioration of a cavity surface due to a wear associated with changes in melt/mold interactions, surface energy, and roughness.

The presence of the phase separation, after overheating of the material due to the shear rate gradients, was confirmed also with the help of computed tomography. According to the previous studies, observed cracks may lead to delamination after sintering, which is also accompanying phenomenon of the phase separation.

Highly filled materials are susceptible to negative effect of weld lines on tensile strength of molded parts. Weld line strength may be increased with increased time and temperature of diffusivity. For this reason, mold inserts for tensile test specimens from various thermal conductivity materials were designed and produced. Weld line formation has a strong influence on the tensile strength of WPC composites. When the acrylic polymer printed insert was used, the weld line strength reached the about 45 % higher in comparison with the copper insert. Enhanced tensile properties result also from the elongated effect of packing due to slower solidification of the smallest cross section profile. Situation differs in case of PIM feedstock, where the effect of weld lines is noticeable only for copper insert. However, the effect of weld line is positive in this case. The trajectory during injection molding of samples without weld line was longer in comparison to the situation when two gates were utilized (and weld line occured). PIM feedstock (λ = 4.0 $W.m^{-1}.k^{-1}$) in combination with

copper insert (λ = 394 $W.m^{-1}.k^{-1}$) solidifies quickly, and therefore, the elongation of filling stage (one gate - without weld line) results in the decreased packing time leading into deteriorated tensile strength. For this reason, weld lines in PIM technology may be advantageously used with regard to tensile strength properties, when filling time is decreased and duration of packing stage may be elongated.

CONTRIBUTION TO SCIENCE AND PRACTICE

The Thesis is aimed on qualification of phase separation during injection molding when material may be regrinded and used again. In other words, the aim is to enhance production economic with on-line determination of phase segregation. For this point of view contribution of the Doctoral Thesis to science and practice is:

- new testing geometry for phase separation with combination of segregation supporting elements;
- verification of reason for phase separation with CAE simulations where shear rate gradients take place;
- proposed way to measure melt temperature inside mold cavity and ensure identification of potentially critical area, where phase separation may occur due to dissipation heat induced by shear rate;
- non-destructive qualification of phase separation by computed tomography with respect to qualification in bulk.

Design standards for PIM tooling are generally copying design standards for conventional injection molding. When highly filled compounds are molded to form complex shapes, weld lines may occur. From the second part of the Thesis, the contribution to science and practice includes:

- weld lines in conventional injection molding of highly filled compound strongly affect tensile strength of molded products;
- thermal conductivity of mold insert in conventional injection molding of highly filled compounds has significant effect on tensile strength, where slower cooling rate have positive effect;
- weld lines in PIM do not effect tensile strength of final (sintered) products
- thermal conductivity of mold inserts in PIM has insignificant influence on tensile strength.

With the respect to the current competitor of forming technologies - additive manufacturing, the Thesis opens a possibility of low volume injection molding where:

- 3D printed mold inserts might be used;
- silicon mold copying 3D printed master model may be used, where liquid polymeric system with thermally conductive filler (to increase thermal conductivity) is casted to form a mold insert.

REFERENCES

Agassant, J. F., et. al. (2017) *Polymer processing: principles and modeling.* 2nd edition. Munich: Hanser Publishers, 841 p. ISBN 978-1-56990-605-7.

Anderson, I. E., White, E. M. H., Dehoff, R. (2018) *Feedstock Powder Processing Research Needs for Additive Manufacturing Development.* Current Opinion in Solid State and Materials Science. 22, pp. 8-15.

Andrews, I., et. al., (2010) *A Case Study on Computational Fluid Dynamics Analysis of Micro-MIM Products.* Powder Injection Moulding International, 4, pp. 55-65.

Atre, S., V., Park, S., J., Zauner, R., German, R., M. (2007) *Process Simulation of Powder Injection Molding. Identification of Significant Parameters During the Mold Filling Phase.* Powder Metallurgy, 50 (1), pp. 76-85.

Barriere, T., Gelin, J. C., Liu, B. (2002) *Improving Mould Design and Injection Parameters in Metal Injection Moulding by Accurate 3D Finite Element Simulation.* Journal of Materials Processing Technology, 125-126, pp. 518-524.

Bendada, A., Derdouri, A., Lamontage, M., Simard, Y. (2004) *Analysis of thermal contact resistance between polymer and mold in injection molding.* Applied Thermal Engineering, 24, pp. 2029-2040.

Bergstrom, J., Thuvander, F., Devos, P., Boher, C. (2001) *Wear of Die Materials in Full Scale Plastic Injection Moulding of Glass Fibre Reinforced Polycarbonate*. Wear, 251, pp. 1511-1521

Biehl, S., Lűthje, H., Bandorf, R., Sick, J. H. (2006) *Multifunctional thin film sensors based on amorphous diamond-like carbon for use in tribological applications,* Thin Solid Films, 515, pp. 1171-1175.

Biehl, S. et. al. (2016) *Multifunctional thin film sensor system as monitoring system in production*. Microsystem Technologies, 22, pp. 1757-1765.

Bilovol, V., V., Kowalski, L., Duszczyk, J., Katgerman, L. (2003a) *Comparison of numerical codes for simulation of powder injection moulding.* Powder Metallurgy, 46 (1), pp. 55-60.

Bilovol, V., V. (2003b) *Mould filling simulations during powder injection moulding.* Ph.D. Thesis, Delft University of Technology, Delft, The Netherlands.

Bhusman, B, et. al. (2000) *Modern Tribology Handbook*, Two Volume Set. Boca Raton: CRC Press, 1760 p. ISBN 978-0-84938-403-5

Bleyan, D., Hausnerova, B., Kasparkova, V., Pata, V. (2016) *Surface Adhesion between Ceramic Injection Molding Feedstocks and Processing Tools.* Ceramics International, 42, pp. 460-465.

Bose, A., et. al. (2018) *Traditional and additive manufacturing of a new Tungsten heavy alloy alternative.* International Journal of Refractory Metals and Hard Materials, 73, pp. 22-28.

Brandrup, J., Grulke E. A., Immergut, E. H. (1999) *Polymer handbook.* 4th ed. Hoboken, New Jersey: Wiley-Interscience, 2, ISBN 0471479365.

Bricout, J., et. al. (2013*) Influence of powder characteristics on the behaviour of PIM feedstock*, Chemical Engineering Research and Design, 91 (12), pp. 2484-2490.

Charmeau, J. Y., Chailly, M., Gilbert, V., Bereaux, Y. (2008) *Influence of mold surface coatings in injection molding: application to the ejection stage*. International Journal of Material Forming, 1 (1), 699–702.

Chen, S. C., Chen, J. T., Chien, D. R., Chen, C. S. (2007) *Investigation on the weldline strength of thin-wall injection molded ABS parts.* International Communications in Heat and Mass Transfer, 34 (4), pp. 448-455

Chen, S. C., et. al. (2009) *Effect of cavity surface coating on mold temperature variation and the quality of injection molded parts*. International Communications in Heat and Mass Transfer, 36 (10), pp 1030-1035.

Chookaew, W. (2013) *An Investigation of Weldline Strength in Injection Molded Rubber Parts*. Energy Procedia, 34, pp 767-774.

Cohen, Y., Metzner, A. B. (1982) *Adsorption effects in the flow of polymer solutions through capillaries*. Macromolecules, 15, pp. 1425-1429.

D'Agostino, R. B., Stephens, M. A. (1986) *Goodness-of-Fit Techniques*. New York: CRC Press, 1986, pp. 576, ISBN 978-0824774875

Dealy, J. M., Saucier, P. C. (2000) *Rheology in plastics quality control.* Munich: Hanser Publishers, 2000, 140 p. ISBN 3-446-21069-5.

DebRoy, T. (2018) *Additive Manufacturing of Metallic Components – Process, Structure and Properties*. Progress in Material Science, 92, pp. 112-224.

Derrick, B., Ruck, A., Toher, D., White, P. (2018) *Tests for equality of variances between two samples which contain both paired observations and independent observations.* Journal of Applied Quantitative Methods, 13 (2), pp.36-47.

Drummer, D., Messingschlager, S. (2014) *Ceramic injection molding material analysis, modeling and injection molding simulation.* AIP Conference Proceedings, pp. 582 - 586

Duretek, I., Holzer, C. (2017) *Material Flow Data for Numerical Simulation of Powder Injection Molding.* Universal Journal of Materials Science, 5, pp. 7-14.

Ebnesajjad, S. (2011) *Handbook of adhesives and surface preparation: technology, applications and manufacturing.* Amsterdam: Elsevier, 427 p. Plastics design Library. PDL handbook series. ISBN 978-1-4377-4461-3.

Enneti, R. K., Park, S. J. P., German, R. M., Atre, S. V. (2012) *Thermal debinding Process in Particulate Materials Processing.* Material and Manufacturing Processes, 27 (2), pp. 103-118.

Gasbarre, T.G., Jandesca, W.F. (1989). *Advances in Powder Metallurgy*, Metal Powder Industries Federation, Princeton, NJ.

Gasik, M., Zhang, B. (2000) *A constitutive model and FE simulation for the sintering process of powder compacts.* Computational Materials Science, 18 (1), pp. 93-101

German, R. M., Bose, A. (1997) *Injection molding of metals and ceramics*. [1st ed.]. Princeton: Metal Powder Industries Federation, 413 p. ISBN 1-878-954-61-x.

German, R. M. (2011) *Metal injection molding, A comprehensive MIM design guide*. Princeton: Metal Powder Industries Federation, 2011, xiii, 194. ISBN 978-0-9819496-6-6.

German, R. M. (2013) *Powder Injection Molding Design & Applications,* Innovative Materials Solutions, 260 p. ISBN 978-0972764209

Greiner, A., et. al. (2011) *Simulation of Micro Powder Injection Moulding: Powder Segregation and Yield Stress Effects During Form Filling.* Journal of the European Ceramic Society, 31, pp. 2525-2534.

Griffiths, C., et. al. (2014) *Influence of injection and cavity pressure on the demoulding force in micro-injection moulding*. Journal of Manufacturing Science and Engineering, 136 (3).

Grubbs, F. (1969), *Procedures for Detecting Outlying Observations in Samples*, Technometrics, 11 (1), pp. 1-21.

Gulsoy, O. H., German, R., M. (2008) *Production of micro-porous austenitic stainless steel by powder injection molding*. Scripta Materialia, 48, pp. 295-298.

Guerrier, P., Tosello, G., Hattel, H. J. (2017) *Flow visualization and simulation of the filling process during injection molding.* CIRP Journal of Manufacturing Science and Technology, 16, pp. 12-20.

Gundermann, P. (2017) *Review of the PM Industry from a European Perspective*, Euro PM2017, Milan, Congress Proceedings.

Gutierrez, J. G. et. al. (2016) *Models to Predict the Viscosity of Metal Injection Molding Feedstock Materials as Function of Their Formulation*. Metals - Open Access Metallurgy Journal, 6 (129).

Hashmi, S., (2016) *Comprehensive Materials Finishing*, Elsevier, pp. 1484, ISBN 978-0128032503

Hausnerova, B.; Marcanikova, L., Filip, P., Saha P. (2010) *Wall-slip velocity as a quantitative measure of powder-binder separation during powder injection moulding*, Proceeding of PM2010, Firenze

Hausnerova, B. (2011a). *Powder Injection Molding – An Alternative Processing Method for Automotive Items*, New Trends and Developments in Automotive Systems Engineering, pp. 130-146.

Hausnerova, B., Marcanikova, L., Filip, P., Saha P. (2011b). *Optimization of powder injection molding of feedstock based on aluminium oxide and multicomponent water-soluble polymer binder*. Polymer Engineering & Science, 51 (7), pp. 1376-1382.

Hausnerova, B., Sanetrnik, D., Ponizil, P. (2013). *Surface structure analysis of injection molded highly filled polymer melts*, Polymer Composites, 34, pp. 1553–1558.

Hausnerova, B., Sanetrnik, D., Paravanova, G. (2014a) *Wall-Slip of Highly Filled Powder Injection Molding Compounds: Effect of Flow Channel Geometry and Roughness*. AIP Conference Proceedings, 1599, pp. 518-521.

Hausnerova, B., Huba, J. (2014b) *Discrepancies in Design Determination of Metal Injection Molded Tensile Test Specimens*. Development in Machining Tehcnology, Krakow, ISBN 978-83-7242-765-6.

Hausnerova, B., Sanetrnik, D., Hnatkova, E. (2015) *Wall-Slip As A Phenomenon Attending Processing Of Highly Powder Particle Filled Polymer Melts*. M2D2015: Proceedings of the 6th International Conference on Mechanics and Materials in Design, pp. 705-708.

Heaney, D. F. (2012). *Handbook of metal injection molding*. Oxford: Woodhead Publishing, 2012, xvi, 586. Woodhead Publishing in materials. ISBN 978-0-85709-066-9.

Hebda et. al. (2019) *A method for predicting geometric characteristics of polymer deposition during fused-filament-fabrication*, Additive Manufacturing, 27, pp. 99-108.

Heim, H. P. (2016) Specialized injection molding *techniques*. Amsterdam: Elsevier, WA, 247 p. Plastics design Library. PDL handbook series. ISBN 978-0-323-34100-4.

Helmer, H., Bauereiß, A., Singer, R. F., Körner, C. (2016) *Grain structure evolution in Inconel 718 during selective electron beam melting*. Materials Science and Engineering: A, 668 (21), pp. 180-187.

Herzog, D., Seyda, V., Wycisk, E., Emmelmann, C. (2016) *Additive Manufacturing of Metals*. Acta Materialia, 117, pp. 371-392.

Hsu, K. C., and P. C. Tsai. (1995) *Spiral Flow Analysis on the Injection Molding of Alumina Powder – An Experimental Design*, Ceramics International, 21 (6), pp. 439-443

Jain, A. K., Murty, M. N., Flynn, P. J. (1999) *Data Clustering: a Review,* ACM Computing Surveys, 19 (3), pp. 264-323.

Jäntschi, L., Bolboacă, S. D., (2018) *Computation of Probability Associated with Anderson–Darling Statistic,* Mathematics, 6 (6).

Jariyatammanukul, P., Paecheroenchain, N., Pomkajohn, P., Patcharaphun, S. (2010) *Effect of Thickness on Weld Line Strength of Injection Molded Thermoplastic Composites.* Polymer - Plastic Technology and Engineering, 49 (13), pp. 1305-1309

Jenni, M. (2008) *Quantitative study of powder binder separation of feedstock*, PIM International, 2 (4), pp. 50-55

Jenni, M., Zauner, R., Stampfl, J. (2009) *Measurement Methods for Powder Binder Separation in PIM Components*. In EURO PM 2009: Proceedings Vol 2. Copenhagen: European Powder Metallurgy Association, pp. 141-146. ISBN 978-1899072071.

Jiranek, L., Hausnerova, B., Hartwig, T. (2010) *Community Design 001704974*, Office for Harmonization in the Internal Market, Alicante.

Karatas, Ç., Sözen, A., Arcaklioglu, E., Erguney S. (2008) *Investigation for mouldability for feedstocks used powder injection molding*. Materials & Design, 29 (9), pp. 1713-1724.

Kate, K. H., Enneti, R. K., McCabe, T., Atre, S. V. (2016) *Simulations and injection molding experiments for aluminum nitride feedstock.* Ceramics International, 42 (1), pp. 194-203.

Kato, K. (1988) *An Experimental and Theoretical Investigation of Ploughing, Cutting and Wedge Formation During Abrasive Wear.* Tribology International, 21, pp 51-57

Kayama, M., et. al. (2007) Dependence of Mold Conditions on Demolding Force - Effects of Water Contact Angle and Pattern Shape around Top Surface, *Digest of papers Microprocesses and Nanotechnology*, Kyoto, pp. 306-307.

Kazmer, D. (2007) *Injection mold design engineering*. Munich: Hanser Publishers, 423 p. ISBN 978-3-446-41266-8.

Kim, J. K., Thomas, S., Saha, P. (2016) *Multicomponent Polymeric Materials*. Springer, 410 p. ISBN 978-9-40177-323-2.

Kistler (2019) *Pressure and Temperature Sensor, direct measuring ø4 mm*. [ref. 2018-04-12], available at: https://www.kistler.com/en/product/type-6190c/

Krauss, V. A., et. al. (2007) *A Model for PEG Removal from Alumina Injection Molded Parts by Solvent Debinding*. Journal of Materials Processing and Technology, 182 (1-3), pp. 268-273.

Kukla, C. (2018) *Properties for PIM Feedstocks Used in Fused Filament Fabrication.* World PM Congress and Exhibition, Hamburg.

Kyas, K, Cerny, J., Stanek., M., Manas, M., Manas, D. (2012) *Measuring of temperature and pressure in injection mold.* International Journal of Mathematics and Computers in Simulation, 6, pp. 600-607.

Loebbecke, B., Knitter, R., Hausselt, J. (2009) *Rheological Properties of Alumina Feedstocks For the Low-Pressure Injection Moulding Process*. 29 (9), pp. 1595-1602.

Majewsky, C., Hopkinson, N. (2003) *Effect of tool finishing on ejection forces for injection moulded parts made using direct metal laser sintered tools*. International Journal of Production Research, 41(3), pp. 581–592.

Marhöfer, M. (2016) *Validation of precision powder injection molding process simulations using a spiral test geometry.* AIP Conference Proceedings.

Martin, P. J., Wilson, D. I. (2015) *A critical assessment of the Jastrzebski interface condition for the capillary flow of pastes, foams and polymers.* Chemical Engineering Science, 60, pp. 493-502

Martinsen, K., Gellein, L. T., Boivie, K. M. (2017) *Sensors embedded in surface coatings in injection moulding dies.* Procedia CIRP, pp. 386-390.

Mennig, G. (1995) *Wear mechanisms in plastic processing*, Mater. Sci. Eng. Technol. 26, 520–523.

Moore, D. F. (2013). *Principles and Applications of Tribology*. Elsevier, 388 p. ISBN 978-1-48312-486-5.

Mostafaei, A., DeVecchis, P. R., Nettleship, I., Chmielus, M. (2019) *Effect of Powder Size Distribution on Densification and Microstructural Evolution of Binder-Jet 3D-Printed Alloy 625.* Materials & Design, 162, pp.375-383.

Nguyen, Q. B., et. al. (2017) *Characteristics of Inconel Powders for Powder-Bed Additive Manufacturing.* Engineering, 3 (5), pp 695-700.

Oberg, E., et. al. (2016) *Machinery's handbook: a reference book for the mechanical engineer, designer, manufacturing engineer, draftsman, toolmaker, and machinist.* 30th edition. South Norwalk: Industrial Press, 2016, xi, 2883 s. ISBN 978-0-8311-3092-3.

Otsuka, A. (2018) *Nippon Piston Ring: Leading Japanese MIM producer builds on automotive success*. Powder injection moulding international, 12 (1), pp. 57.

Parenti, P., Cataldo, S., Annoni, M. (2018) *Shape deposition manufacturing of 316L parts via feedstock extrusion and green-state milling,* Manufacturing Letters, 18, pp. 6-11.

Pouzada, A., Ferreira, E., Pontes, A. (2006) *Friction properties of moulding thermoplastics*. Polymer Testing, 25 (8), pp. 1017–1123.

Rak, Z. S. (1999). *New trends in powder injection moulding*. Powder metallurgy and metal ceramics, 38 (4), pp.126-132.

Raza, R., et. al. (2015) *Effects of binder system and processing parameters on formability of porous Ti/HA composite through powder injection molding*. Materials and Design, 87, pp. 386-392.

Reddy, J. J. (1996) *Novel method for assessment of critical powder packing during powder forming*. Powder Metallurgy, 39 (4), pp. 281-285.

Roetenberg, K. S.(1992) *Optimization of the mixing process for powder injection molding.* Proceedings of the Powder Injection Molding Symposium, York, 1992.

Rosato, Dominick V., Rosato Donald V., Rosato M. G. (2000) *Injection molding handbook*. 3rd ed. Boston: Kluwer Academic Publishers, xxxi, 1457 s. ISBN 0792386191.

Sadowski, M., Ladani, L., Brindley, W., Romano, J. (2016) *Optimizing quality of additively manufactured Inconel 718 using powder bed laser melting process.* Additive Mnufacturing, 11, pp. 60-70.

Samanta, S. K., et. al. (2008) *A Numerical Study of Solidification in Powder Injection Molding Process*. International Journal of Heat and Mass Transfer, 51 (3-4), pp. 672-682.

Sames, W. J. (2014) *Effect of Process Control and Powder Quality on Inconel 718 Produced Using Electron Beam Melting*. 8th International Symposium on Superalloy 718 and Derivatives, ISBN 9781119016854.

Schneider, J., Iwanek, H., Gahr, K. H. Z. (2005) *Wear behaviour of mould inserts used in micro powder injection moulding of ceramics and metals*. Wear, 259, pp 1290-1298

Shiguang, L. (2007) *Dimensional Variation in Production of High-Aspect-Ratio Micro-Pillars Array by Micro Powder Injection Molding.* Applied Physics A, 89 (3), pp. 721-728.

Spierings, A. B., Herres, N., Levy, G. (2011) *Influence of the Particle Size Distribution on Surface Quality and Mechanical Properties in AM Steel Parts.* Rapid Prototyping Journal, 17 (3), pp. 195-202.

Srinivasan, R., Giannikas, V., McFarlane, D., Thorne, A. (2018) *Customising With 3D Printing: The Role of Intelligent Control.* Computers in Industry. 103, pp. 38-46.

Suresh, G. A., Hsiao, K. T. (2012) Manufacturing techniques for polymer matrix composites (PMCs). Oxford: Woodhead Publishing, 2012, pp. 512, ISBN 978-0-85709-067-6.

Tadmor, Z., Gogos, C. G. (2006) *Principles of polymer processing.* 2nd ed. Hoboken, New Jersey: John Wiley, 961 p. ISBN 0-471-38770-3.

Thornagel, M. (2009) *MIM-Simulation: A Virtual Study on Phase Separation*. In EURO PM 2009: Proceedings Vol. 2. Copenhagen : European Powder Metallurgy Association, pp. 135-140. ISBN 978-1899072071.

Thornagel, M. (2010) *Simulating flow can help avoid mould mistakes*., Metal Powder Report, 65 (3), pp. 26-29

Tuncer, N., et.al. (2014) *Study of metal injection molding of highly porous titanium by physical modeling and direct experiments*. Journal of Materials Processing Technology, 214, pp. 1352-1360.

Walale, A., et. al. (2018) *Analysis of Shrinkage & Warpage in Ceramic Injection Molding of HPT Vane Leading Edge Core of a Gas Turbine Casting.* Materials Today: Proceedings, 5 (9), pp.19471-19479.

Walcher H. (2013) Personal Communication with Hartmut Walcher, MIM Expert in Arburg GmbH + Co KG.

Wang, Y. H., Qu, X. H., Zhang, W. F., Li, W. (2011) *Analysis of Powder Segregation in Powder Injection Molding.* Advanced Materials Research, 217, pp. 1372-1379.

Wilkinson, A. N. & Ryan, A. J., (1998). *Polymer processing and structure development,* Dordrecht: Kluwer Academic Publishers.

Wu, A. S. (2014) *An Experimental Investigation into Additive Manufacturing Induced Residual Stresses in 316L Stainless Steel.* Metallurgical and Materials Transactions A, 45 (13), pp. 6260-6270.

Xie, L. et. al. (2010) *Influence of Particle Concentration and Type on Flow, Thermal, and Mechanical Properties of Wood-Polypropylene Composites.*

Journal of Reinforced Plastics and Composites, 29 (13), pp. 1940-1951.

Xinbo, H., et. al (2014) *The Effects of Filling Patterns on the Powder–Binder Separation in Powder Injection Molding.* Powder Technology, 256, pp. 367-376.

Yang, S., Zhang, R., Qu, X. (2015) *Optimization and evaluation of metal injection molding by using X-ray tomography*. Materials Characterization, 104, pp. 107-115.

Yilmazer, U., Kalyon, D. M. (1989) *Slip effects in capillary and parallel disk torsional flows of highly filled suspensions*. Journal of Rheology, 33, pp. 1197-1212.

Zhang, B., Gasik, M. M. (2002) *Stress evolution in graded materials during densification by sintering processes.* Computational Materials Science, 25 (1-2), pp. 264-271.

Zhou, Y., Mallick, P. K. (2014) *Effect of Melt Temperature and Hold Pressure on the Weld-Line Strength of an Injection Molded Talc-Filled Polypropylene*. Journal of Composites, pp 1-8.

LIST OF FIGURES

LIST OF TABLES

LIST OF SYMBOLS

PIM	Powder Injection Molding
MIM	Metal Injection Molding
CIM	Ceramic Injection Molding
DSC	Differential Scanning Calorimetry
WLF	Williams-Landel-Ferry
IR	Infra-red
MF	Moldflow
SEM	Scanning Electron Microscopy
EDX	Energy-dispersive X-ray spectroscopy
SLM	Selective Laser Melting
AM	Additive Manufacturing
DED	Direct Energy Deposition
PBF	Powder Bed Fusion
UAM	Ultrasonic Additive Manufacturing
BJ	Binder Jetting
FDM	Fused Deposition Manufacturing
L	Laser
EB	Electron Beam
CAD	Computer-aided design
CAE	Computer-aided engineering
PSH	Powder Space Holder
hBN	Hexagonal Boron Nitride
PMMA	Polymethyl methacrylate
KCl	Calcium Chloride
NaCl	Sodium Chloride
POM	Polyoxymethylene
HDPE	High-density Polyethylene
PP	Polypropylene
ABS	Acrylo butadiene styrene
PTFE	Polytetrafluorethylene
TPE	Thermoplastic elastomer
WPC	Wood-plastic composite
TiN	Titanium nitride
ZrO_2	Zirconium dioxyde
Al_2O_3	Aluminium oxide
L/D	Length to diameter ratio
HVN	Vickers hardness
HRC	Rockwell hardness
exp	Exponential function
ln	Natural logarithm

mm	millimetre
µm	micrometre
g	gram
W	Watt
m	metre
K	Kelvin degree
°C	Celsius degree
V	Volt
%	percent
h	hour
min	minute
Pa	Pascal
MPa	Megapascal
s	second
vol.%	volume percent
wt.%	weight percent
$\dot{\varepsilon_e}$	Elastic strain rate
$\dot{\varepsilon_{th}}$	Thermal strain rate
$\dot{\varepsilon_{vp}}$	Visco-plastic strain rate
D_e	Elastic stiggness
$\dot{\sigma}$	Stress rate
E	Young modulus
ν	Poisson's ratio / coefficient of variation
ρ	Density
p	Pressure
t	Time
Δ	Delta (difference)
λ	Thermal conductivity
δ	Shrinkage
$\bar{x}$	Arithmetic mean
$\tilde{x}$	Median
s	Standard deviation
α	Significance level
G	Grubbs test
AD	Anderson-Darling test
H_0	Null hypothesis
$H_{alternative}$	Alternative hypothesis
€	EURO
η	Shear viscosity
η_0	Shear viscosity of first newtonian plateau
η_∞	Shear viscosity of second newtonian plateau
τ	Shear stress

$\dot{\gamma}$	Shear rate
τ^*	Shear stress (transition - first plateau and shear thinning region)
n	Non-Newtonian index / number of observation
m	coefficient of consistency
N	Number of observations
k	sub-group
φ	Volume fraction of a filler
x, y, z	Cartesian coordination system
V_{ef}	Effective velocity
V_s	Velocity of solid phase
V_f	Velocity of fluid phase

LIST OF AUTHOR`S PUBLICATIONS

HUBA, J., SANETRNIK, D., HNATKOVA, E., HAUSNEROVA, B. Mechanical properties of sintered PIM test specimens. In: EAN 2014 - 52nd International Conference on Experimental Stress Analysis. Mariánské Lázně: Curran Associates, Inc., 2014

HAUSNEROVA, B., **HUBA, J.** Discrepancies in Design Determination of Metal Injection Molded Tensile Test Specimens. Development in Machining Tehcnology, Krakow, 2014, ISBN 978-83-7242-765-6.

HUBA, J., HAUSNEROVA, B. A New Mold Design For Qualification Of Powder/Binder Separation In Pim Technology. In: M2D2015: Proceedings of the 6th International Conference on Mechanics and Materials in Design. P Delgada: INEGI-FEUP, 2015, s. 559-562.

HUBA, J., HAUSNEROVA, B. A New Mold Design For Qualification Of Powder/Binder Separation In Pim Technology. In: M2D2015: Proceedings of the 6th International Conference on Mechanics and Materials in Design [online]. P Delgada: INEGI-FEUP, 2015, s. 559-562.

HUBA, J., SANETRNIK, D., HNATKOVA, E., HAUSNEROVA, B., DVORAK, Z. New application of powder injection molded product in medical field. Manufacturing Technology. 2016, vol. 16, iss. 1, s. 94-98. ISSN 1213-2489

FOJTL, L., **HUBA, J.**, KUBISOVA, M., PATA, V., MRACEK, A., SEDLACEK, T. Modern types of PVD/PACVD coatings used for injection molds and their effects on selected physical properties of mold cavities. In: METAL 2017 - 26th International Conference on Metallurgy and Materials, Conference Proceedings. Brno: TANGER Ltd., 2017, s. 1258-1263.

Utility models

HAUSNEROVA, B., **HUBA, J.**, KREIZLOVA, J. Vstřikovaná struktura pro kvalitativní vyhodnocení fázové separace kompozitu na bázi polymerní matrice vysoce plněné kovovým nebo keramickým práškem. IPC: Czech Republic. Utility model, CZ 2014-30495 U1

HUBA, J., HAUSNEROVA, B., PATA, V., HAUSNER, D. Vstřikovací forma. IPC: Czech Republic. Utiliti model, PUV 2019-36080 - *application filed*

AUTHOR`S CV

PERSONAL INFORMATION Jakub Huba

Pod Vrskom 7, 034 03 Ruzomberok (Slovakia)
+420 57 603 5173
+420 776 576 106
jhuba@utb.cz

WORK EXPERIENCE

2018 - Present — Assistant
Tomas Bata University in Zlin
nam. T. G. Masaryka 5555, 760 01 Zlin (Czech Republic)
www.utb.cz

2013–2018 — R&D Assistant
Plastic Cluster z.s.
Vavreckova 5262, 760 01 Zlin (Czech Republic)
www.plastr.cz
3D technologies (3D printing, 3D scanning)
evaluation of CT data

2013–2017 — Junior Researcher
Tomas Bata University in Zlin
nam. T. G. Masaryka 5555, 760 01 Zlin (Czech Republic)
www.utb.cz

EDUCATION AND TRAINING

2013–Present — PhD. student
Tomas Bata University in Zlin, Zlin (Czech Republic)
Degree Programme: Process Engineering
Degree Course: Tools and Processes

2011–2013 — Ing.
Tomas Bata University in Zlin, Zlin (Czech Republic)
Degree Programm: Process Engineering
Degree Course: Technological Equipment Construction
Master's thesis: Mechanical Properties of Injection Molded Rubber Products

2008–2011 **Bc.**

Tomas Bata University in Zlin, Zlin (Czech Republic)

Degree program: Process Engineering
Degree course: Technological Equipment
Bachelor's thesis: Utilization of Reverse Engineering for Design of Injection Molds

PERSONAL SKILLS

Mother tongue(s) Slovak

	Listening	Reading	Spoken interaction	Spoken production	Writing
English	B2	B2	B2	B2	B2

Job-related skills
- Understanding of processes in plastic industry
- Good knowledge of tool design for plastic processing (especially of injection molds)
- Proactive in problem-solving

Digital skills
Microsoft Office ™ Tools
CAD, CAE, CAM programs (CATIA, Solid Works, Autodesk Moldflow, Cadmould, NX 9.5)
FEM/FEA programs (Cosmos, CATIA FEM modul)
VG StudioMAX 2.2 (Evaluation od CT data)
Graphic programs (Photoshop, Inkscape, Keyshot)

Driving licence B1, B

ADDITIONAL INFORMATION

Projects
- CORNET - Smart coating systems for process control and increased wear resistance in processing of natural fibre reinforces polymers - CZ.01.1.02/0.0/0.0/15_007/0001161
- Centre of advanced polymer and composite materials (Centers of Competence) - 2012-2019 - TE01020216
- Centre of Polymer Systems - (CZ.1.05/2.1.00/03.0111)

Jakub Huba

Mold Design Concept for Injection Molding of Highly Filled Compounds

Koncept vstřikovací formy pro vysoce plněné polymery

Doctoral Thesis

Publication Year: 2019